REACTIVE EVAPORATION OF CHROMIUM FROM STAINLESS STEEL AND THE REACTIVE CONDENSATION OF CHROMIUM VAPOR SPECIES ON CERAMIC SURFACES

by

Gregory Steven Tatar

A dissertation submitted in partial fulfillment
of the requirements for the degree

of

Doctor of Philosophy

in

Chemical Engineering

MONTANA STATE UNIVERSITY
Bozeman, Montana

November 2018

©COPYRIGHT

by

Gregory Steven Tatar

2018

All Rights Reserved

ACKNOLEDGEMENTS

In working through my PhD program, there were several individuals and organizations which helped by way of funding, teaching, advising, and encouragement. First and foremost I would like to thank my advisor, Dr. Paul Gannon, for his unwavering support, advice, and sincerity in his efforts to help me succeed. I appreciate the willingness of Drs. Robert Walker, Stephen Sofie, and Roberta Amendola to agree to take on the responsibilities associated with being on a PhD committee, in addition to their valuable criticisms and suggestions for improvement. I am grateful for the opportunity to have earned a stipend as a graduate teaching assistant, as provided by the department of Chemical and Biological Engineering (ChBE). The ChBE, in addition to the Graduate School, also provided funding assistance for conference travel which was a great help. The characterization techniques available through the Imaging and Chemical Analysis Laboratory (ICAL), as well as input from helpful ICAL staff, proved invaluable. Lastly, I would like to acknowledge funding from Morgan Advanced Materials, which allowed for a portion of the research performed in this work to be completed.

TABLE OF CONTENTS

1. INTRODUCTION 1

Dissertation Overview and Structure 1
Content in Chapter One 3
Background 4
Impacts of the Reactive Evaporation of Chromium 6
Human Health and the Environment 6
High Temperature Corrosion of Ferritic Stainless Steel 6
Solid Oxide Fuel Cell Degradation 7
Reactive Evaporation 9
Transpiration Method 10
Thermodynamic Modeling 16
Thesis Statement 23

2. REACTIVE EVAPORATION OF CHROMIUM FROM FERRITIC STAINLESS STEEL 25

Content in Chapter Two 25
Basic Material Science of Ferritic Stainless Steel 26
Behavior of Ferritic Stainless Steel at High Temperature 34
Influence of Water Vapor 51
Influence of Ceramic Contacting Conditions 64

3. VOLATILE CHROMIUM SPECIES AND SOLID OXIDE FUEL CELLS 82

Content in Chapter Three 82
Solid Oxide Fuel Cell Basics 82
Material Selection for Solid Oxide Fuel Cell Components 86
Interactions between Volatile Chromium Species and Solid Oxide Fuel Cell Components 90
Cathode and Electrolyte 90
Sealing Glass 95

TABLE OF CONTENTS CONTINUED

4. CHROMIUM ON CERAMIC CATALYST SUPPORTS 100

Content in Chapter Four.....100
Catalyst Supports 100
Cr Catalyst Preparation Method.....101
Surface Chromium Compound Formation.....102
Consensus and Contradiction.....108

5. INVESTIGATION OF SURFACE INTERACTIONS BETWEEN VOLATILE CHROMIUM SPECIES AND CERAMICS.....113

Content in Chapter Five 113
Interactions on Aluminosilicate Fibers 114
Methods.....114
Observations and Interpretations 117
Interactions on Alumina, Quartz Wool, and Mica.....127
Methods.....128
Observations and Interpretations 129

6. CONCLUSION.....147

Summary and Implications 147
Limitations and Future Work.....150

REFERENCES CITED.....154

LIST OF TABLES

Table Page

1. Stainless Steel T409 Elemental Composition 70

2. Total Chromium Content on Fibers 81

3. XPS Peak Information for Brown Staining on Aluminosilicate Fibers 120

4. XPS Peak Information for Green Staining on Aluminosilicate Fibers 121

5. XPS Peak Information for Yellow Staining on Aluminosilicate Fibers 122

6. Record of Alumina, Mica, and Quartz Wool Samples Possessing Detectable Levels of Chromium using XPS 130

7. XPS Peak information for Quartz Wool Samples 134

8. XPS Peak information for Mica Samples 136

9. XPS Peak information for Alumina Samples 139

LIST OF FIGURES

Figure Page

1. Solid Oxide Fuel Cell Schematic 8
2. Transpiration Equipment 11
3. Volatile Chromium Species and Varied Water Partial Pressure 13
4. Volatile Chromium Species and Varied Oxygen Partial Pressure 13
5. Log of Equilibrium Constants Plotted Against Inverse Temperature 16
6. Thermodynamic Modeling of Volatile Chromium Species 21
7. Body Centered Cubic Structure 26
8. Miller Indices 27
9. Crystal Planes 27
10. Grain Boundary Illustration 28
11. Grain Boundary Micrograph 28
12. Edge and Screw Dislocations 31
13. Dislocation Slip 32
14. Dislocation Climb 32
15. Gibbs Free Energy of Formation of Metal Oxides 35
16. Metal Oxidation Illustration 37
17. Oxidation Kinetics 39
18. Ellingham Diagram 41
19. Internal Oxidation of Binary Alloy 42
20. Continuous External Scale Formation on Binary Alloy 43

LIST OF FIGURES CONTINUED

Figure Page

21. Oxide Layer in Compression 50

22. Boundary Layer Regions 52

23. Law of the Wall 56

24. Chromium Collection and Gas Flow Rate 59

25. Chromium Mass Transport Coefficients 59

26. Thermodynamic Modeling in Low and High Pressure Steam 61

27. Thermodynamic Modeling of Cr Volatility for Perovskites and Chromia 67

28. Experimental Setup for Oxidation of Metals Study 72

29. Diffraction Patterns for Non-contacting Surfaces 73

30. Diffraction Patterns for Contacting Surfaces 74

31. Non-contacting Surface Morphology Micrographs 74

32. Contacting Surface Morphology Micrographs 75

33. Proposed Mechanism for Oxidation of Metals Study 79

34. Micrograph Images of Contrasting Whisker Formation 80

35. Solid Oxide Fuel Cell Schematic 83

36. Planar Stacked Solid Oxide Fuel Cell Schematic 84

37. 5 kW Planar Stacked Solid Oxide Fuel Cell 84

38. Tubular Stacked Solid Oxide Fuel Cell Schematic 85

39. Electrochemical Deposition at Triple Phase Boundary 91

40. Extension of Triple Phase Boundary through Chromia 92

LIST OF FIGURES CONTINUED

Figure Page

41. Extension of Triple Phase Boundary through Electrolyte 92

42. Electrochemical Deposition on Cathode.....93

43. Chemical Deposition at the Triple Phase Boundary.....94

44. Chemical Deposition on Cathode 94

45. Glass and Stainless Steel Interact to Form Strontium Chromate.....96

46. Auger Electron Spectroscopy Depth Profiling 96

47. Interfacial Interaction between Glass and Stainless Steel.....98

48. Influence of Isoelectric Point and pH on Hydroxyl Groups 103

49. Chromate under Hydrated and Calcined Conditions 104

50. Experimental Setup for Journal of the Electrochemical Society Study.....115

51. Broad and Defined Multiplet Splitting Structure of Chromia 117

52. Staining on Aluminosilicate Fibers.....118

53. Colors of Aluminosilicate Fiber Staining 118

54. Cr 2p3/2 Energy Window for Brown Staining 119

55. Cr 2p3/2 Energy Window for Green Staining 120

56. Cr 2p3/2 Energy Window for Yellow Staining 121

57. Formation of Chromate on Aluminosilicate Fibers 123

58. Formation of Chromium Trioxide on Aluminosilicate Fibers.....124

59. Formation of Chromia on Aluminosilicate Fibers.....125

60. Experimental Setup for Surface and Interface Analysis Study.....129

LIST OF FIGURES CONTINUED

Figure Page

61. Interpretation of Spectra 129

62. Stain Colors on Quartz Wool.....132

63. Stain Colors on Alumina.....132

64. Mica Samples Pre/Post Exposure 132

65. XPS Spectra for Quartz Wool.....134

66. XPS Spectra for Mica 135

67. XPS Spectra for Alumina in Cold Zones.....137

68. XPS Spectra for Alumina in Hot Zones.....138

69. Proposed Modification to General Mechanism at High Temperature 142

70. Mechanism Summary in Cold Zones.....144

71. Mechanism Summary in Hot Zones 145

DEFINITION OF TERMS

ASR – Area Specific Resistance

BCC – Body Centered Cubic

CTE – Coefficient of Thermal Expansion

EBSD – Electron Backscatter Diffraction

EDS – Energy Dispersive X-ray Spectroscopy

FESEM – Field Emission Scanning Electron Microscope

FWHM – Full Width at Half Maximum

GDC – Gadolinium-Doped Ceria

GL – Gaussian Lorentzian

HSAB – Hard Soft Acid Base

IEP – Isoelectric Point

LNF – Lanthanum Nickel Ferrite

LSCF – Lanthanum Strontium Cobalt Ferrite

LSF – Lanthanum Strontium Ferrite

LSM – Lanthanum Strontium Manganite

MIEC – Mixed Ionic Electronic Conductor

ORR – Oxygen Reduction Reaction

PBR – Pilling-Bedworth Ratio

REO – Reactive Element Oxide

DEFINITION OF TERMS CONTINUED

SOFC – Solid Oxide Fuel Cell

ToF-SIMS – Time of Flight Secondary Ion Mass Spectroscopy

TPB – Triple Phase Boundary

XPS – X-ray Photoelectron Spectroscopy

XRD – X-ray Diffraction

YSZ – Yttria-Stabilized Zirconia

ABSTRACT

Stainless steels are often used in high temperature (≥500°C) applications such as solid oxide fuel cells (SOFCs), combustion engine exhaust systems, and various power/chemical plant process equipment. At high temperatures and in oxidizing conditions, chromium containing oxides, such as chromia (Cr_2O_3), form protective surface layers on the underlying stainless steel. Reactive evaporation of these surface layers, however, may form volatile chromium species such as $CrO_2(OH)_2$ and CrO_3, compromise the protection of stainless steels, and cause deleterious downstream effects. Such effects include SOFC performance degradation and hazardous materials generation. This study focuses on both the reactive evaporation and reactive condensation processes and their dependencies on materials and environmental conditions. First, the corrosion behaviors of stainless steels were investigated in a variety of exposure conditions and then the nature of chromium vapor condensation was investigated on ceramic surfaces under various conditions.

Ferritic stainless steel samples (T409) were examined after 700°C exposures (94 h) to dry or wet air or nitrogen, and with or without contacting aluminosilicate fibers. Surface compositions and structures were characterized using field emission scanning electron microscopy, energy dispersive x-ray spectroscopy, and x-ray diffraction. The fibers had a substantial impact on corrosion behaviors; likely serving as a mass transport barrier for corrosive gas species. Observed corrosion behaviors under these different environments and their potential mechanisms are presented and discussed. Additionally, quantification of chromium content on fibers was performed using inductively coupled plasma mass spectroscopy. Fibers were observed to collect chromium in dry/moist air consistent with the formation of CrO_3 and $CrO_2(OH)_2$, respectively, and their subsequent reactive condensation.

To better understand the reactive condensation of volatile chromium species onto various ceramic surfaces, volatile chromium species were generated from chromium containing sources at 500-900°C and flowed past samples of aluminosilicate fibers, alumina, mica, and quartz wool at temperatures ranging from 100-900°C for 24-150 hours. The ceramic surfaces were characterized using x-ray photoelectron spectroscopy. Analysis of Cr $2p_{3/2}$ peak positions revealed the influence of temperature, material, and exposure time on the oxidation states of surface chromium compounds, and extent of chromium deposition. Potential mechanisms are proposed to help explain the observed trends.

CHAPTER ONE

INTRODUCTION

Dissertation Overview and Structure

The goal of this research is to determine what factors influence the deposition mechanisms of volatile chromium species onto ceramics. The study results indicate deposition may be influenced by temperature, chromium loading, and the hydroxyl population/properties of a material. Ceramics examined in this investigation include alumina, silica, and aluminosilicates, though the author believes the explanatory value of the proposed factors is not limited to these materials. This may allow for the discovery of materials which resist chromium deposition in the case of SOFCs, enhance chromium deposition for getters, or encourage the formation of trivalent species in processes at risk of spreading the hexavalent form.

The content of this dissertation is organized, fundamentally, into four parts. The introduction (Chapter 1), literature review (Chapters 2-4), investigation of the problem (Chapter 5), and conclusion (Chapter 6). The introduction defines the reactive evaporation of chromium, covers its importance for human health, the environment, SOFCs, and states the focus of this research, in addition to its limitations. The literature review portion begins with an account of the relevant science for each chapter, and then draws from studies related to the reactive evaporation of chromium and/or condensation. These studies are centered on ferritic stainless steel corrosion, solid oxide fuel cell systems, and ceramic catalyst supports. The literature grounding provides the necessary

tools to proceed to Chapter 5, which describes the methods used to investigate surface interactions between volatile chromium species and ceramics, in addition to observations, and interpretations. The last chapter, the conclusion, summarizes the work performed, reiterates potential implications and limitations of the work, and describes future work which may be performed to test the hypothesis presented here.

Several first author papers are outlined in the dissertation. “Surface Studies of T409 Stainless Steel at 700°C in Wet or Dry Air or N_2 With and Without Contacting Ceramic Fibers”, published in *Oxidation of Metals* [1], is outlined in Chapter 2: Influence of Ceramic Contacting Conditions. “XPS Characterization of Aluminosilicate Fibers Post Interaction with Chromium Oxyhydroxide at 100-230°C”, published in the *Journal of the Electrochemical Society* [2], is outlined in Chapter 5: Interactions on Aluminosilicate Fibers. “Investigation of Surface Interactions between Volatile Chromium Species and Ceramics”, under review with *Surface and Interface Analysis* [3], is outlined in Chapter 5: Interactions on Alumina, Quartz Wool, and Mica.

Co-authored publications, not included herein, but having contributed to the intellectual body of work and development of the skillset of the author, include “Influence of Silicon on High Temperature (600°C) Chlorosilane Interactions with Iron” which was published in *Solar Energy Materials* [4], and “High-Temperature (550-700°C) Chlorosilane Interactions with Iron” which was published in the *Journal of the Electrochemical Society* [5]. Chlorosilane species are used in the production of ultra-high purity silicon. These species may react with iron in process equipment to form iron silicide and iron chloride. Iron silicides are partially protective oxide layers, but iron

chloride tends to volatilize and may result in accelerated failure of the affected equipment [4, 5]. These studies do not focus on volatile chromium species, but are thematic in the sense of examining the phenomenon of reactive evaporation.

Lastly, this dissertation was written with the intention of being accessible to any reader with a scientific background. Many concepts are introduced from the ground up, and experts in these areas may find these sections unnecessary for comprehension of later material. For readers with this expertise, the following sections in Chapters 1-3 are recommended: Ch. 1 – Thesis Statement and Limitations, Ch. 2 - Influence of Ceramic Contacting Conditions, and Ch. 3 – Interactions between Volatile Chromium Species and Solid Oxide Fuel Cell Components. Chapters 4-6 are recommended for all readers.

Content in Chapter One

Chapter One goes into background on impacts of the reactive evaporation and/or condensation of chromium vapor species, basic theory of thermodynamics and transpiration experiments, and ends with the thesis statement. Impacts of reactive evaporation and/or condensation of chromium vapor species may be seen in human health and the environment, high temperature corrosion of ferritic stainless steel, and degradation of solid oxide fuel cells. To explain how what is known of chromium vapor species is known, basic principles of thermodynamics and workings of transpiration experiments are outlined. It is important to note that none of the work presented in this chapter is attributable to the author.

Background

Stainless steels are among the most widely used materials in the modern world. These iron-based metal alloys are so attractive due to their low costs and stability over a large temperature range, from cryogenic conditions to temperatures exceeding 1000°C [6,7]. This stability is due to the ability of stainless steels to form a surface passivation layer in the presence of oxygen, which acts as a protective barrier against corrosion of the underlying alloy. This corrosion resistance, in addition to availability and cost, largely explains why applications ranging from combustion engines, to skyscraper construction, to refrigeration units use stainless steels as materials of construction. Different grades, or types, of stainless steel may be used depending on specific application requirements to ensure sufficient corrosion resistance, retention of mechanical properties, and minimal reactivity with the surrounding system.

There are five main classes of stainless steel: austenitic, ferritic, martensitic, precipitation hardening, and duplex. Austenitic stainless steels have a face centered cubic structure stabilized by manganese and nitrogen in the 200 series and nickel in the 300 series, with chromium content ranging from 16-28%. These alloys offer excellent corrosion resistance and formability. Ferritic stainless steels have a body centered cubic structure and possess a chromium range of 10.5-30%. These alloys do not retain their strength at high temperatures as austenitic alloys do but are lower cost and offer excellent resistance to stress corrosion cracking. Martensitic stainless steels have a body centered tetragonal structure with 11.5-18% chromium content. These alloys have a high carbon content allowing for enhanced hardness but diminished ductility. Precipitation hardening

stainless steels are a class of martensitic or austenitic stainless steels which are heat treated with additions such as titanium, copper, molybdenum, and/or aluminum to form precipitates which increases strength and hardness at the cost of toughness. Duplex stainless steels possess both austenitic and ferritic stainless steel structures to obtain mixed behavior.

For all of these classes of stainless steel chromium plays an important role in passivation of the alloy. There exist conditions, however, which may disrupt surface passivation layers and subsequently compromise the integrity of the underlying alloy by encouraging volatilization, or reactive evaporation, of the passivation layer. This is especially true for chromia formers, stainless steels which show a propensity for chromium(III) oxide formation as the passivation layer. Upon volatilization, the formerly protective chromia layer may transform into a highly mobile vapor species, which may interact with the surrounding system in detrimental fashion. These interactions pose challenges to human health, the environment, and in electrochemical devices, e.g. solid oxide fuel cells.

Impacts of the Reactive Evaporation of Chromium

Human Health and the Environment. Chromium compounds often have a trivalent or hexavalent oxidation state. Trivalent chromium is a necessary trace nutrient and is not hazardous to the environment at large [8]. Hexavalent chromium, however, is toxic and a known carcinogen [9]. It is also primarily generated in man-made processes, as opposed to trivalent chromium which is naturally occurring [10]. Processes such as leather

tanning, electroplating, textile manufacturing, and stationary fuel combustion are largely responsible for annual environmental releases [10]. The maximum contaminant level for total chromium in drinking water is 0.1 mg/L [8]. The permissible exposure limit to which a worker may be exposed to airborne chromic acid, and/or chromates over the course of eight hours, is 5 $\mu g/m^3$ [8]. This limit is two orders of magnitude greater for trivalent chromium species [8]. Unfortunately, due to corporate nonfeasance or malfeasance, these limits are occasionally exceeded. Conditions exceeding prescribed limits are toxic and/or mutagenic for plants, microbes, animals, and humans [8-10].

High Temperature Corrosion of Ferritic Stainless Steel. Ferritic stainless steel is a high chromium (10-27%), low carbon ($\leq 0.1\%$) steel with a body centered cubic structure. This combination of traits allows for excellent oxidation and stress corrosion cracking resistance, in addition to relatively good machinability and formability. When exposed to an oxidizing atmosphere, the chromium in the steel reacts with oxygen at the surface to form a passive layer of chromia (Cr_2O_3). If manganese is present in the steel, then a duplex structure may form at the surface with Cr-Mn spinel ($(Cr,Mn)_3O_4$) as a top layer, and chromia beneath it [11-13]. These dense oxide layers serve as a protective barrier against inward oxygen transport, thus slowing the rate of corrosion.

These protective layers are susceptible to failure through several modes. Spallation, or delamination, which will be discussed further in Chapter 2, is one such failure mode. An oxide scale segment that undergoes spallation detaches from the alloy, exposing the underlying alloy to the environment. A sufficient concentration of

chromium, however, endows the alloy with a self-healing quality. Chromium may diffuse to the spalled region and react with oxygen to quickly reform the protective oxide scale. At high temperature (≥500°C), and in the presence of oxygen and water vapor, however, reactive evaporation of chromium may compromise intact oxide scale integrity, or oxide scale reformation. An oxide scale in the form of chromia will undergo reactive evaporation to form chromium oxyhydroxide as a product. If chromia volatilizes more quickly than it may be replenished in the scale, then the formerly protective oxide will breakdown and a less protective scale, such as $(Fe,Cr)_2O_3$ or iron oxides, will form [14-16]. These less protective oxides may lead to localized breakaway corrosion of the alloy, thus altering the material properties of the alloy in service. Selecting an alloy susceptible to this mode of degradation may make an application unpractical, unaffordable, and/or unsafe. As will be discussed in Chapter 2, some oxides, such as several spinel and perovskite phases [17-20], are more resistant to chromium volatility than chromia and may prevent/minimize the breakdown in protective behavior noted here.

Solid Oxide Fuel Cell Degradation. Solid oxide fuel cell (SOFC) technology offers high efficiency and flexible energy conversion of fuels into heat and electricity. Operating at high temperature (650-1000°C), SOFCs may oxidize carbon monoxide, hydrocarbons, and/or hydrogen to produce electricity, heat and carbon dioxide and/or water, depending on the fuel [21]. A simplified schematic of a SOFC using hydrogen as fuel is shown in Figure 1.

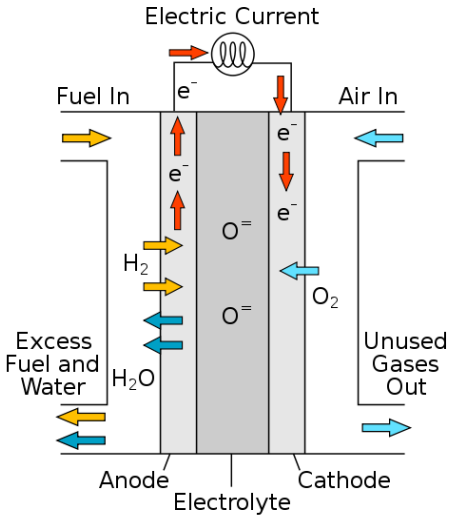


Figure 1 - Schematic of a SOFC using hydrogen as fuel.

As seen in Figure 1, a SOFC consists of two electrodes separated by an oxide ion conducting electrolyte, commonly yttria-stabilized zirconia (YSZ) [21]. Hydrogen is oxidized at the anode/YSZ interface and the electrons created serve to generate a current, and reduce oxygen at the cathode/YSZ interface. The latter interface is often referred to as the triple phase boundary (TPB) as this is where the gas phase, electrolyte, and cathode meet. One cell, consisting of the anode, cathode, and electrolyte, produces less than 1 Volt [22]. For practical use of SOFC technology, cells must be stacked and interconnected to obtain higher voltage and power. Lower operating temperatures (≤ 800°C) allow for the use of metallic interconnects, such as ferritic stainless steel, which meets many of the interconnect requirements [23]. At these temperatures, however, interconnects exposed to air on the cathode side may evolve volatile chromium species in the form of chromium trioxide and/or chromium oxyhydroxide. These volatile species may then proceed to deposit on the cathode, with both chemical and electrochemical

deposition noted in literature [24-27]. Deposition has been noted to occur at the TPB, or at a cathode/gas, electrolyte/gas two phase boundary. This deposition diminishes SOFC performance over time. Acceptable performance degradation, as outlined by the US Department of Energy, is reliable lifetime degradation of less than 0.2% per 1000 hours over 40,000 hours of operation [28]. Progress towards this goal is underway, with an example being the Jülich Research Centre reporting less than 0.1% performance degradation per 1000 hours for stacks operated for 17000 and 19000 hours [29,30]. Both operated under a current load of 0.5 A cm^{-2} at 700°C and used H_2/3% H_2O as fuel. Successful demonstrations like these offer promise for SOFC technologies; however, long-term operation with conventional fuels in real-world conditions are needed. Understanding degradation phenomena, like chromium poisoning are requisite in this pursuit.

Reactive Evaporation

Given high temperature (≥500°C) oxidizing environments, a chromia scale will be subject to reactive evaporation in accordance with Equation 1.1 [31-33].

$$\frac{1}{2}Cr_2O_3(s) + \frac{3}{4}O_2(g) = CrO_3(g) \qquad (1.1)$$

If, however, water vapor is also present, then the dominant volatilization pathway will proceed according to Equation 1.2 [31-36].

$$\frac{1}{2}Cr_2O_3(s) + \frac{3}{4}O_2(g) + H_2O(g) = CrO_2(OH)_2(g) \qquad (1.2)$$

These conclusions have been drawn from transpiration experiments in addition to thermodynamic modeling.

Transpiration Method. In a transpiration experiment, volatile species are generated by flowing a reactant gas over a compound of interest in a furnace. The compound of interest here is chromia, and the reactant gas is either dry air or humidified air. These gases may react with chromia, as seen in Equations 1.1 and 1.2, to form volatile chromium species in the form of chromium trioxide and chromium oxyhydroxide, respectively. Once generated, these species may diffuse through the boundary layer, and become entrained in the bulk flow. As the vapor species proceed further and further downstream, the temperature continues to drop. Some of the volatile species may react with the tube walls at elevated temperatures, but the majority of the volatile species deposit in the region of the tubes which are at or below the condensation point of the vapor [31, 37]. Figure 2 displays a schematic of transpiration equipment used by Opila et al. [31] for clarification.

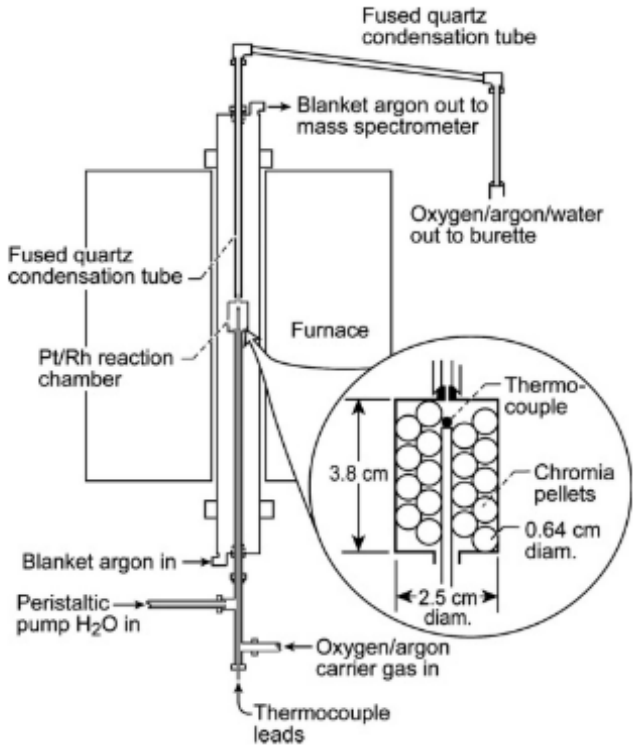


Figure 2 - Transpiration equipment used by Opila et al. [31].

At the conclusion of the experiment, condensed chromium may be collected from quartz tubing using solvents such as water, nitric acid, or hydrofluoric acid [31, 37, 38]. Dissolved chromium may then be quantified using a technique such as inductively coupled plasma mass spectroscopy. This quantified condensate may be used to determine the partial pressure of volatile chromium species using the ideal gas law as shown in Equation 1.3.

$$P_{Cr-O-H} = \frac{\dot{n}_{Cr} RT}{\dot{V}} \tag{1.3}$$

$P_{Cr\text{-}O\text{-}H}$ – Partial pressure of volatile chromium species

$\dot{n}_{Cr}$ – Molar flow rate of chromium

R – Gas constant

T – Temperature

$\dot{V}$ – Total volumetric flow rate

To solve for the partial pressure of volatile chromium species in Equation 3, one must first determine the molar flow rate of chromium and the total volumetric flow rate. This can be done using Equations 1.4 and 1.5.

$$\dot{n}_{Cr} = \frac{m_{Cr}}{M_{Cr} t} \tag{1.4}$$

$$\dot{V} = \frac{RT(\dot{n}_{O_2} + \dot{n}_{H_2O} + \dot{n}_{Cr-O-H})}{P} \tag{1.5}$$

m_{Cr} – Mass of chromium

M_{Cr} – Molar mass of chromium

t – Time

P – Total pressure

$\dot{n}_{O_2}$ – Molar flow rate of oxygen

$\dot{n}_{H_2O}$ – Molar flow rate of water

$\dot{n}_{Cr-O-H}$ – Molar flow rate of volatile chromium species

With this ability to calculate the partial pressure of volatile chromium species, one may test to see if Equation 1.1 or 1.2 is dominant, or even valid, in an environment with humidified air, as Opila et al. did [31]. A series of transpiration experiments were performed using chromia pellets as a Cr source at 600°C. To determine oxygen and water dependency, experiments were performed in two sets: One set of experiments held the oxygen partial pressure constant and varied the partial pressure of water. The other set did the opposite, holding the partial pressure of water constant and varying the oxygen

partial pressure. The resulting partial pressure of volatile chromium species was plotted for each run on a log-log plot, as can be seen in Figures 3 and 4.

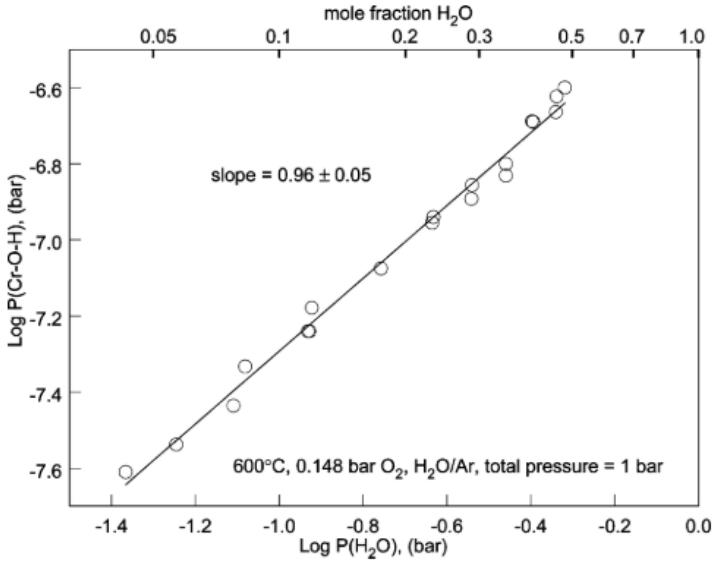


Figure 3 - From Opila et al. [31]. Log-log plot of volatile chromium species partial pressure against varied water partial pressure.

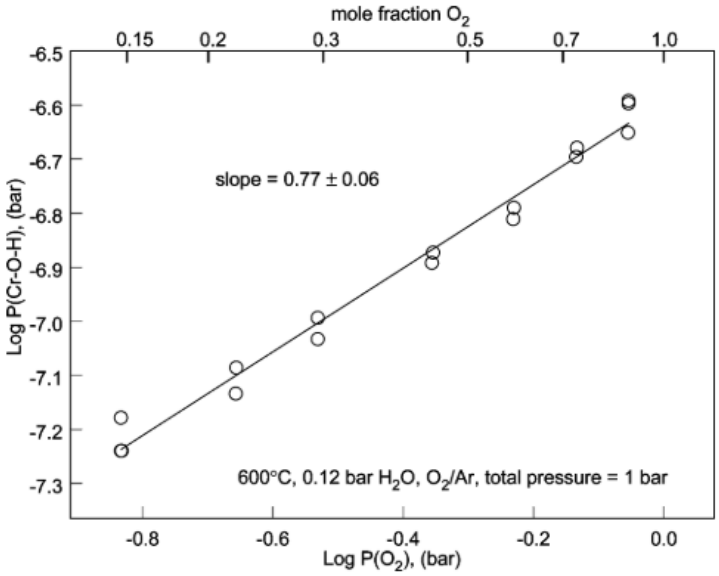


Figure 4 - From Opila et al. [31]. Log-log plot of volatile chromium species partial pressure against varied oxygen partial pressure.

Examining Figures 3 and 4, best fit lines give a slope of 0.96 ± 0.05 and 0.77 ± 0.06, respectively. Recall from Equation 1.2, that the stoichiometric coefficients for water vapor and oxygen are 1 and 0.75, respectively. Slopes on log-log plots are indicative of monomial relationships shown by Equations 1.6 and 1.7.

$$P_{Cr-O-H} \propto P_{H_2O}^{0.96\pm0.05} \tag{1.6}$$

$$P_{Cr-O-H} \propto P_{O_2}^{0.77\pm0.06} \tag{1.7}$$

Equations 1.6 and 1.7 show the empirically derived power law exponents match those expected from Equation 1.2 within a 95% confidence interval. This result shows the dominance of Equation 1.2 over Equation 1.1 at 600°C, though the study's authors believe it to be representative of a broader temperature range, as a control experiment using dry air at 900°C yielded a contribution to the total volatility of 1% or less from CrO_3. Additionally, the study's authors performed transpiration experiments at temperatures ranging from 300-900°C, and calculated an equilibrium constant for each run. The natural log of these equilibrium constants were plotted against inverse temperature as shown in Figure 5. The slope and y-intercept relate to the enthalpy and entropy, respectively, through a form of the van't Hoff expression shown in Equation 1.8.

$$\ln K_p = -\frac{\Delta H^o}{R}\left(\frac{1}{T}\right) + \frac{\Delta S^o}{R} \tag{1.8}$$

K_p – Equilibrium constant

ΔH^o – Standard state enthalpy change

ΔS^o – Standard state entropy change

Equation 1.8 may be derived from Gibbs free energy expressions, with Gibbs free energy being rooted in the second law of thermodynamics.

$$\Delta S_{universe} > 0 \tag{1.9}$$

$$\Delta S_{universe} = \Delta S_{surroundings} + \Delta S_{system} \tag{1.10}$$

$$\Delta S_{surroundings} = \frac{-\Delta H}{T} \tag{1.11}$$

$$\Delta G = -T\Delta S_{universe} = \Delta H - T\Delta S_{system} \tag{1.12}$$

$\Delta S_{universe}$ – Entropy change of the universe

$\Delta S_{surroundings}$ – Entropy change of the surroundings

ΔS_{system} – Entrophy change of the system

Given a standard reference state, Equation 1.12 becomes Equation 1.13.

$$\Delta G^o = \Delta H^o - T\Delta S^o \tag{1.13}$$

An alternative definition of Gibbs free energy is shown in Equation 1.14.

$$\Delta G = \Delta G^o + RTlnQ \tag{1.14}$$

Q – Reaction quotient

At equilibrium ΔG = 0.

$$\Delta G^o = -RTlnK \tag{1.15}$$

Combining Equations 1.13 and 1.15 yields the form of the van't Hoff expression in Equation 1.8.

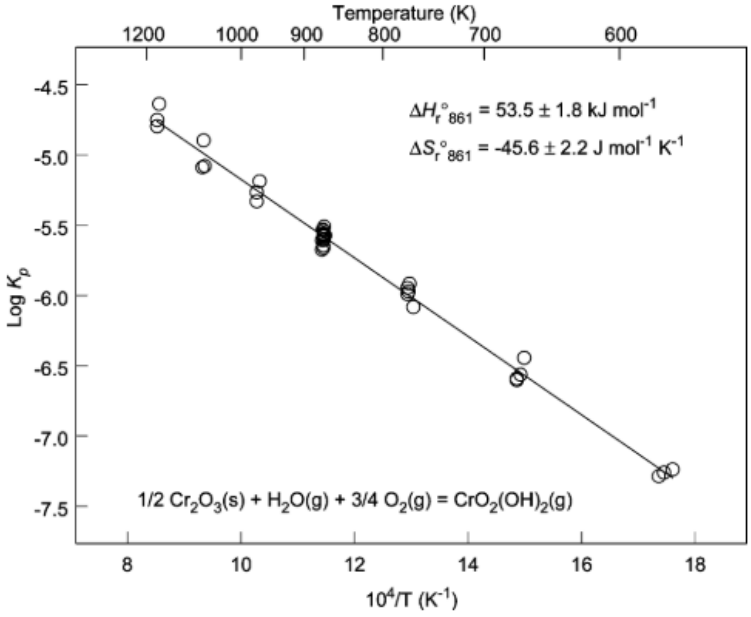


Figure 5 - From Opila et al. [31]. The natural log of equilibrium constants plotted against inverse temperature.

The study's authors noted that the linear fit in Figure 5 holds well over the entire temperature range, and thus the volatilization mechanism is not measurably altered from 300-900°C.

Thermodynamic Modeling. In thermodynamic modeling, thermodynamic principles are used to predict the most stable arrangement in a given system. This may be done by minimizing Gibbs free energy in keeping with the second law of thermodynamics. As a reminder, the systems of interest are given in Equations 1.1 and 1.2, restated here.

$$\frac{1}{2}Cr_2O_3(s) + \frac{3}{4}O_2(g) = CrO_3(g) \quad (1.1)$$

$$\frac{1}{2}Cr_2O_3(s) + \frac{3}{4}O_2(g) + H_2O(g) = CrO_2(OH)_2(g) \quad (1.2)$$

These systems involve modeling a condensed phase (chromia) with a gas phase. The Gibbs free energy for an ideal gas mixture is given in Equation 1.16.

$$\bar{G}_k = u_k = RTlnp_k + \lambda_k(T) \tag{1.16}$$

$\bar{G}_k$ – Partial molar Gibbs energy of component "k" in a mixture

u_k – Chemical potential of component "k"

p_k – Partial pressure of component "k"

$\lambda_k(T)$ – Chemical potential of pure "k" in an ideal gas state at T and P=1 bar

Including the condensed phase, the total Gibbs free energy of the system may be represented by Equation 1.17.

$$G = RT \cdot \left(\sum_{k=1}^{m} n_k^g \left[\left(\frac{\mu^o}{RT} \right)_k^g + lnP + lnx_k^g \right] + \sum_{k=1}^{s} n_k^c \left(\frac{\mu^o}{RT} \right)_k^c \right) \tag{1.17}$$

G – Total Gibbs free energy

n_k^g – Moles of component "k" in gas phase

n_k^c – Moles of component "k" in condensed phase

$\left(\frac{\mu^o}{RT}\right)_k^g$ – Chemical potential of pure component "k" in gas phase, divided by RT

$\left(\frac{\mu^o}{RT}\right)_k^c$ – Chemical potential of pure component "k" in condensed phase, divided by RT

P – System pressure

x_k^g – Mole fraction of component "k" in gas phase

In words, Equation 1.17 states that the summation of chemical potentials, multiplied by their respective molar quantities, will yield the total Gibbs free energy of

the system. In the gas phase, each component chemical potential is adjusted by its partial pressure in the gas phase, in line with Equation 1.16. Since this is giving the ideal gas case, the partial pressure is being used in place of fugacity. There is no chemical potential adjustment in the condensed phase, as pure chromia is being considered, therefore having a chromia activity equal to one.

To find the minimum Gibbs free energy, the method of Lagrange undefined multipliers may be used. In this method, a function of interest, in this case Equation 1.17 defined above, is placed under some constraint. In this case, Equation 1.18 represents the constraint in the form of a mass balance.

$$\psi(n) = \left(\sum_{k=1}^{m+s} a_{kj} n_k - b_j \right)_{j=1}^{NC} = 0 \tag{18}$$

m – Number of components in gas phase

s – Number of components in condensed phase

k – Component “k”

a_{kj} – Number of atoms of element “j” in a molecule of component “k”

n_k – Moles of component “k”

b_j – Total quantity of element “j” in the system

NC – Number of components in the system

In words, Equation 1.18 is a constraint on the system to conserve mass. It states the summation of any given element in the system, given all phases and components, will equal the total quantity of that element in the system. This constraint may be used to construct the Lagrangian expression in Equation 1.19.

$$\mathcal{L}(n,\lambda) = F(n) - \lambda \cdot \psi(n) \tag{1.19}$$

$$F(n) = \frac{G}{RT} \tag{1.20}$$

λ – Lagrange multiplier

The Lagrange multiplier is a proportionality constant which relates the mass balance ($\psi(n)$) to the total Gibbs free energy divided by RT ($F(n)$). To minimize the Gibbs free energy, the gradient of Equation 1.19 must be taken and set equal to zero, as shown in Equations 1.21-1.25.

$$\nabla\mathcal{L}(n,\lambda) = 0 = \nabla F(n) - \lambda \cdot \nabla\psi(n) \tag{1.21}$$

$$\nabla F(n) = \lambda \cdot \nabla\psi(n) \tag{1.22}$$

$$\left(\frac{\partial \mathrm{F}}{\partial n_k}\right)_{T,P}^{g} = \left(\frac{\mu^o}{RT}\right)_k^{g} + \ln P + \ln \frac{n_k}{\sum_{k=1}^{m} n_k} \tag{1.23}$$

$$\left(\frac{\partial \mathrm{F}}{\partial n_k}\right)_{T,P}^{c} = \left(\frac{\mu^o}{RT}\right)_k^{c} \tag{1.24}$$

$$\lambda \cdot \left(\frac{\partial \psi}{\partial n_k}\right)_{T,P} = \sum_{j=1}^{NC} a_{kj}\lambda_j \tag{1.25}$$

Putting everything together, the gas phase, condensed phase, and atom balances are displayed in Equations 1.26-1.28.

$$\text{Gas phases: } \left(\frac{\mu^o}{RT}\right)_k^{g} + \ln P + \ln \frac{n_k}{N} - \sum_{j=1}^{NC} a_{kj}\lambda_j = 0 \tag{1.26}$$

$$\text{Condensed phase: } \left(\frac{\mu^o}{RT}\right)_k^{c} - \sum_{j=1}^{NC} a_{kj}\lambda_j = 0 \tag{1.27}$$

$$\text{Atom balance: } \left(\sum_{k=1}^{m+s} a_{kj} n_k - b_j\right)_{j=1}^{NC} = 0 \tag{1.28}$$

For Equation 1.1, "j" includes Cr and O, whereas for Equation 1.2, "j" includes Cr, O, and H. Likewise, for Equation 1.1 "k" includes Cr_2O_3(s), O_2(g), and CrO_3(g), whereas for Equation 1.2 "k" includes Cr_2O_3(s), O_2(g), H_2O(g), and $CrO_2(OH)_2$(g). Entering these elements and compounds, a system of equations is generated which may be solved simultaneously. Equations 1.27 and 1.28 are linear, but Equation 1.26 is non-linear. To develop a system of linear equations, Equation 1.26 must be linearized, with one method being to use a Taylor series expansion for the natural log term in Equation 1.26. The general form of the Taylor series is given in Equation 1.29.

$$\sum_{n=0}^{\infty} \frac{f^{(n)}(a)}{n!}(x-a)^n \tag{1.29}$$

In words, Equation 1.29 is an approximation of f(x) at point "a". This approximation is obtained by summing f(a) and its subsequent derivatives until a desirable level of error tolerance is met. Up to the first derivative term is shown in the Taylor series expansion for ln(n_k) in Equation 1.30.

$$\ln n_k \approx \ln y_k + \frac{n_k - y_k}{y_k} = \ln y_k + \frac{x_k}{y_k} - 1 \tag{1.30}$$

$n_k(0) = y_k$

Substituting this approximation into Equation 1.26, and given mathematical manipulation, the linearized form of Equation 1.26 can be obtained, and is displayed in Equation 1.31. The mathematical steps are available in Appendix D of reference [39].

$$\sum_{i=1}^{NC} \lambda_i \sum_{k=1}^{m} a_{kj} a_{ki} y_k + \left[\frac{N}{Y} - 1\right] \sum_{k=1}^{m} a_{kj} y_k + \sum_{k=m+1}^{m+s} a_{ij} n_k = \sum_{k=1}^{m} a_{kj} f_k - C_j \quad (1.31)$$

$$f_k = y_k \left[\left(\frac{\mu^o}{RT} \right)_k^g + \ln P + \ln \frac{y_k}{Y} \right] \quad (1.32)$$

$$C_j = \sum_{k=1}^{m} a_{kj} y_k - b_j, j = 1, \ldots, NC \quad (1.33)$$

Y – Summation of all y_k values

Equations 1.27, 1.28, and 1.31 may be solved simultaneously to obtain intensive and extensive variables of interest. The results of this modeling can be seen in Figure 6 from Jacobson et al. [32].

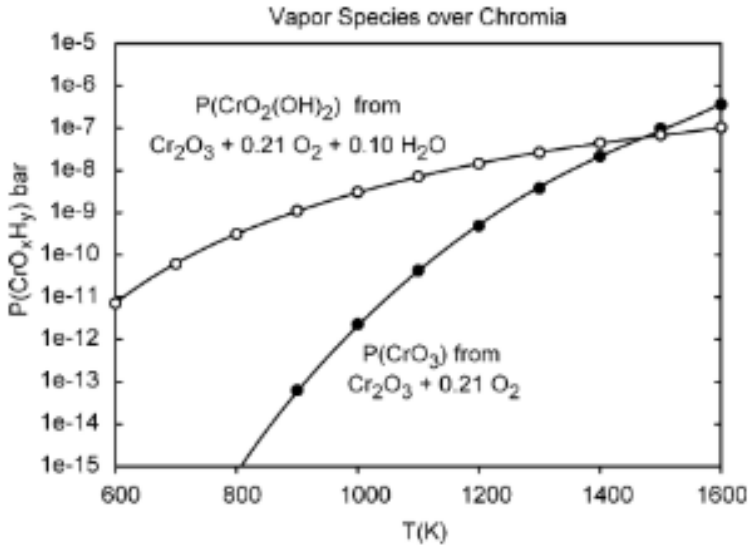


Figure 6 - From Jacobson et al. [32]. Thermodynamic modeling of Equations 1.1 and 1.2.

From the modeling displayed in Figure 6, the vapor pressure of $CrO_2(OH)_2$(g) is greater than the vapor pressure of CrO_3(g) over chromia up to around 1400 K. It should be noted

that vapor pressure approximations based on thermodynamic modeling may vary depending on the thermodynamic data set used.

The disparate vapor pressure behavior of $CrO_2(OH)_2(g)$ and $CrO_3(g)$ is interesting, as $CrO_2(OH)_2(g)$ is a larger compound than $CrO_3(g)$. Generally speaking, there is an inverse relationship between the vapor pressure of a compound and its size due to the greater London dispersion forces afforded to a bigger molecule with more electrons [39]. This trend does not hold for all cases, for example CF_4 is larger than CHF_3, but since the latter is a polar molecule it has a lower vapor pressure [40, 41]. It may also be noted that a similar trend of thermodynamic stability and vapor pressure appears to match the vapor pressure trend mentioned above. Comparing alkanes with alkanes, alkenes with alkenes, alkynes with alkynes, and alcohols with alcohols, Gibbs energy of vaporization becomes less favorable with increasing size within each category [39]. Unfavorable free energy of vaporization corresponds with an unstable product in the gas phase relative to the liquid phase, corresponding with a lower vapor pressure. This matches the inverse relationship trend between vapor pressure and size of a molecule.

Volatility will be dependent on both the stability of the vapor phase compound, and the intermolecular forces preventing the volatilization of said compound. Differences in vapor pressure between CrO_3 and $CrO_2(OH)_2$ may be attributable to both stability and intermolecular forces. Johnson and Panas [43, 44] propose a mechanism in which oxygen first reacts with chromia to form surface CrO_3 species for both wet and dry conditions. These species form -O-(CrO_2)-O-(CrO_2)-O repeating units with a given vapor pressure at a given temperature (see vapor pressure estimate of CrO_3 in Figure 6). Conversion from

CrO_3 to $CrO_2(OH)_2$ may occur through hydrolysis reactions with surface repeat units, resulting in the severing of Cr-O-Cr bonds and formation of $CrO_2(OH)_2$. If CrO_3 first volatilizes, then a gas phase hydrolysis reaction may occur to form $CrO_2(OH)_2$. These reactions were observed to be exothermic which coincides with the gap between the equilibrium partial pressures of the two volatile species in Figure 6 closing with increasing temperature. Figure 6 does not account for this interplay between the two volatile species, however, and is strictly derived from an examination of the thermodynamic stability of the two molecules. The decreasing partial pressure difference in Figure 6 is likely due to the unfavorable entropy of $CrO_2(OH)_2$ formation becoming more significant with increasing temperature. Though the question may be explored in greater detail elsewhere, for the purpose of this study the difference in vapor pressure of CrO_3 and $CrO_2(OH)_2$ will be attributed primarily to two factors: hydrolysis facilitated dissociation reactions for $CrO_2(OH)_2$, and greater thermodynamic stability of $CrO_2(OH)_2$ (up to around 1400 K).

Thesis Statement

Volatile chromium species deposition on a material may be influenced by temperature and time, but the most germane dependency is the material on which reactive condensation will occur. More specifically, the surface hydroxyl population/properties of a material will have the most influence on chromium deposition. As chromium deposition is a surface phenomenon, hydroxyl groups serve as anchoring points which possess an affinity for volatile chromium species, and little steric inhibition relative to positions in a

crystalline lattice or amorphous structure. Chromium deposition will increase with increasing surface hydroxyl populations and basicity [45-51].

CHAPTER TWO

REACTIVE EVAPORATION OF CHROMIUM FROM FERRITIC STAINLESS STEEL

Content in Chapter Two

Chapter Two contains information on basic concepts in materials science and fluid mechanics, literature reporting relevant to the reactive evaporation of chromium from ferritic stainless steel, and a first authored paper published in Oxidation of Metals [1]. Concepts covered include crystallographic planes, grain structure, lattice diffusion mechanisms, kinetics, metal oxidation theory, basics of fluid mechanics, and spallation. These concepts are necessary to understand literature presented in this dissertation and so are included, though experts in these areas may proceed to the literature review section beginning in Influence of Water Vapor, after the derivation of Equation 2.55.

There are several important notes to be made for optimal reader comprehension. Equations are presented for an understanding of the relevant fundamental science, not for use in the research performed in this dissertation. Next, five classes of stainless steels were outlined in the first chapter, but the focus here is on ferritic stainless steel. This is due to its prevalence as an interconnect material in SOFCs and exhaust systems in automobiles, both of which are relevant to the reactive evaporation and/or condensation of chromium vapor species. Lastly, the only work performed by the author of this dissertation is presented in Influence of Ceramic Contacting Conditions beginning at Table 1.

Basic Material Science of Ferritic Stainless Steel

Ferritic stainless steel has a body centered cubic (BCC) structure and is comprised primarily of iron and chromium. An illustration of a BCC unit cell is given in Figure 7.



Figure 7 – Body centered cubic structure. Credit: chem.libretexts.org.

Unit cells are the smallest divisible frame of atoms which maintain the long range order of a crystalline material. When stacked with one another in the same orientation, unit cells make up a single BCC crystal. Ferritic stainless steels are typically polycrystalline, however, which are comprised of many crystal grains of random, or preferred, orientation. These orientations may be described using a notation system known as Miller indices. The indices may be used to describe crystallographic planes as can be seen in Figure 8.

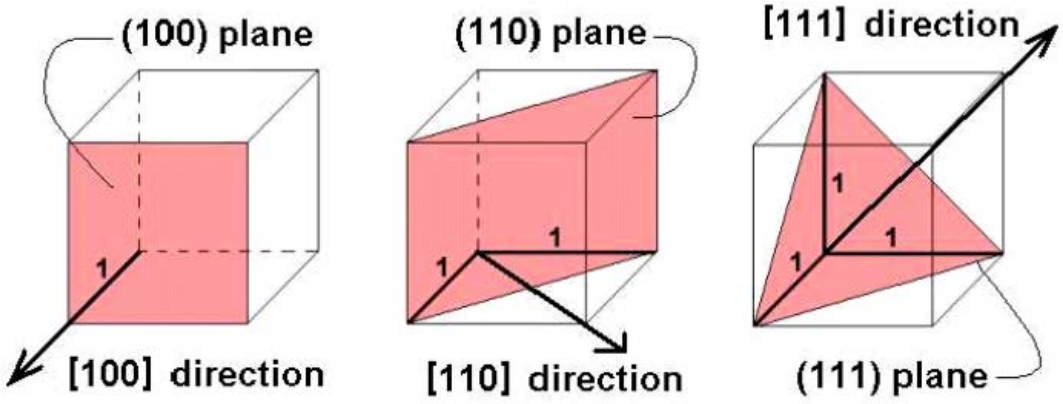


Figure 8 - Miller indices.

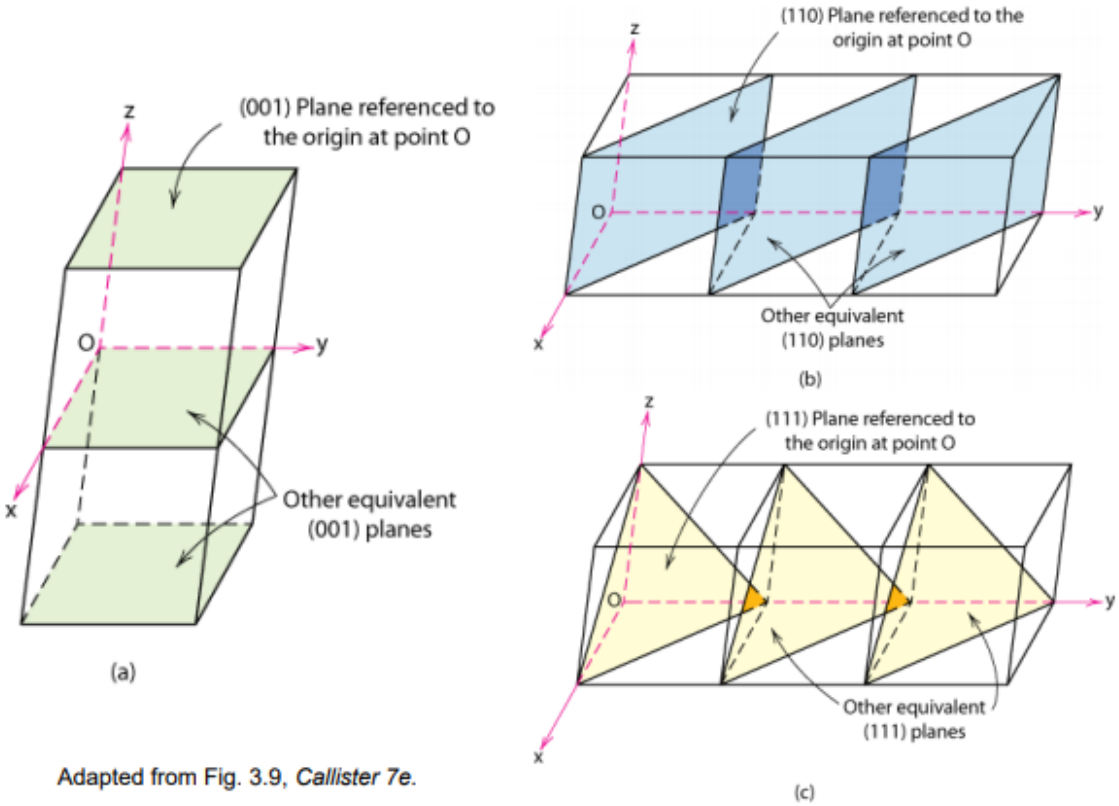


Figure 9 – Crystal planes.

Three sets of stacked BCC unit cells, oriented in accordance with Figure 9, may be imagined to mismatch at the boundaries as shown in Figures 10 and 11. Where these differently oriented grains meet are known as grain boundaries.

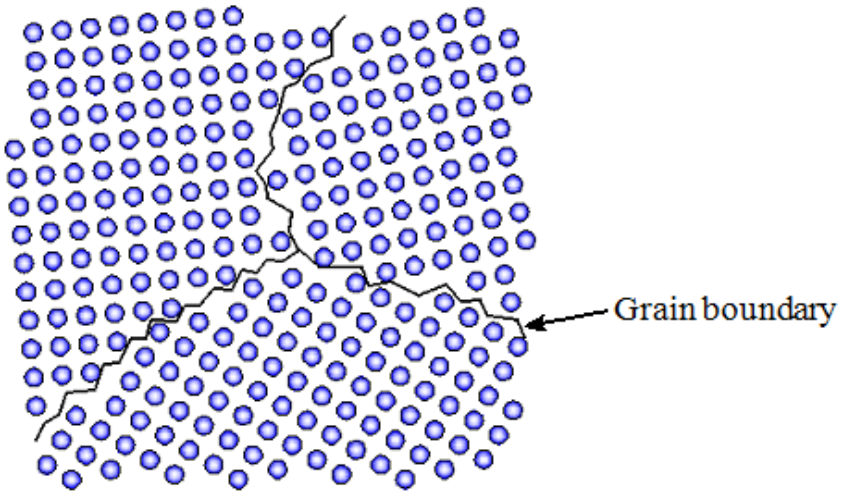


Figure 10 - Grain boundary illustration. Credit: engineeringarchives.com.

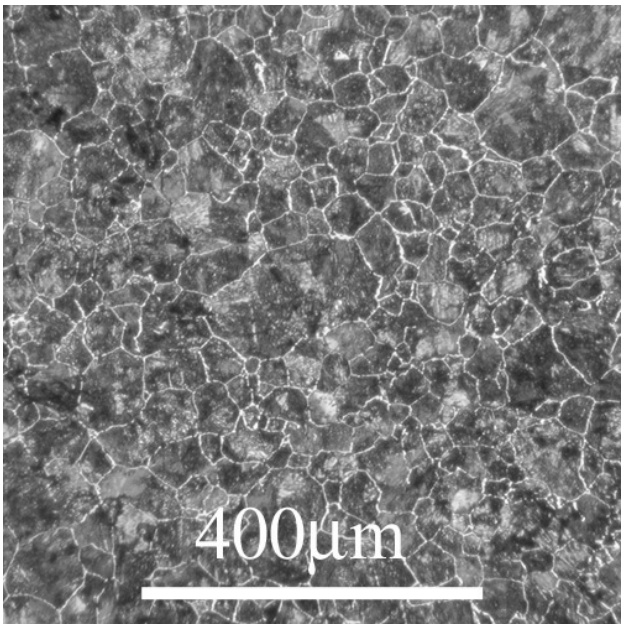


Figure 11 - Grain boundary micrograph. Credit: doitpoms.ac.uk.

Grain boundaries are not the only crystallographic defects present. It is also necessary to understand point and linear defects to understand stainless steel and its behavior. Carbon is an interstitial impurity atom in the α-iron lattice (BCC) which occupies octahedral positions of the unit cell. There is an octahedral site on each face of the unit cell. With carbon uptake into these interstitial positions, the lattice distorts and is strengthened in the form of steel. The max solubility of carbon in α-iron is 0.022 wt% in order to maintain a BCC structure.

Carbon fit into interstitial positions as it is much smaller than iron. Chromium is larger than iron and therefore substitutes into vacant positions. Vacancies are atom positions in the lattice which are not occupied. Vacant positions are generated due to their contribution to minimization of Gibbs free energy from configurational and vibrational entropy, but are attenuated by the energy required for vacancy formation. The entropic and energetic considerations combine to provide a given concentration of vacancies at a given temperature, as can be seen in Equations 2.1-2.5. 33-37.

$$\Delta G = n\left(\Delta h_f - T\Delta s_v\right) - T\Delta S_c^n \tag{2.1}$$

$$S_c^n = k_B \ln\left(\frac{N!}{n!\,(N-n)!}\right) \tag{2.2}$$

$$\frac{\partial S_c^n}{\partial n} \approx -k_B \ln\left(\frac{n}{N}\right) \tag{2.3}$$

$$\frac{\partial G}{\partial n} = 0 = \Delta h_f - T\Delta s_v + k_B T \ln\left(\frac{n_{eq}}{N}\right) \tag{2.4}$$

$$\frac{n_{eq}}{N} = \exp\left(\frac{\Delta s_v}{k_B}\right) \cdot \exp\left(-\frac{\Delta h_f}{k_B T}\right) \tag{2.5}$$

n – Number of vacancies

n_{eq} – Number of vacancies at thermodynamic equilibrium

N – Total number of lattice sites

Δh_f – Energy of vacancy formation

Δs_v – Change in vibrational entropy due to introduction of one vacancy

ΔS_c^n – Change in configurational entropy due to introduction of n vacancies

k_B – Boltzmann constant

Taking the derivative of Gibbs free energy with respect to vacancies and setting it equal to zero minimizes Gibbs free energy, as the second derivative of Equation 2.4 is positive. Vacancies may be generated or consumed at interfaces such as grain boundaries or dislocations. Dislocations are linear regions of atoms which are out of position in the lattice. Shear stresses within the lattice may form edge or screw dislocations, with edge dislocations moving parallel to the stress and screw dislocations moving perpendicular. This difference may be visualized using Figure 12.

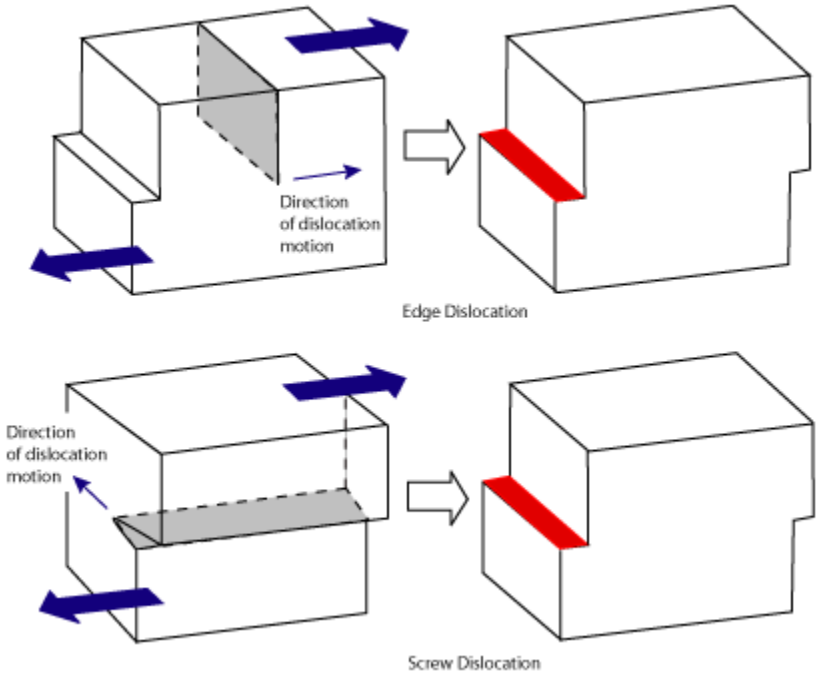


Figure 12 - Edge and screw dislocations. Credit: nde-ed.org.

Dislocations may move through mechanisms of slip or climb. Slip refers to slip planes, which are planes in a lattice which have the highest density of atoms. Movement along these planes is illustrated in Figure 13 where a few atoms in a dislocation may break and reform bonds to begin shifting the dislocation.

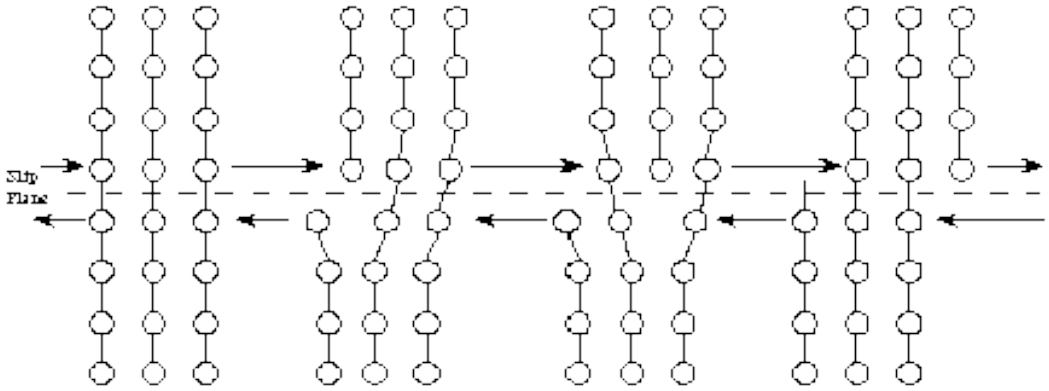


Figure 13 - Dislocation motion through slip.

Alternatively, dislocations may move by climb, which is not dependent on the slip plane. Dislocations may experience positive or negative climb if acting as a vacancy sink or source, respectively. This may be visualized in Figure 14.

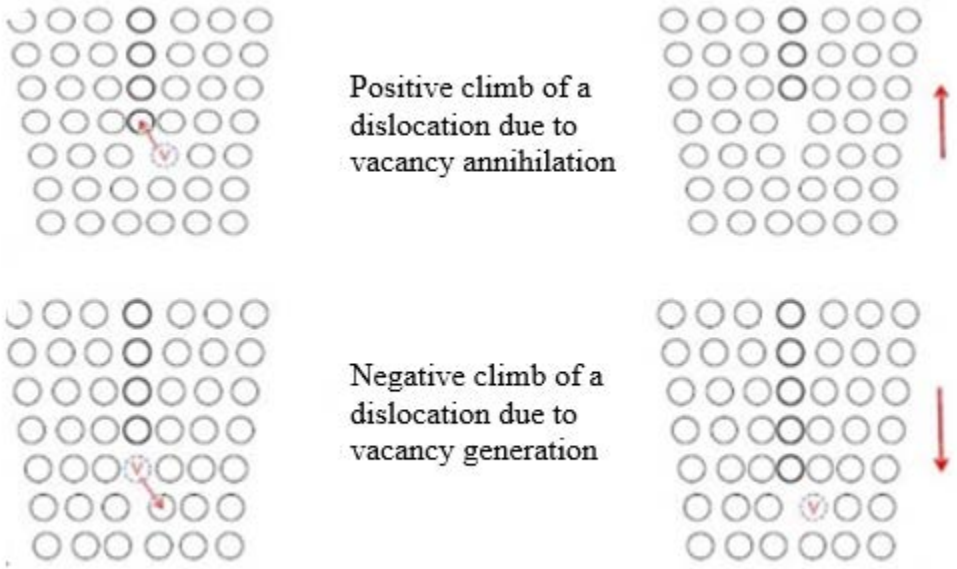


Figure 14 - Dislocation climb.

Diffusion of atoms within a lattice may be described using Fick's first law (Equation 2.6), and Fick's second law (Equation 2.8) which may be derived from the first law and the continuity equation (Equation 2.7).

$$J = -D\nabla C \tag{2.6}$$

$$\frac{\partial C}{\partial t} + \nabla \cdot J = 0 \tag{2.7}$$

$$\frac{\partial C}{\partial t} = \nabla \cdot (D\nabla C) \tag{2.8}$$

D – Diffusion coefficient

C – Concentration

J – Molecular flux

The diffusion coefficient depends on temperature, crystal structure, concentration, and composition. These dependencies may be approximated by taking into account the probability of finding a vacancy adjacent to the diffusing species, and the frequency of jump attempts by the diffusing species.

$$P = z \cdot \exp\left(-\frac{Q_v}{k_B T}\right) \tag{2.9}$$

$$R_j = R_0 \cdot \exp\left(-\frac{E_m}{k_B T}\right) \tag{2.10}$$

$$D \approx D_0 \cdot \exp\left(-\frac{Q_d}{k_B T}\right) \tag{2.11}$$

P – Probability of finding an adjacent vacant site

R_j – Frequency of jumps with sufficient thermal energy

R_0 – Attempt frequency related to frequency of atomic vibration

z – Coordination number of vacancy position

D_0 – $R_0 \cdot z$, or temperature independent diffusion parameter

Q_v – Necessary energy for vacancy formation

E_m – Necessary energy for jump into vacant position

Q_d – $E_m + Q_v$, or energy necessary for diffusion

As a general rule diffusion will occur most swiftly on the surface, followed by grain boundary and dislocation diffusion. The slowest route being diffusion through the lattice volume. The less restrictive the structural region, the faster the rate of diffusion.

Behavior of Ferritic Stainless Steel at High Temperature

As was noted in the previous section, an increase in temperature will increase the rate of diffusion of atoms. Temperature increases will also increase the rate of oxidation of ferritic stainless steel (FSS). It is true that metal oxidation is typically an exothermic process, as the metal-metal bonds in these cases hold more energy than the product metal-oxygen bonds. The effect of adding heat to an exothermic process can be observed in Figure 15, which displays the change in Gibbs free energy for metal oxide formation over a range of temperatures. As temperature increases, the Gibbs free energy increases, and the reaction is therefore less energetically favorable. While this effect is detrimental to oxidation, it is outweighed by kinetic considerations.

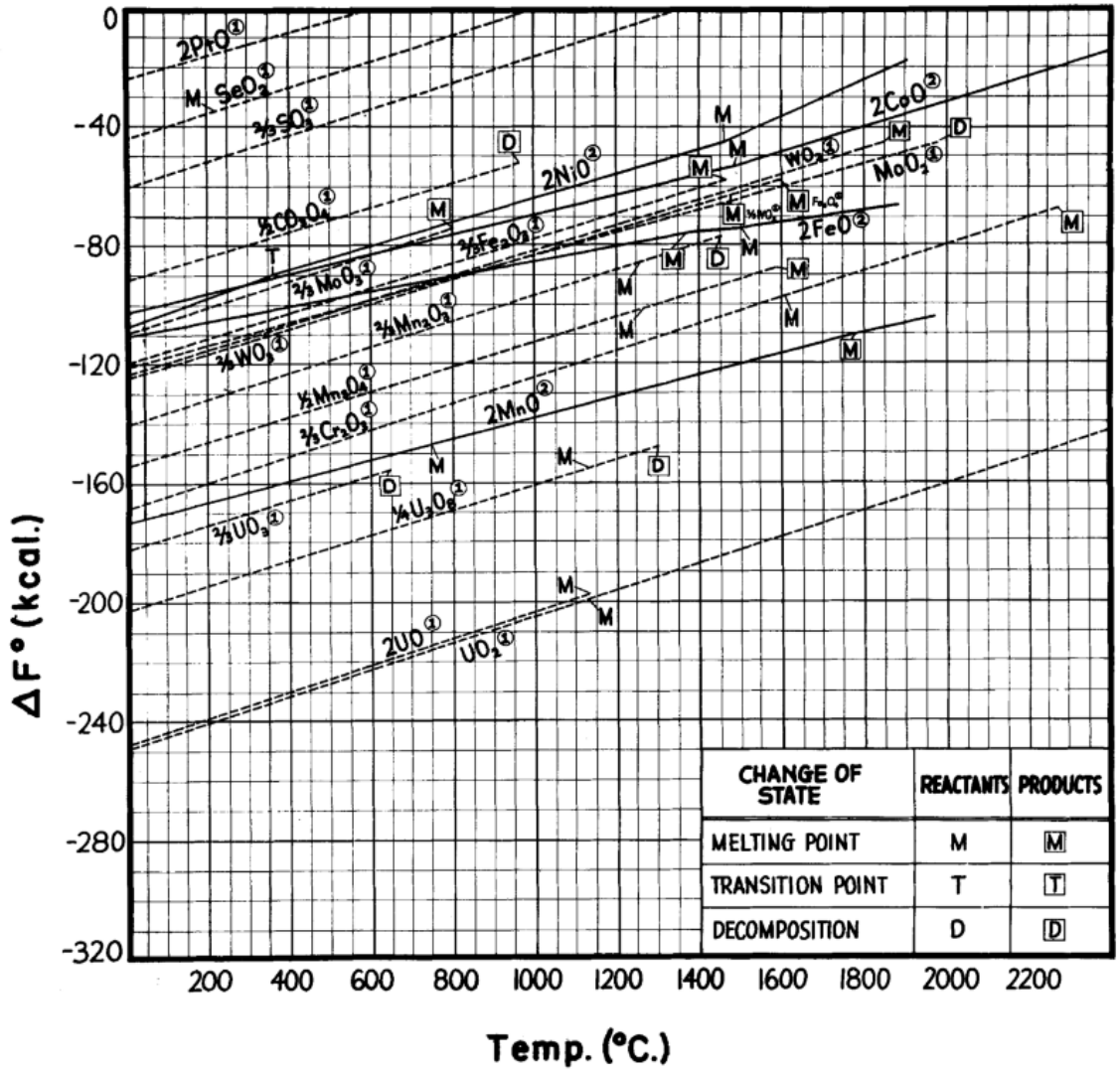


Figure 15 - Gibbs free energy of formation of metal oxides at elevated temperatures [52].

Kinetics is grounded in molecular collision theory. An increase in temperature will increase the frequency of collisions, and the energy which molecules have when colliding. Kinetic expressions, or rate laws, such as the general form shown in Equation 2.12 are often used to represent these collisions/reactions.

$$-r_A = k_A(T) \cdot fn(C_A, C_B, \ldots, C_N) \qquad (2.12)$$

$$k_A(T) = A \cdot \exp\left(-\frac{E}{RT}\right) \tag{2.13}$$

$$A = d_{AB}^2 \sqrt{\frac{8k_B T}{\mu}} \tag{2.14}$$

$$\mu = \frac{m_1 m_2}{m_1 + m_2} \tag{2.15}$$

$-r_A$ – Rate of consumption of reactant "A"

C_N – Concentration of "N"

A – Collision frequency

E – Activation energy

d_{AB}^2 – Distance between the center of "A" and "B" squared

μ – Reduced mass

The general form of the rate law in Equation 2.12 is typical of gas phase reactions, but expressions may become more complex with increasing system complexity. Active intermediates may cause deviation from elementary reaction kinetics, or kinetics in which the power of the concentration in a rate law isn't equal to its stoichiometric value in a reaction (e.g. A + B = C, C_A and C_B are raised to the first power in elementary expression $-r_A=k(T)C_AC_B$). Additional complexity arises when considering a gas/solid phase reaction as mass transport to the solid, adsorption on the surface, followed by reaction, desorption, and then transport away from the solid (if a gas phase remains) must also be considered.

When considering the kinetics of metal oxidation, factors such as diffusivity, vacancy concentration, chemical and electric potential, and temperature must be

considered. This list is not exhaustive. Figure 16 displays a simple schematic which will be used to help frame the kinetics of metal oxidation.

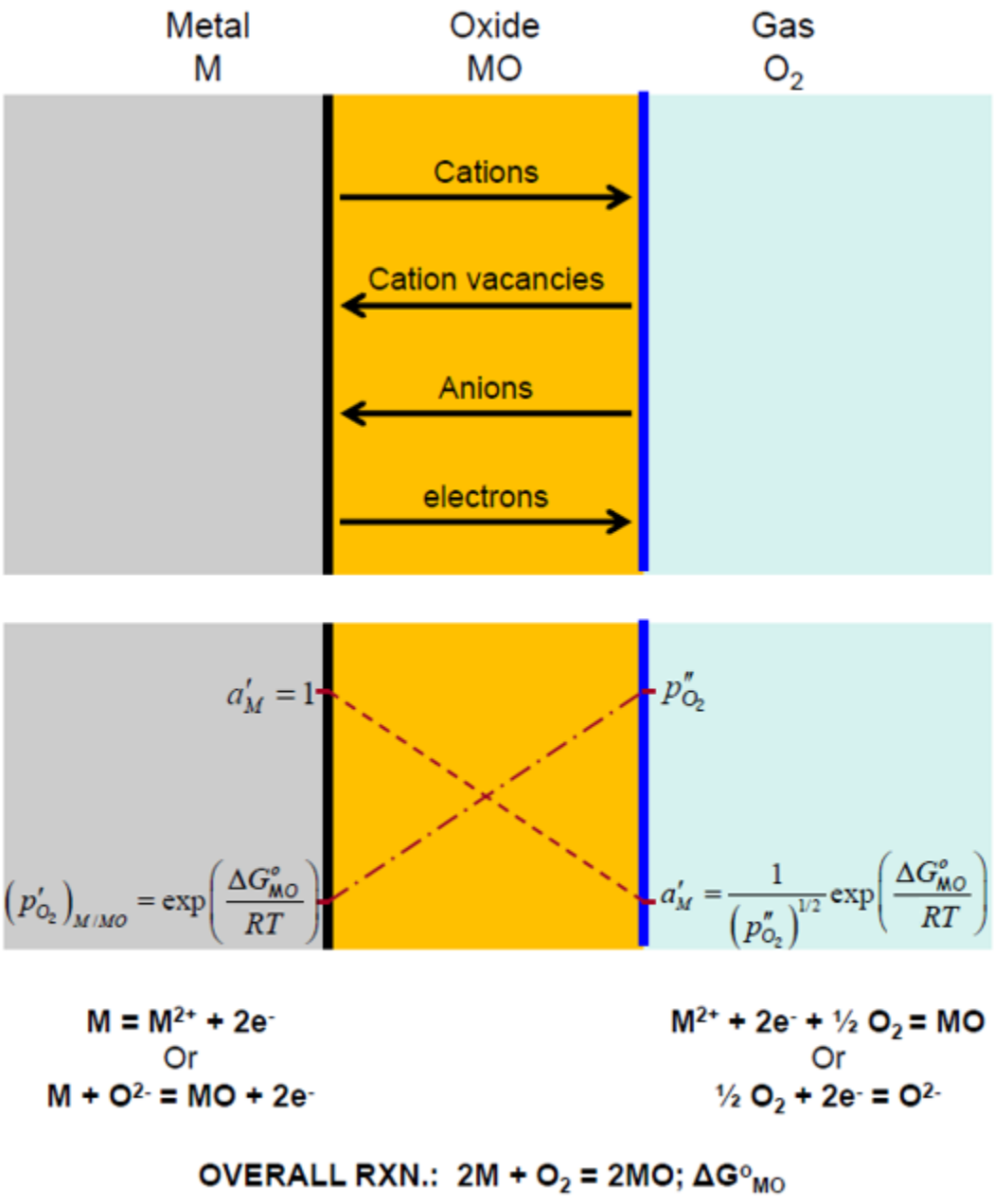


Figure 16 – Cation, anion, vacancy, and electron transport during metal oxidation. Credit: Mark Weaver University of Alabama.

Figure 16 displays diffusion of cations and electrons from the metal/oxide interface and counter diffusion of cation vacancies and anions from the oxide/gas interface. Cation and anion activity gradients are established across the oxide, also shown in Figure 16. This causes cations to diffuse outward and anions to diffuse inward, which in turn gives rise to an electric potential gradient. This gradient is alleviated by the movement of electrons through the scale, which are typically much more mobile than the cation and anion species. Metal oxide may be formed at either interface, depending on the dominant diffusing species. The parabolic rate constant is a measure of the areal growth of this oxide over time (cm^2/s). It may be expressed as Equation 2.16 in the case of greater cation mobility, or Equation 2.17 if anions are more mobile.

$$k_p = \frac{1}{RT}\int_{\mu_M''}^{\mu_M'} D_M d\mu_M \tag{2.16}$$

$$k_p = \frac{1}{RT}\int_{\mu_X'}^{\mu_X''} D_X d\mu_X \tag{2.17}$$

$$D_i = \frac{RT\kappa_i}{C_i(Z_iF)^2} \tag{2.18}$$

k_p – Parabolic rate constant

μ_M' – Chemical potential of metal “M” at metal/oxide interface

μ_M'' –Chemical potential of metal “M” at oxide/gas interface

μ_X' – Chemical potential of non-metal “X” at metal/oxide interface

μ_X'' – Chemical potential of non-metal “X” at oxide/gas interface

D_i – Diffusion coefficient for species “I” through the oxide scale

κ_i – Conductivity

C_i – Concentration of species “i”

Z_i – Charge

F – Faraday constant

Empirical methods of determining the parabolic rate constant are often more convenient, as Equations 2.16 and 2.17 require diffusion data that is not always readily available. The mass change over time may be observed to determine the parabolic rate constant at a given temperature, as can be seen in Figure 17.

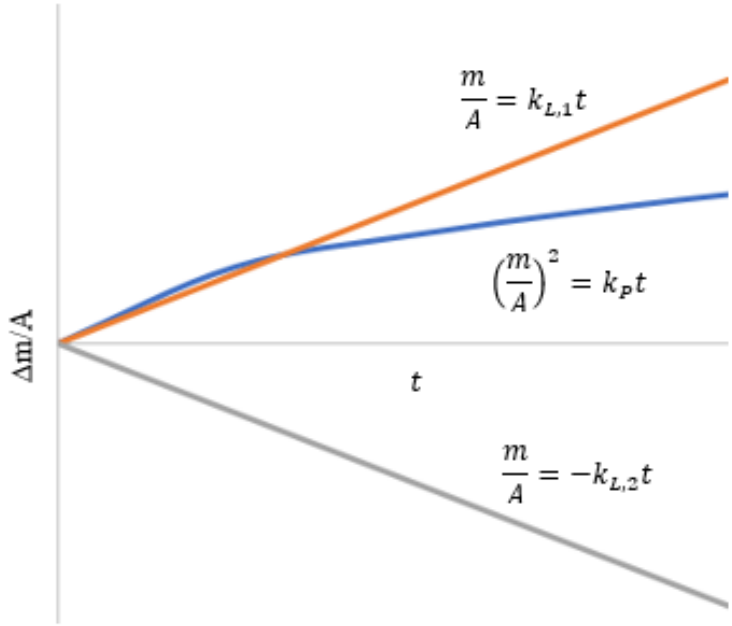


Figure 17 – oxidation kinetics: linear growth (top curve), parabolic (middle curve), and linear loss (bottom curve).

$k_{L,1}$ – Linear growth rate constant [=] g cm^{-2} s^{-1}

$k_{L,2}$ – Linear loss rate constant [=] g cm^{-2} s^{-1}

k_p – Parabolic rate constant [=] $g^2\ cm^{-4}\ s^{-1}$

As can be seen in Figure 17, which is not exhaustive, parabolic kinetics is not the only model for the rate of oxide growth. Linear rate laws, both growth and loss, are also commonly observed. Parabolic and linear regimes may be generally classified as diffusion limited and surface reaction limited, respectively. Diffusion limited oxide growth is considered protective for the underlying alloy relative to surface reaction limited, as implied in Figure 17. The mass gain of diffusion limited oxide growth will slow as the scale grows, whereas mass gain in a linear regime is not restricted in this way. With regard to parabolic kinetics, there are many assumptions required for this model to hold. The oxide layer is assumed to be dense, perfectly adherent, and only shows small deviations from stoichiometry. Thermodynamic equilibrium is assumed at the interfaces and throughout the scale. Oxygen solubility in the metal is neglected. Deviation from these ideal cases is common in real world oxide formation.

Oxygen solubility is often not negligible and may lead to internal oxidation. Oxygen ions may enter a lattice by following the sequence of events in Equation 2.19.

$$\frac{1}{2}O_{2,(g)} \rightarrow \frac{1}{2}O_{2,(a)} \rightarrow O_{(a)} \rightarrow O^{-}_{(chem)} \rightarrow O^{2-}_{(latt)} \qquad (2.19)$$

(a) – adsorbed

(chem) – Chemisorbed

(latt) – Integration into lattice

Equation 2.19 shows oxygen molecules adsorbing to a surface, splitting to form adsorbed oxygen, and electron transfer from the surface to chemisorb and integrate into the lattice. Elements with high oxygen affinity may react with oxygen in the lattice to form an

internal oxide phase. Oxygen affinity at various temperatures may be viewed using an Ellingham diagram. Using Figure 18, it may be seen, for example, that chromium has a greater affinity for oxygen than iron for the given temperature range.

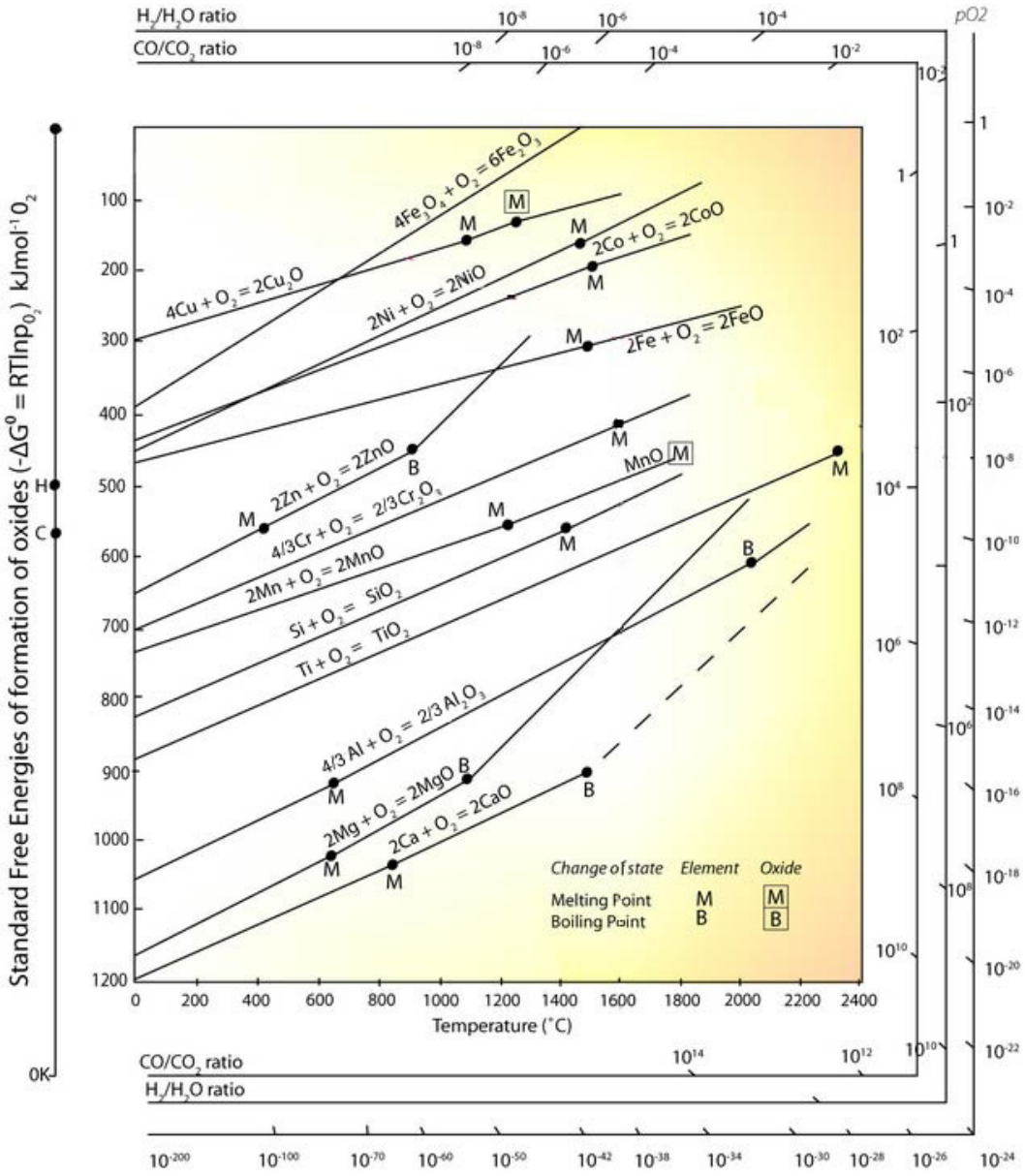


Figure 18 - Ellingham diagram. Credit: doitpoms.ac.uk.

A simplified system may be imagined consisting of generic elements “A” and “B”, where the majority of the alloy consists of A, but B has a greater affinity for oxygen. Figure 19 displays a simplistic version of internal oxidation for this binary alloy.

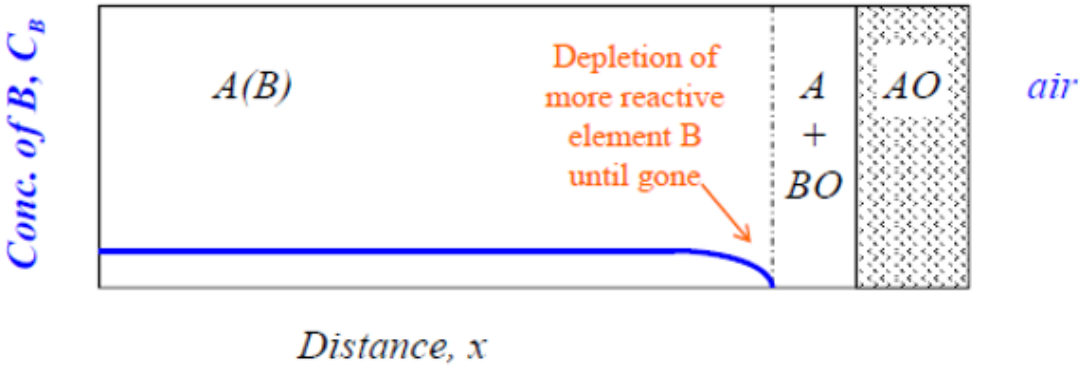


Figure 19 - Internal oxidation of binary alloy “A” and “B”, with majority A, but B having a greater oxygen affinity. Credit: Mark Weaver University of Alabama.

Figure 19 shows external scale formation of AO, and the concentration of element B in the bulk depleting as oxygen anions react with B to form the oxide “BO” internally. The formation of AO, in this case, is not protective against oxygen ingress. There exists a critical concentration of B which will result in the formation of a continuous external BO layer, as shown in Figure 20. The critical concentration is given by Equation 2.20.

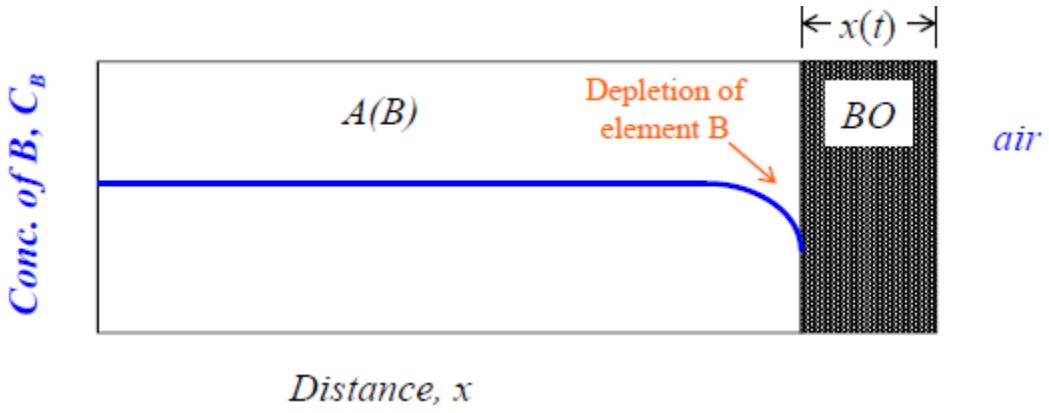


Figure 20 - Continuous scale formation of binary alloy "A" and "B" with critical concentration of B. Credit: Mark Weaver University of Alabama.

$$C_B^{crit} = \left(\frac{\pi g^* C_O^S D_O V_m}{2 D_B V_O}\right)^{1/2} \quad (2.20)$$

g^* – Critical volume fraction of oxide for transition from internal to external scale ≈ 0.3

V_m – Molar volume of metal

V_O – Molar volume of oxide

C_O^S – Solubility of oxygen in A

C_B^O – Bulk alloy concentration of B in A

D_O – Diffusivity of oxygen

It will be noted that behavior in alloys may be much more complicated, as B and A may form oxide phases together, solid solutions of B/A oxides are possible, and more elements with different diffusion rates, oxygen affinities, and phases are possible. A plausible sequence of events for FSS phase formation is as follows. At low temperature (25°C) elements in the alloy would engage in competitive adsorption of oxygen at the surface. Elements with a higher oxygen affinity will outcompete elements with a lower

oxygen affinity. Adsorbed oxygen will dissociate to molecular oxygen and chemisorb with high oxygen affinity elements. These regions serve as nucleation points of oxide compounds which may grow heteroepitaxially and coalesce into an oxide layer [53]. This surface layer is on the order of angstroms thick and forms in the order of nanoseconds [54]. As the temperature rises, the rate of diffusion of elements through the BCC lattice and oxide scale increases as can be seen in Equation 2.18 and increases the chemical potential gradients for transport of oxygen and metal through the scale. As a result, the oxidation rate constant increases and the scale thickens. Ferritic stainless steel alloys containing manganese will undergo selective oxidation of the manganese within the chromia scale as it has a greater affinity for oxygen than chromium and forms a more stable oxide. Independent phases such as MnO_x have been identified which may react with Cr_2O_3 to form an external spinel phase in the form of $MnCr_2O_4$ [25]. This duplex type scale formation of external Mn-Cr spinel and internal Cr_2O_3 is commonly observed for manganese containing FSS in oxidizing environments [11-13].

Establishment of stable external scales which are continuous, well adhered and nonporous protect the underlying alloy from oxidation. Over time, however, these layers are prone to failure. A common failure mode is spallation, or the localized fragmentation and/or detachment of a surface oxide layer. This often occurs during a temperature change due to mismatched coefficients of thermal expansion. This coefficient considers how a material changes with temperature, with linear, areal, and volumetric coefficients. These coefficients may be related to strain in a material, as Equations 2.21 and 2.22 show for linear coefficients of thermal expansion.

$$\varepsilon_{thermal}^{metal} = \alpha_M \Delta T \tag{2.21}$$

$$\varepsilon_{thermal}^{oxide} = \alpha_{Ox} \Delta T \tag{2.22}$$

$\varepsilon_{thermal}^{metal}$ – Thermal strain on metal

$\varepsilon_{thermal}^{oxide}$ – Thermal strain on oxide

α_M – Linear thermal expansion coefficient for the metal

α_{Ox} – Linear thermal expansion coefficient for the oxide

The strain of the metal and oxide is equal to the change in length divided by the original length. If the oxide remains attached, then these strains, in addition to strains caused by residual stress must equal as shown in Equation 2.23.

$$\varepsilon_{thermal}^{metal} + \varepsilon_{mechanical}^{metal} = \varepsilon_{thermal}^{oxide} + \varepsilon_{mechanical}^{oxide} \tag{2.23}$$

$$\varepsilon_{mechanical}^{metal} = \frac{\sigma_M(1-\nu_M)}{E_M} \tag{2.24}$$

$$\varepsilon_{mechanical}^{oxide} = \frac{\sigma_{Ox}(1-\nu_{Ox})}{E_{Ox}} \tag{2.25}$$

$\varepsilon_{mechanical}^{metal}$ – Mechanical strain from residual stress in metal

$\varepsilon_{mechanical}^{oxide}$ – Mechanical strain from residual stress in oxide

ν_M – Poisson's ratio for the metal

ν_{Ox} – Poisson's ratio for the oxide

E_M – Young's modulus for the metal

E_{Ox} – Young's modulus for the oxide

The mechanical stress Equations (2.24 and 2.25) are an extension of Hooke's law, which states that force is equal to displacement of a spring multiplied by a stiffness

constant. Atoms bonded behave in a similar way so long as the force does not begin causing plastic deformation, where stress acts as a force per area, Young's modulus as a stiffness constant for bond stretching (also F/A), and the strain as displacement. Poisson's ratio is the change in transverse length over the change in longitudinal length, and is used in Equations 2.24 and 2.25 to account for stress in the direction of longitudinal strain. Combining Equations 2.21-2.25, and a force balance (Equation 2.26), yields Equation 2.27, which is the thermally generated stress on the oxide.

$$\sigma_M t_M + 2\sigma_{Ox} t_{Ox} = 0 \tag{2.26}$$

$$\sigma_{Ox} = -\frac{(\alpha_{Ox}-\alpha_M)\Delta T}{\frac{2t_{Ox}(1-\nu_M)}{t_M E_M}+\frac{(1-\nu_{Ox})}{E_{Ox}}} \tag{2.27}$$

σ_M – Metal stress

σ_{Ox} – Oxide stress

t_M – Metal thickness

t_{Ox} – Oxide thickness

If the Poisson ratios for the oxide and metal are the same, and if the scale is thin relative to the metal thickness, then Equation 2.27 may be simplified to Equation 2.28.

$$\sigma_{Ox} = -\frac{E_{Ox}\Delta\alpha\Delta T}{(1-\nu)} \tag{2.28}$$

There exists some threshold change in temperature which will generate a critical stress and result in spallation. This critical stress is related to a critical strain by Young's modulus, which is related to critical strain energy per unit volume as seen in Equation 2.29. Strain energy is a measure of the energy stored in a material under strain. The

critical strain energy is the most energy a strained oxide may withstand before detaching from the metal/oxide interface.

$$W^* = \frac{1}{2}\sigma_x\varepsilon_x + \frac{1}{2}\sigma_y\varepsilon_y = \frac{\sigma_{Ox}^2}{E_{Ox}}(1 - \upsilon_{Ox}) \quad (2.29)$$

W* – Critical strain energy per unit volume

σ_x – Stress in the x-direction

σ_y – Stress in the y-direction

ε_x – Strain in the x-direction

ε_y – Strain in the y-direction

Equation 2.29 is valid given an assumption of equibiaxial stress and strain. Unidirectional thermal stress may be entered into Equation 2.29 (Equation 2.28 without the denominator) to give Equation 2.30.

$$W^* = E_{Ox}(1 - \upsilon_{Ox})\Delta\alpha^2\Delta T_c^2 \quad (2.30)$$

ΔT_c – Critical temperature change

The critical strain energy is related to the energy of the oxide/metal interface and the resultant surface energies of both metal and oxide, shown in Equation 2.31. These surface energies are a measure of stability, with small values being more stable than large values. As can be seen in Equation 2.31, the more stable the interface (low interfacial energy) and the less stable the oxide/metal surfaces (high surface energies), the more the critical strain energy required for spallation increases.

$$\xi W^* = \gamma_o + \gamma_m - \gamma_{om} \quad (2.31)$$

γ_o – Surface energy of oxide

γ_m – Surface energy of metal

γ_{om} – Energy of oxide/metal interface

ξ – Oxide thickness

Equations 2.30 and 2.31 may be combined to give Equation 2.32, an expression relating the critical temperature change to the interfacial and surface energies.

$$\Delta T_c = \left(\frac{\gamma_o+\gamma_m-\gamma_{om}}{\xi E_{Ox}\Delta\alpha^2(1-\nu_{Ox})}\right)^{1/2} \quad (2.32)$$

It is important to note that these equations assume entirely elastic fracture behavior. Plastic deformation or creep could also serve to dissipate strain energy.

Growth stress is another considerable source of stress that must be considered. As an oxide scale grows, growth stresses build due to differences in molar volume between the oxide scale and the metal. This volume mismatch is often described using the Pilling-Bedworth ratio (PBR) shown in Equation 2.33.

$$PBR = \frac{V_{Ox}}{V_M} \quad (2.33)$$

V_{Ox} – Molar volume of the oxide

V_M – Molar volume of the metal

If the PBR is greater than one, then the oxide is expected to experience compressive stress. Compressive stresses are only generated, however, if the oxide grows from the oxide/metal interface or within the oxide. These regions are constrained and will therefore introduce stress, whereas growth at the gas/oxide interface is unconstrained and will not introduce stress. Oxides that grow predominately by outward diffusion will therefore incur less growth stress than oxides which grow by inward or mixed diffusion.

Growth stresses for the latter cases are best modeled by mixed diffusion, as oxygen may gain access to the interior of oxides through micro-cracks or grain boundaries. Equation 2.34 may be used to approximate growth stresses due to oxide growth within grain boundaries, provided the grain size is much thinner than the scale thickness.

$$\sigma_{Ox} = \frac{4G_{Ox}d_i}{2\delta(1-2\nu_{Ox})} \tag{2.34}$$

G_{Ox} – Shear modulus

d_i – Width of new oxide grown at internal grain boundaries

δ – Oxide grain size

Shear modulus is similar to Young's modulus, but uses shear stress and strain instead of normal stress and strain. Similar to the examination of thermal stress, Equation 2.34 is grounded in an assumption of elastic oxide behavior.

Compressive stresses generated from growth stresses and/or thermal stresses, if in excess of the critical strain energy, may result in spallation in the form of wedging or buckling. Wedging occurs if the adhesive strength of the interface is greater than the cohesive strength of the oxide. Buckling occurs if the opposite is true. Figure 21 displays these two spallation behaviors given a temperature drop.

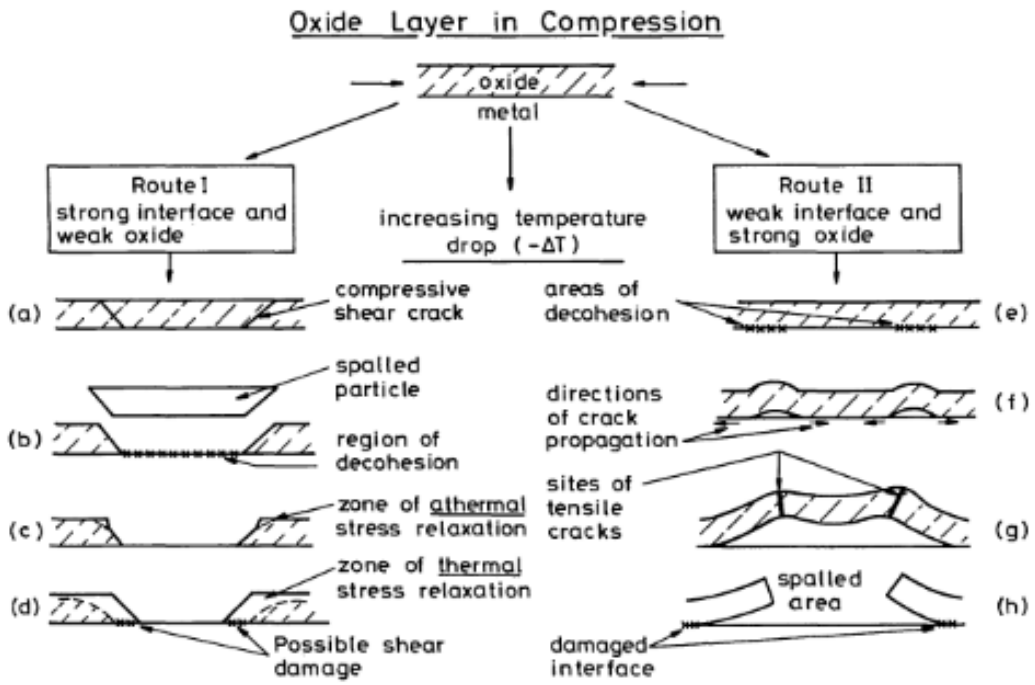


Figure 21 - Wedging and buckling, from Evans et al. [55].

A localized breakdown of protective behavior occurs in the event of spallation by wedging or buckling. If chromium is above the requisite critical concentration (Equation 2.20) then the spalled region may quickly reform an external protective oxide scale. There exist conditions which may compromise this self-healing behavior. If the creep rate in the metal core is sufficiently high, then the oxide may experience tensile stress in excess of the oxide fracture strength, resulting in tensile cracking. The rate of scale reformation would need to be greater than the imposed strain rate in order to fill the crack with protective oxide. Volatility due to water vapor, as will be discussed in the next section, is another such compromising condition.

Influence of Water Vapor

While reactive evaporation of chromium from chromia is observed to occur more extensively in atmospheres of oxygen and water vapor (see Figure 6), it is important to note that there will always be some partial pressure of compound "x" in the vapor phase, regardless of the atmosphere. Often this partial pressure is negligible for practical considerations. For example, using thermodynamic data from Ebbinghaus [56], the equilibrium partial pressure of $CrO_3(g)$ in Equation 1.1 (formed from chromia and oxygen) may be estimated to be 8E-40 bar at 298 K and 0.21 bar oxygen. As was seen in the thermodynamic section, an increase of 500 K increases this partial pressure by 25 orders of magnitude, up to 1E-15 bar. The oxyhydroxide ($CrO_2(OH)_2(g)$) partial pressure was observed to be larger (in the presence of water vapor), by many orders of magnitude for much of the temperature range up until approximately 1400 K. The importance of temperature and reactants on the reactive evaporation of chromium have been noted, but the importance of mass transport has not yet been discussed. Fluid dynamics play a large role in the evaporation rates of chromium from scales, and limiting thicknesses for those scales as will be discussed.

In a closed system with chromia, water vapor, and oxygen, the equilibrium partial pressure of $CrO_2(OH)_2$ at temperature T would eventually be reached and sustained, causing little disturbance to an oxide scale. In real world applications, however, oxygen and water vapor will be flowing past chromium oxide scales at some gas velocity "u". This gas velocity will influence the thickness of the boundary layer, which is a region close to a surface in which viscous forces dominate, as seen in Figure 22.

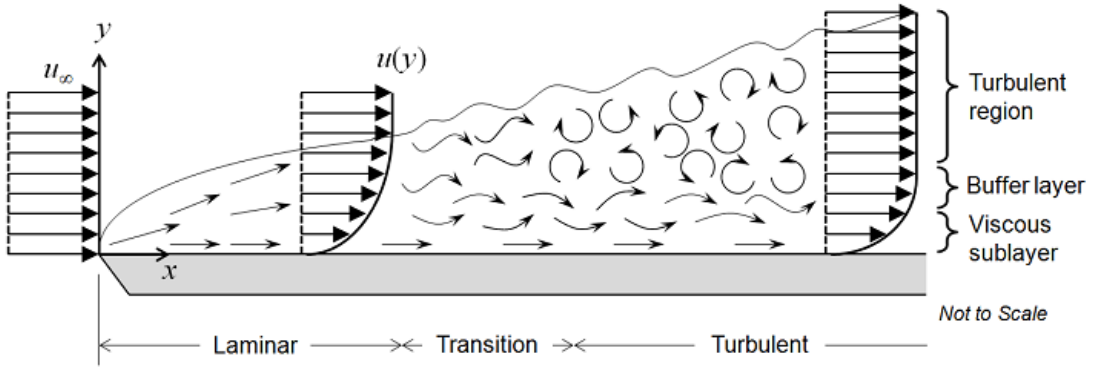


Figure 22 - Boundary layer illustration. Credit: comsol.com.

There are three regions on the flat plate geometry shown in Figure 22: laminar, transition, and turbulent. The laminar region is dominated by viscous forces. The transition region follows where inertial forces begin to become non-negligible. The turbulent region is comprised of an outer turbulent layer where inertial forces dominate, a thin viscous sublayer close to the surface, and a buffer layer between which acts as an intermediary between the two. The free stream gas velocity is altered upon entering the boundary layer, depending position "x" down the plate of length "L", and position "y" in the boundary layer. The boundary layer thickness grows down the length of the plate. This is due to the dependence of the boundary layer on the Reynolds number. The Reynolds number is a dimensionless quantity which represents the ratio of inertial forces to viscous forces, as seen in Equation 2.35.

$$Re = \frac{\rho u x}{\mu} \tag{2.35}$$

Re – Reynolds number

ρ – Density

u – Gas velocity

x – Length down the flat plate

μ – Dynamic viscosity

The dependence of the boundary layer thickness on the Reynolds number may be seen from an order of magnitude analysis on the equation of motion in the x-direction for a Newtonian fluid in Equations 2.36-2.40.

$$\rho\left(\frac{\partial v_x}{\partial t}+v_x\frac{\partial v_x}{\partial x}+v_y\frac{\partial v_x}{\partial y}+v_z\frac{\partial v_x}{\partial z}\right)=-\frac{\partial P}{\partial x}+\mu\left(\frac{\partial^2 v_x}{\partial x^2}+\frac{\partial^2 v_x}{\partial y^2}+\frac{\partial^2 v_x}{\partial z^2}\right) \tag{2.36}$$

$$\rho v_x\frac{\partial v_x}{\partial x}\sim O\left(\rho\frac{u^2}{L}\right) \tag{2.37}$$

$$\mu\frac{\partial^2 v_x}{\partial x^2}\sim O\left(\mu\frac{u}{\delta^2}\right) \tag{2.38}$$

$$\rho\frac{u^2}{L}\sim\mu\frac{u}{\delta^2} \tag{2.39}$$

$$\delta\sim\frac{L}{\sqrt{Re}} \tag{2.40}$$

The boundary layer thickness is directly proportional to the length of the plate and inversely related to the square of the Reynolds number. This is valid for viscous and inertial forces which are approximately equal, but as the inertial forces become more dominant (Re>>1) the boundary layer thickness deviates from this model. For turbulent flow the law of the wall is a better approximation. This approximation may be briefly described by examining the shear stress generated due to flow in the x direction, with momentum transfer in the y direction shown in Equation 2.41.

$$\tau_{yx} = \mu \frac{d\bar{v}_x}{dy} - \rho \bar{v}_x' \bar{v}_y' \tag{2.41}$$

τ_{yx} – Shear stress with flow in direction x and momentum transfer in direction y

μ – Absolute viscosity

ρ – Density

$\bar{v}_x$ – Time averaged velocity in the x-direction

$\bar{v}_x'$ – Time averaged velocity fluctuations in the x-direction

$\bar{v}_y'$ – Time averaged velocity fluctuations in the y-direction

Velocity fluctuations in a given direction are expected to be largely random, so averaging these quantities alone gives zero. The velocity fluctuations in the x and y directions are correlated, however, so their averaged product is not equal to zero. This product is instead known as the Reynolds stress. This stress is not expected to make a large contribution in the laminar region, or viscous sublayer in the turbulent region in Figure 22. These regions are best described by Newton's law of viscosity (Equation 2.41 without the Reynolds stress). The turbulent layer of the turbulent region in Figure 22 is better described by the Reynolds stress, which may be transformed into the non-dimensional logarithmic law of the wall as follows.

$$\bar{v}_y' \cong \bar{v}_x' = \kappa y \frac{d\bar{v}_x}{dy} \tag{2.42}$$

$$\tau_{yx,turbulent} = \rho \kappa^2 y^2 \left(\frac{d\bar{v}_x}{dy}\right)^2 = \tau_o \; at \; the \; wall \tag{2.43}$$

$$\frac{d\bar{v}_x}{dy} = \frac{\sqrt{\tau_o / \rho}}{\kappa y} \tag{2.44}$$

$$\bar{v}_x = \frac{\sqrt{\tau_o/\rho}}{\kappa} \cdot lny + C_1 \tag{2.45}$$

$$v^* = \frac{\bar{v}_x}{\sqrt{\tau_o/\rho}} \tag{2.46}$$

$$y^* = y \cdot \frac{\sqrt{\tau_o/\rho}}{\nu} \tag{2.47}$$

$$v^* = \frac{1}{\kappa} \cdot lny^* + C_1' \tag{2.48}$$

v^* - Non-dimensional velocity

y^* - Dimensionless length

κ – Empirical constant

C_1 – Integration constant

C_1' - Modified integration constant

The empirical constant κ is related to mixing length ($\kappa \cdot y$) which is the distance over which a fluid control volume will retain its characteristics before mixing with the surrounding fluid. This constant and the integration constant C_1' have been determined empirically and used to construct the universal velocity profile displayed in Figure 23.

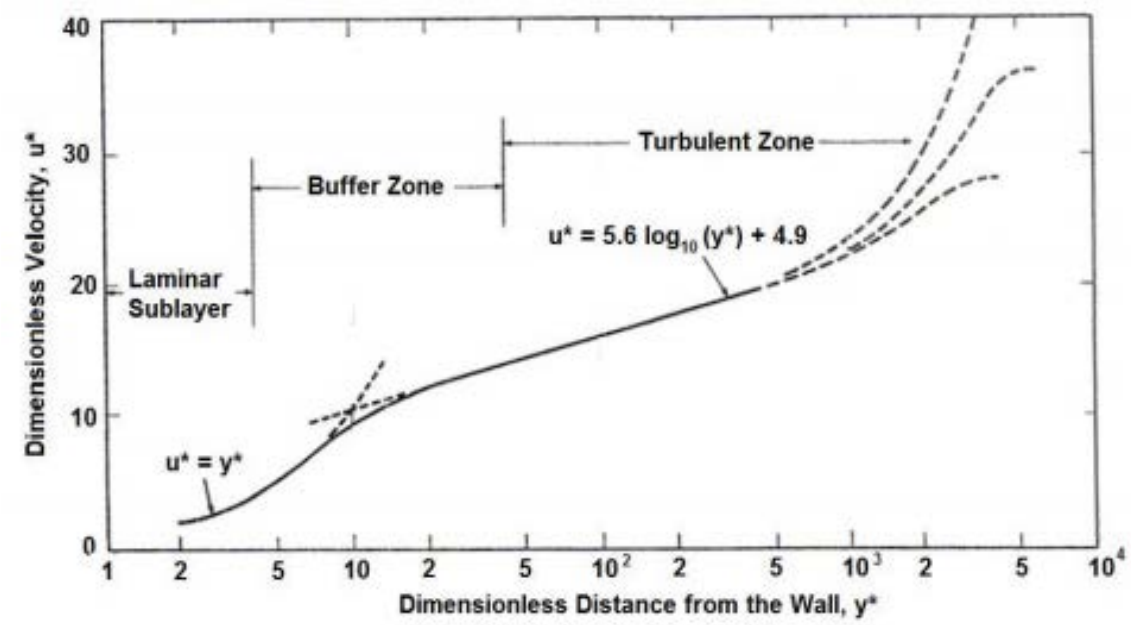


Figure 23 - Universal velocity profile near a wall. Credit: Brennen.caltech.edu.

Fluid may only be modeled by Newton's law of viscosity up to a dimensionless length of about 5. Equation 2.48, shown with $\kappa = 1/5.6$ and C_1' = 4.9, is valid above a dimensionless length of 30. Between these zones exists the buffer region, and a suggested fit takes a similar form to Equation 2.48 as v*=5 ln(y*+0.205)-3.27.

The Reynolds number is also related to the linear volatility rate, mentioned previously in linear oxidation kinetics. For FSS, where mass gain and loss is occurring simultaneously in high temperature air and water vapor, parabolic and linear kinetics need to be combined to describe the behavior. The Tedmon equation (Equation 2.49) is used to combine parabolic rate mass gain and linear mass loss.

$$\frac{dx}{dt} = \frac{k_p}{x} - k_l \tag{2.49}$$

x – scale position

k_p – Parabolic rate constant

k_l – Linear rate constant

The linear rate constant may be approximated using the Sherwood number, which is a function of the Reynolds number and the Schmidt number. The Reynolds number was conceptualized as the ratio of inertial forces to viscous forces. Similarly, the Schmidt number may be conceptualized as the ratio of the rate of viscous diffusion to the rate of mass diffusion. The Sherwood number combines these concepts to give the ratio of the convective mass transfer rate to the rate of diffusion. It is related to the linear rate constant as shown in Equation 2.50.

$$Sh = \frac{k_l L}{\rho D} \tag{2.50}$$

Sh – Sherwood number

L – Characteristic length

D – Diffusion coefficient

The Sherwood number as defined in Equation 2.50 may be equated to correlations developed given conditions such as geometry and Reynolds number. For flat plate geometry and a Reynolds number less than 3 x 10^5, Equation 2.51 is used to approximate the Sherwood number.

$$Sh = 0.644 Re^{0.5} Sc^{0.33} \tag{2.51}$$

Sc – Schmidt number

Combining Equations 2.50 and 2.51 yields Equation 2.52 which is an approximation for the linear rate constant given flat plate geometry and laminar flow conditions.

$$k_l = 0.644 Re^{0.5} Sc^{0.33} \cdot \frac{\rho D}{L} \tag{2.52}$$

Using the ideal gas law to substitute in partial pressure of volatile chromium species for density gives Equation 2.53.

$$k_l = 0.644 Re^{0.5} Sc^{0.33} \cdot \frac{DM_{CrO2(OH)2}}{LRT} \cdot P_{CrO2(OH)2} \tag{2.53}$$

The partial pressure of chromium oxyhydroxide may be replaced using the Gibbs free energy expression for Equation 1.2.

$$\Delta G_{eq\,2} = -RTln\left(\frac{P_{CrO2(OH)2}}{P_{H2O} P_{O2}^{0.75} a_{Cr2O3}^{0.5}}\right) \tag{2.54}$$

$$k_l = 0.644 Re^{0.5} Sc^{0.33} \cdot \frac{DM_{CrO2(OH)2}}{LRT} \cdot \exp\left(-\frac{\Delta G_{eq\,2}}{RT}\right) P_{H2O} P_{O2}^{0.75} a_{Cr2O3}^{0.5} \tag{2.55}$$

For a flat plate geometry with a Reynolds number above 3 x 10^5, the Reynolds number in Equation 2.55 will be 0.8 instead of 0.5. As they Reynolds number increases, so too does the linear rate constant. Examining the Tedmon equation (Equation 2.49), a limiting scale thickness may be approximated when the derivative is equal to zero. This thickness is equal to k_p/k_l, so an increasing linear rate constant decreases the oxide thickness limit. There exists some disagreement in literature as to a limitation on the linear rate constant. Kurokawa et al. [34] and Gindorf et al. [33] have both suggested an upper limit to this rate constant, as can be seen in Figure 24. These figures do not have the same units as k_l, but are related by the proposed limitation on mass transport of chromium, even as the flow rate continues to increase. In both cases, volatile chromium condensate was collected on glass tubes, which was then dissolved into a nitric acid solution and quantified using inductively coupled plasma mass spectroscopy.

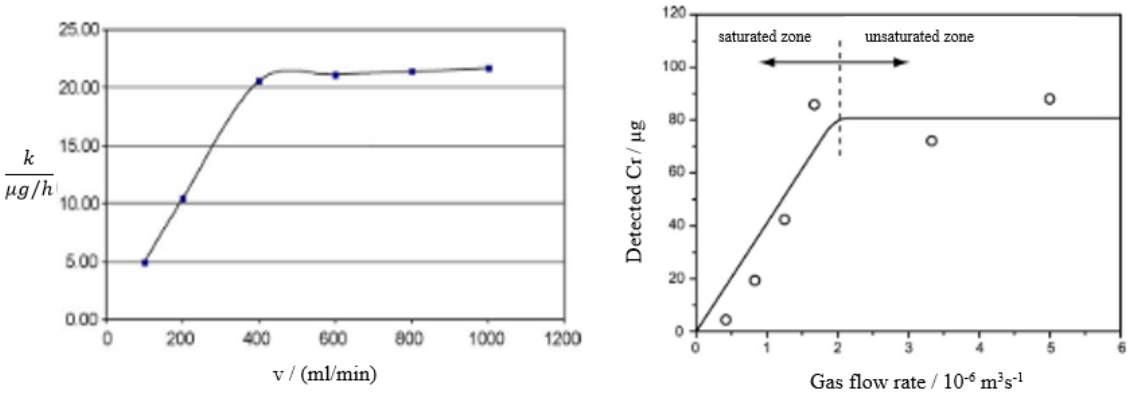


Figure 24 – Collected volatile chromium vs gas flow rate: Gindorf et al. [33] left, Kurokawa et al. [34] right.

The universality of these results were called into question by a study performed by Holcomb [36]. Holcomb examined supercritical steam turbine conditions with a linear flow rate of 300 m/s, temperatures ranging from 540-760°C, pressures ranging from 163-340 atm, and 1-21.70 ppb dissolved oxygen. Predicted mass transport coefficients for steam turbines are displayed against laboratory conditions (linear velocity of 0.02 m/s) at 760°C in Figure 25.

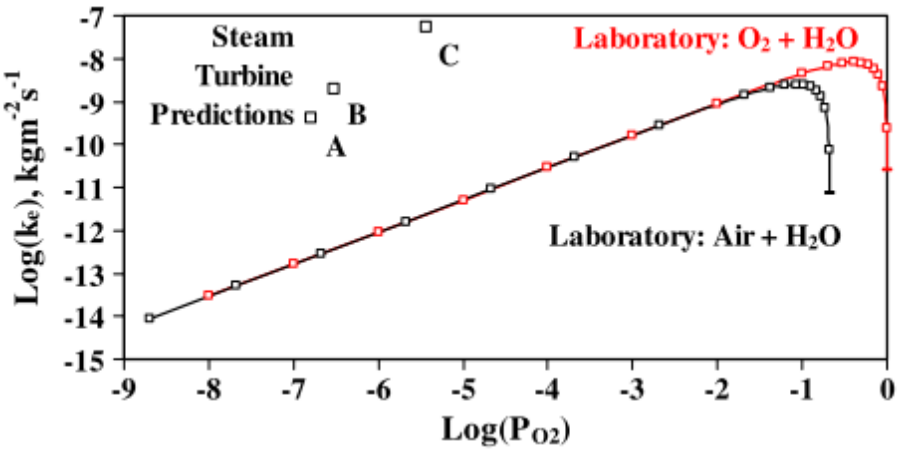


Figure 25 - Mass transport coefficients for steam turbines and laboratory conditions. "A" is representative of current power plant conditions, "B" is for current advanced power plants, and "C" is for DOE target conditions.

The mass transport coefficients for steam turbines are predicted to be several orders of magnitude higher than laboratory scale conditions. While the high gas velocity certainly contributes to increasing the mass transport coefficient, it is unclear how much of the difference is attributable solely to the gas velocity. There is also a two order of magnitude pressure difference between the lab scale and turbine conditions. This pressure increase will increase the reactive evaporation of chromium, as thermodynamic modeling shows in Figure 26.

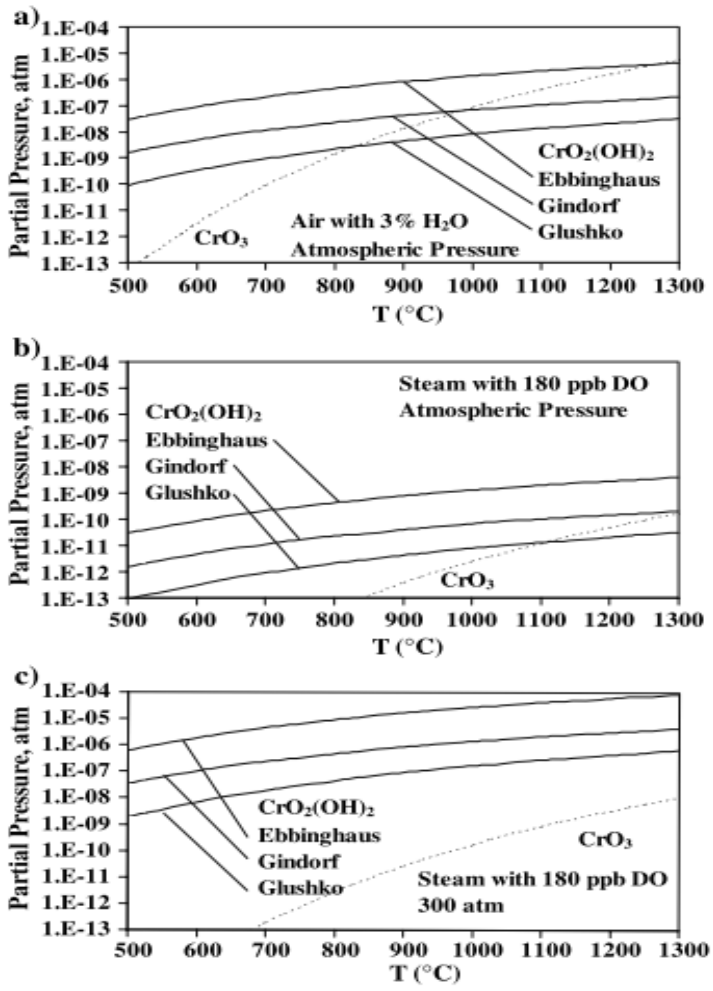


Figure 26 - Thermodynamic modeling using data from Ebbinghaus, Gindorf, and Glushko. a) air and 3% water vapor at 1 atm, b) steam with 180 ppb dissolved oxygen at 1 atm, c) steam with 180 ppb dissolved oxygen at 300 atm.

The difference in oxygen content is an additional confound when attempting to directly compare laboratory scale and turbine conditions. Holcomb suggests future work to include increased gas velocity experiments. The Opila research group at the University of Virginia has developed a steam jet technique in which liquid water is delivered into the hot zone of a furnace via a fused quartz capillary. The water evaporates and the subsequent expansion allows for a jet of high temperature steam with a gas velocity of

150-200 m/s [57]. To the knowledge of the author this technique has not been used to examine chromium volatility.

Up to this point the reactive evaporation of chromium has been examined from a pure chromia source, but in FSS this will rarely be the case. The general case for oxide phase formation was given in the previous section, where an external scale of Mn-Cr spinel may be expected to form. This oxide is more stable than chromia and is therefore less susceptible to reactive evaporation of chromium [18, 58, 59]. Volatility differences of various oxides will be outlined in the following section. The impact of chromium volatilization on FSS oxide phase formation will be explored here.

One may begin with FSS behavior in “low evaporation rate” environments. These are described by Segerdahl et al. [60] as gas environments which promote the reactive evaporation of chromium, but the oxide remains protective. In this study, these atmospheres consisted of O_2 + 10% H_2O and O_2 + 40% H_2O with gas velocities less than 2.5 cm/s. Under these conditions, the alloy which formed a protective Cr-rich $(Cr,Fe)_2O_3$ layer in dry O_2 instead forms an Fe-rich $(Cr,Fe)_2O_3$ outer layer with a Cr-rich $(Cr,Fe)_2O_3$ inner portion. Increasing the flow rate above 2.5 cm/s, creating a “high evaporation rate” environment, results in a breakdown of protective behavior. The corundum type solid solution breaks down into an outer layer of nearly pure hematite with Fe,Cr spinel underneath. The breakdown in protective behavior resulted in a mass change (mg/cm^2) two orders of magnitude higher (O(0.01) up to O(1)). It may be noted that while the Mn,Cr spinel phase was not claimed, depth profiling revealed a thin (<0.1 μm) layer of manganese which appeared to covary with chromium content. Similar breakdown in

protective behavior was noted by Asteman et al. [61] for oxidation of 304L in similar gas environments, though the change in mass was only one order of magnitude, and an inner layer of Fe-rich $(Cr,Fe)_2O_3$ was noted as opposed to Fe,Cr spinel.

Breakdown of protective behavior in these studies was not uniform, but instead led to localized regions of breakaway corrosion. These breakaway regions, comprised of an outer layer of hematite, grow much more quickly than the surrounding protective scale and lead to the creation of what are termed “oxide islands”. An observation was made by Asteman et al. [61] that oxide islands often do not cross grain boundaries, but instead form within these borders. It was proposed that grain boundaries, which permit diffusion rates up to nine orders of magnitude greater than the bulk [62], were not depleted of chromium even under high evaporation rate conditions. This would allow grain boundaries to remain protective, while regions away from these boundaries would become depleted of chromium as described above and subsequently form oxide islands.

Formation of oxide islands is not restricted to conditions promoting volatilization induced localized breakaway corrosion. Several authors have also noted oxide island formations under conditions in which chromium volatility is negligible. Essuman et al. [63] exposed Fe-10Cr and Fe-20Cr to atmospheres of Ar-20% O_2, Ar-7% H_2O, and Ar-4% H_2-7% H_2O at 900°C for 72 hours. In accordance with Figures 19 and 20, the 10Cr alloy exposed to Ar-20% O_2 formed an external layer of iron oxides and in inner layer of chromia, whereas the 20Cr alloy formed a protective external chromia scale. In Ar-4% H_2-7% H_2O, both alloys experienced internal oxidation, though the 10Cr alloy had more extensive internal oxidation due to its inability to form a protective external chromia

layer. Both alloys, however, experienced a breakdown in protective behavior in Ar-7% H_2O. Oxide islands like those described by Asteman et al and Segerdahl et al. [60, 61], with more extensive oxide growth present in the 10Cr alloy.

Ehlers et al. [64] made similar observations with 9%Cr steel P91 at 650°C in N_2-1% O_2- x% H_2O (x=2-7) for 1-30 hours. In N_2-1% O_2 the alloy formed a thin protective scale. Adding water to the gas led to breakaway corrosion with an outer most layer of hematite, with underlying layers of magnetite, Fe-Cr-Mn spinel, and lastly an internal oxidation zone. As the water composition in the gas increased, the time necessary to induce breakaway corrosion was reduced. These breakaway regions were noted to be porous and contain many voids which also increased with increased water content. The study's authors attributed the porosity and voids to the formation of iron hydroxide within the scale from reactions between iron oxide and water vapor in anoxic conditions. Iron hydroxide formed in the scale may diffuse to the surface where the oxygen partial pressure is large enough to convert the iron hydroxide into an iron oxide. An important condition for breakaway oxidation was given as $pH_2O/pO_2 \geq 1$ at which point water is expected to outcompete oxygen in adsorbing to vacant surface sites.

Influence of Ceramic Contacting Conditions

The author performed a similar study of FSS in mixed gas environments, but also incorporated contacting aluminosilicate fibers to examine their impact on corrosion behavior. Many prior studies have examined the effect of contacting conditions on corrosion behavior. Several coatings, such as reactive element oxide (REO), perovskite, and spinel have been examined in the SOFC literature. These coatings are intended to

attenuate oxide scale thickness, be electronically conductive, reduce reactive evaporation of chromium, and generally meet SOFC component requirements as outlined in Chapter Three.

Reactive element oxides incorporate reactive elements such as Y or Ce which are believed to segregate to grain boundaries and block/slow short-circuit diffusion [65]. These elements are also theorized to serve as closely spaced surface nucleation points, which result in a thin, fine-grained scale forming more rapidly than uncoated oxidation [66]. Several authors have studied these coatings for FSS SOFC interconnects. Qu et al. [66] examined the effect of Y, Co, and Y/Co oxide coatings on 430 SS at temperatures ranging from 700 to 800°C in air for up to 500 hours. All samples, coated and uncoated, formed chromia and Cr-Mn spinel. Uncoated and Co coatings displayed the worst oxidation resistance and were susceptible to spallation after 250+ hours. Yttria coatings resulted in scale thickness and mass gains 50% less than uncoated and Co coatings and 25% of the area specific resistance (ASR) with 14-21 $m\Omega\ cm^2$. Coatings of Y/Co had similar ASR values.

Fontana et al. [23] examined the effect of coating Crofer 22 APU, AL 453, and Haynes 230 with La_2O_3, Nd_2O_3, and Y_2O_3 after 100 hours in 800°C air. The Ni based alloy Haynes 230 showed the best oxidation resistance, but does not have a suitable CTE for current use in a SOFC system. All coatings for the two ferritic stainless steels reduced the observed parabolic rate constants, but some coatings increased the ASR relative to the uncoated samples. Crofer 22 APU coated with Y_2O_3 had an ASR 2-3 times higher than uncoated Crofer, whereas La_2O_3 coated Crofer was two orders of magnitude lower at

0.004 Ω cm^2 after 100 hours. The La_2O_3 coating was observed to form a $LaCrO_3$ perovskite phase, likely doped with iron, which endowed it with a high conductivity. Coatings on AL 453 were not observed to be largely beneficial in terms of ASR, with Y_2O_3 performing slightly better at 0.069 Ω cm^2 as opposed to 0.077 Ω cm^2 for uncoated, La_2O_3 being 0.219 Ω cm^2, and Nd_2O_3 at 0.524 Ω cm^2. The formation of the $YCrO_3$ perovskite phase on AL 453, but not on Crofer, helps to explain the poor performance of Y_2O_3 on Crofer, with the Y_2O_3 resistivity being higher than chromia or the perovskite [23].

The formation of perovskites from reactive element oxides has been repeatedly observed [23, 67, 68]. Cubic structured with the general formula ABO_3, where "A" is typically a rare earth metal (La, Y, etc.) and "B" a transition metal (Cr, Mn, etc.), perovskites offer excellent electric conductivity and stability in over a wide pO_2 range [69]. They may also supply reactive elements to the underlying oxide scale to enhance oxidation resistance as mentioned above. Dopants such as strontium and calcium, which occupy the lanthanum site, are commonly used and increase the conductivity [70, 71]. These properties make perovskite coatings promising for SOFC interconnects, but there are challenges to be addressed. Yang et al. [72] coated E-brite, Crofer 22 APU, and AL 453 with $LaSr_{0.2}FeO_3$ (LSF) and $LaSr_{0.2}CrO_3$ (LSC) and exposed them to 800°C air for 1200 hours. All coatings were observed to improve oxidation resistance over uncoated alloys, and only LSC coated Crofer 22 APU was observed to be detrimental to the ASR. Coatings of LSC were better for oxidation resistance than LSF due to its lower ionic conductivity, but chromium volatility from LSC is still a concern. Though LSF does not

contain chromium, it does not prevent outward diffusion of chromium from the steel into the coating which may then volatilize. Peck et al. used Knudsen effusion mass spectroscopy to determine the vapor pressure of volatile chromium species over LSC and lanthanum chromite. Knudsen effusion mass spectroscopy is a technique in which a material is placed in a Knudsen cell where volatile species diffuse into a low pressure region where they are subsequently ionized and analyzed using mass spectroscopy. Partial pressures of volatile species were calculated to be several orders of magnitude lower in LSC and lanthanum chromite when compared to chromia as seen in Figure 27.

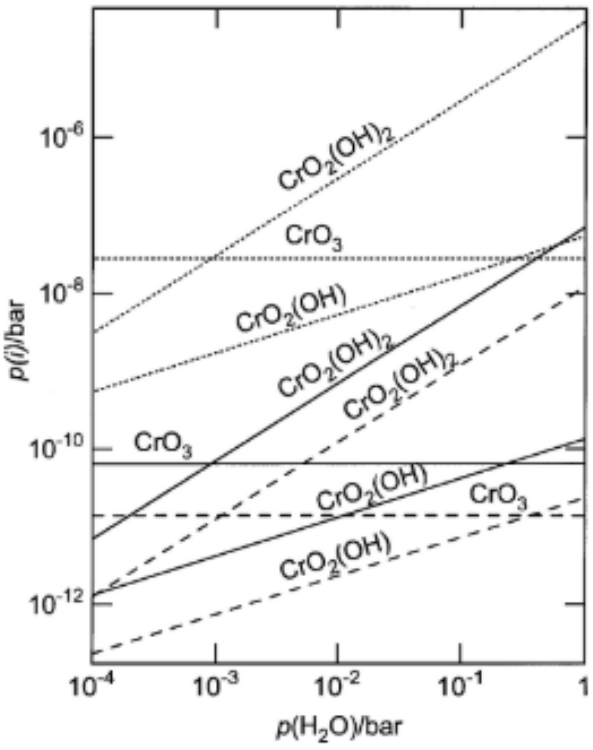


Figure 27 - Partial pressures of volatile chromium species at 950°C for $La_{0.84}Sr_{0.16}CrO_3$ (solid line), $LaCrO_3$ (dashed line), and Cr_2O_3 (dotted line) [20].

From Figure 27 it can be seen that a higher partial pressure of volatile chromium species was calculated for the strontium doped chromite. The LSC phase may be considered a solid solution of lanthanum chromite and strontium chromite, with strontium chromite being less stable. More strontium chromite, therefore, will favor a greater vapor pressure of volatile chromium species. This discussion has not been exhaustive. There are many additional perovskite materials which are being/have been pursued for interconnect coatings [34, 58, 73, 74]

Spinel coatings are also cubic and of the form AB_2O_4 where “A” and “B” may be di/tri/tetravalent cations. Spinels also show good electronic conduction, match other component CTEs in the SOFC system, and have demonstrated protection against both chromium egress and oxygen ingress. Yang et al. [75] coated E-brite, Crofer 22 APU, and AISI430 with $Mn_{1.5}Co_{1.5}O_4$ and exposed these samples to 800°C air for 100 hours. Both coated E-brite and Crofer formed a protective duplex scale consisting of internal chromia and external spinel which was observed to prevent outward chromium diffusion by EDS, and offer excellent electrical conductivity with measured ASR values as low as 7 $m\Omega\ cm^2$. While the coated AISI430 was also observed to prevent outward chromium diffusion, the lower chromium content in the alloy resulted in internal iron oxide formation, and the increased silicon content resulted in insulating silicon oxide scale formation. The increase in ASR to 40 $m\Omega\ cm^2$ was attributed to this insulating oxide formation and the increased scale growth rate. Yang et al. [76] reported similar findings when examining the same coating on uncoated and coated Crofer 22 APU, with the

uncoated alloy reaching an ASR three times higher than uncoated (39 vs 13 mΩ cm^2), and double the thickness (~4 µm vs ~2 µm).

In addition to Mn-Co spinel coatings, Bateni et al. [77] also examined $Cu_{1.4}Mn_{1.6}O_4$ coatings on FSS grade 430 interconnects exposed to 750°C air for seven days. The coating was observed to be well adherent and prevented outward chromium diffusion, though did not prevent outward diffusion of iron. Iron largely remained in solution according to XRD analysis, with copper oxide and spinel being the only identified phases. While not identified, an internal chromia layer appears to have formed when examining elemental mapping using EDS. The uncoated FSS 430 oxide scale was an order of magnitude thicker (hundreds of microns vs tens) and not well adherent, which was attributed to the CTE mismatch of magnetite and the FSS substrate.

Chromium containing spinels, such as $(Mn,Cr)_3O_4$ and $(Co,Cr)_3O_4$, have displayed acceptable oxidation resistance and electrical conductivity [78-80], but Cr in the spinel may be undesirable. While less susceptible to reactive evaporation than chromia [18, 36, 58], these scales may still result in unacceptable vapor pressures of volatile chromium species. The Mn-Co spinel discussed above has been observed to act as an effective barrier against outward Cr transport and reduce volatility by up to two orders of magnitude [34, 82, 83]. Metallic coatings of Cu, Co, and Ni on Crofer 22 APU in humid air at 800°C for up to 1200 hours by Stanislowski et al. [35] were observed to form surface Co, Cu, and Ni single element oxides, with an internal spinel layer which reduced chromium release by two orders of magnitude compared to uncoated Crofer. Similar to perovskites, there are many more studies and spinel coatings which were not covered

here [84-87]. In addition to coatings, research has been performed by placing ceramics in direct contact with stainless steels at high temperature and observing the outcome. These cases will be discussed in the next section.

To the best knowledge of the author, the impact of contacting aluminosilicate fibers on corrosion behavior has not been investigated. This contacting condition is important as SOFC getters designed to collect volatile chromium species may be supported by alumina micro/nanofibers [88] which would be in contact with FSS interconnects. Additionally, ferritic stainless steel T409 (FSS T409) is often used in automobile exhaust systems and contacts ceramic fibers in a catalytic converter. These materials may influence one another in contacting conditions, with fibers collecting various chromium species, and the corrosion behavior of FSS T409 being altered. The findings from Surface Studies of T409 Stainless Steel at 700°C in Wet or Dry Air or N_2 With and Without Contacting Ceramic Fibers, published in Oxidation of Metals in January 2018 [1], are outlined below.

Strips of FSS T409 were characterized using EDS to obtain the general composition in Table 1.

Table 1 - Composition of FSS T409 taken by EDS.

	Fe	C	Mn	Si	Cr	Ti
T409	Bal	Max: 0.08	0.5	0.4	10.5	0.2

Two strips, each 125 mm x 14 mm x 1.48 mm, were used in each experiment which were each measured, massed, and stamped for identification pre-exposure. These strips were

used to sandwich aluminosilicate fibers, provided by Morgan Advanced Materials, of approximate mass 0.4 g which spanned the length and width of the strips.

Henceforth, this placement of aluminosilicate fiber between two strips of T409 will be referred to as a clamp. An assembled clamp was placed in a quartz crucible which was housed in the center of a 30 mm OD quartz tube. The quartz tube was placed in a GSL-1100 × tube furnace, and flanges sealed with O-rings were used to connect the quartz tube to inlet and outlet tubing. The inlet to the furnace was supplied using either house air or nitrogen controlled by a three-way valve. The selected feed gas was then passed through an Omega FL-3613G rotameter to establish a flow rate of 900 sccm and then to another three-way valve to direct gas either directly into the furnace or to a 1 L glass bubbler. The bubbler was fitted with a frit of porosity rating P1 and filled with room temperature water. The inlet gas/vapor interacts with a clamp at 700 °C and exits the tube initially routed into a 500 mL Erlenmeyer flask to condense water vapor. The effluent is then directed to a fume hood for release. The experimental setup is schematically illustrated in Figure 28.

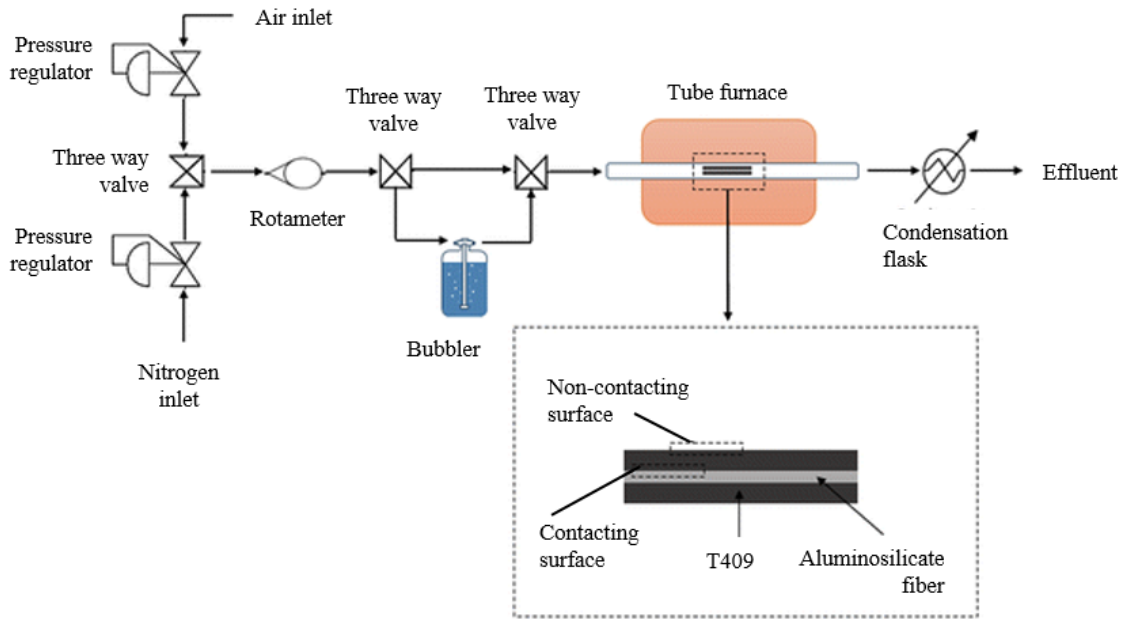


Figure 28 - Experimental setup used in Surface Studies of T409 Stainless Steel at 700°C in Wet or Dry Air or N_2 With and Without Contacting Ceramic Fibers [1].

For all experiments, the furnace ramp rate was 30 °C/min, and exposure time at 700 °C was 94 h. In the experiments using nitrogen, the system was purged of oxygen with dry nitrogen flow of 900 sccm for 20 min prior to heating the furnace. Additionally, for all experiments after the exposure period elapsed, power to the furnace was discontinued and dry gas was used during cooldown. Dry nitrogen was used for nitrogen experiments, and dry air was used for air experiments. After cooling to room temperature, each clamp was disassembled and re-massed. An Allied Techcut 4™ precision low speed saw was used to cut two coupons from a strip in each experiment. Two coupons were cut from each experiment as there were two contacting conditions. One coupon was analyzed on the side contacting aluminosilicate fiber whereas the other coupon had the non-contacting surface analyzed. These coupons were washed with methanol and acetone to remove cutting fluids. Coupons were then analyzed using field emission scanning

electron microscopy (FESEM), energy dispersive x-ray spectroscopy (EDS), and XRD. A Zeiss SUPRA 55VP was used for FESEM/EDS, and a Scintag X1 Diffraction System was used for XRD. Diffraction patterns were obtained using a Cu K-alpha X-ray source with Bragg–Brentano geometry from 15 to 70 degrees 2Θ. Samples were scanned at 0.5°/min with 0.02° steps. Separate coupons were prepared as cross sections using an Allied MultiPrep™ polishing system. Samples were mechanically ground and polished from 120 grit up to a 3-micron finish. These cross sections were examined using FESEM/EDS.

Diffraction patterns for the non-contacting and contacting surfaces are displayed in Figures 29 and 30, respectively. Surface micrographs for the non-contacting and contacting surfaces are shown in Figures 31 and 32.

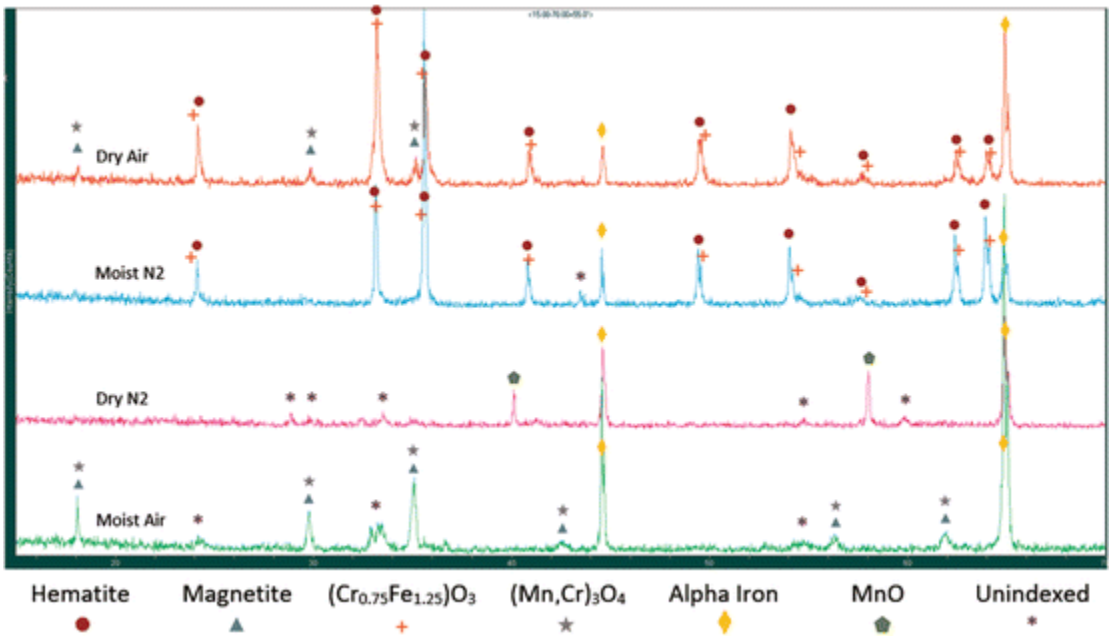


Figure 29 - Diffraction patterns for non-contacting surfaces.

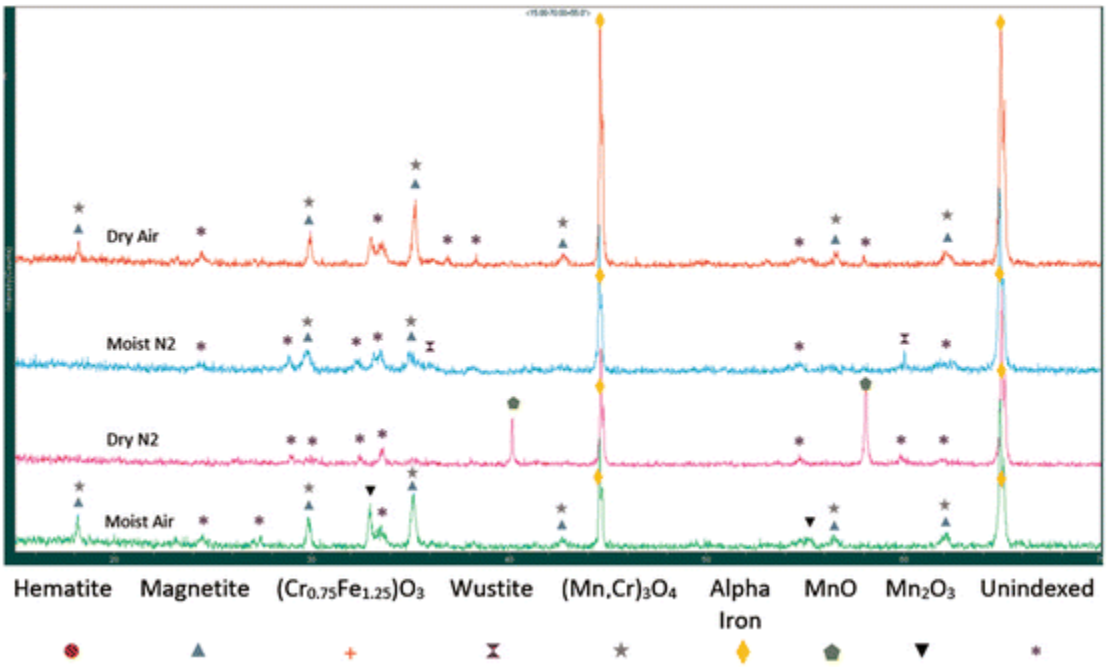


Figure 30 - Diffraction patterns for contacting surfaces.

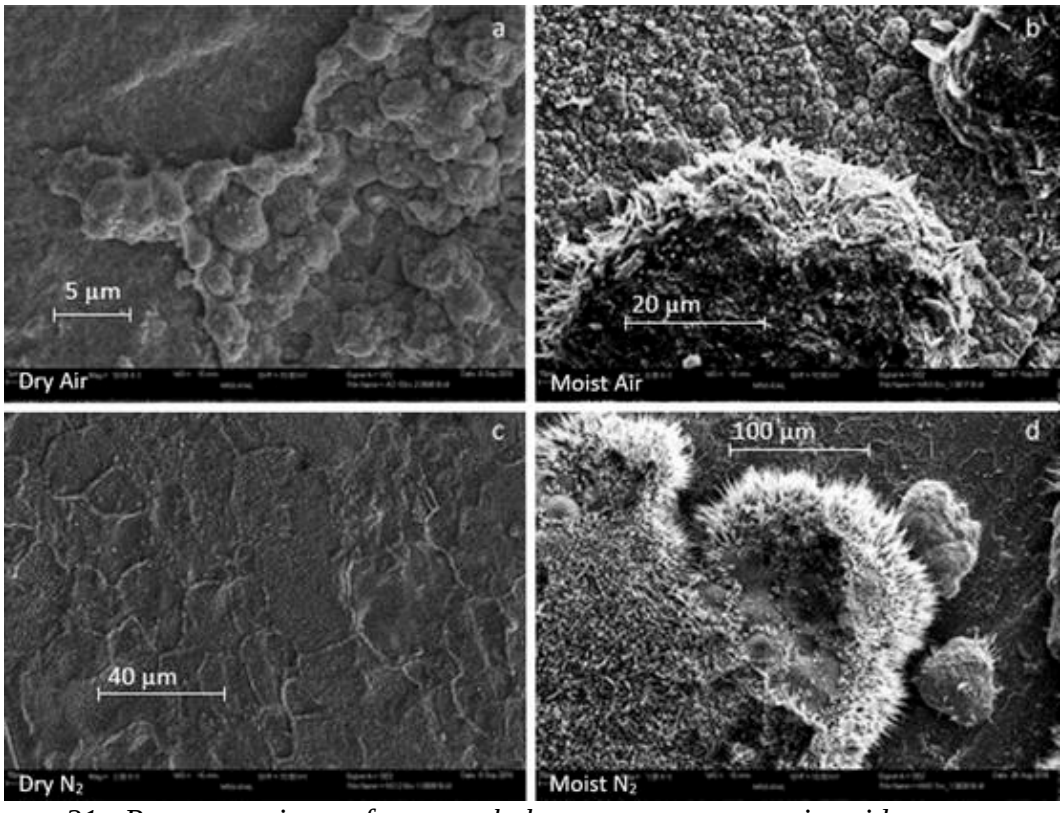


Figure 31 - Representative surface morphology post non-contacting side exposure to a) dry air b) moist air c) dry N_2 d) moist N_2.

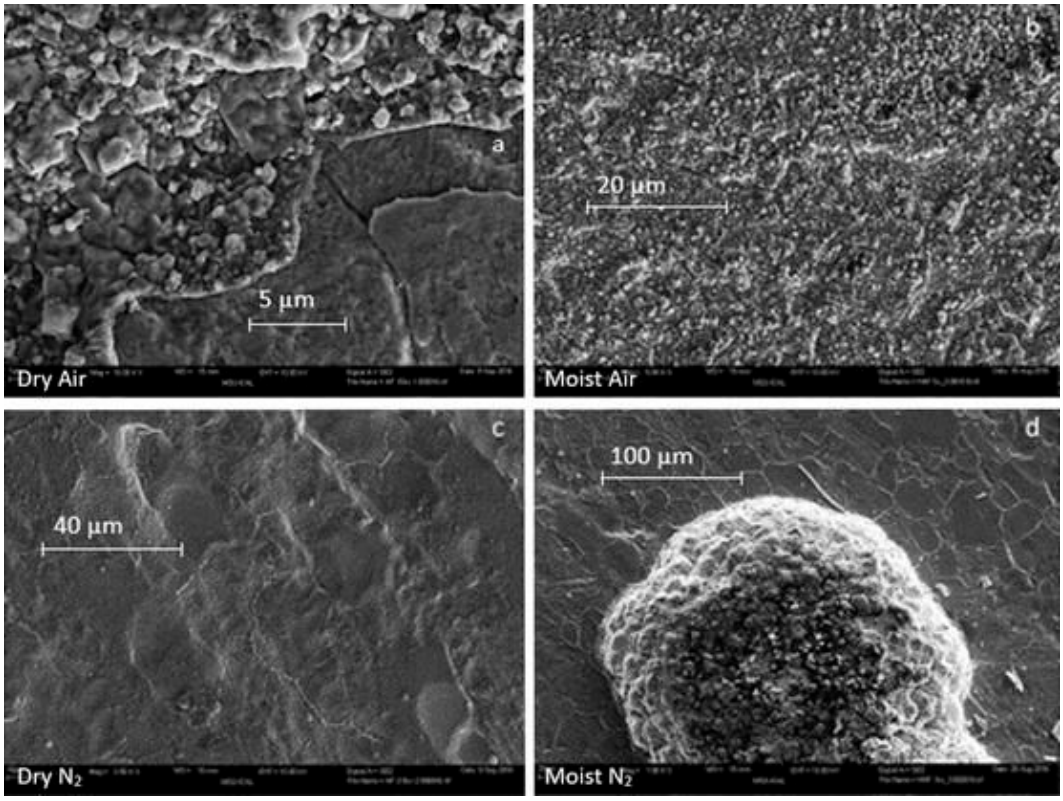


Figure 32 - Representative surface morphology post contacting side exposure to a) dry air b) moist air c) dry N_2 d) moist N_2.

Examining Figures 31 and 32, the contacting side exposures can be seen to form smaller oxide nodules than the non-contacting exposures. Oxide islands observable in Figure 31b were no longer present on Figure 32b. Additionally, oxide islands which agglomerated in Figure 31d instead form standalone units free of whiskers in Figure 32d. The diffraction patterns in Figures 29 and 30 show that hematite is no longer observed for contacting side exposures. These differences will be explained briefly here.

Smaller oxide nodules are attributed to the fibers acting as a barrier to mass transport of corrosive species. Further, it was theorized that hydrogen will more easily infiltrate the barrier than other larger species such as oxygen and water vapor. This may result in an inflated hydrogen composition in the fibers relative to the influent. The

significance of increased hydrogen content may be seen from an Ellingham diagram as was shown in Figure 18. An Ellingham diagram is used to predict thermodynamic stability at a given temperature for a given reaction. The necessary oxygen partial pressure to oxidize, or the requisite CO/CO_2, H_2/H_2O ratios to reduce are displayed on the top, right, and bottom axes. These ratios drive reduction due to Le Chatelier's principle, which essentially states that a system will seek a new equilibrium when subjected to a change in pressure, temperature, or concentration. A large H_2/H_2O ratio will drive the reaction equilibrium towards the formation of water, and consequently the consumption of oxygen. It is in this way that the gas atmosphere of the fiber region may produce smaller oxide nodules relative to non-contacting conditions and suppress hematite formation.

The fibers acting as a mass transport barrier and also inflating the H_2/H_2O ratio help to explain why oxide islands are not present in the contacting humidified air exposure while they are present in the non-contacting case. These oxide islands are believed to form by the volatilization induced localized breakaway corrosion mechanism discussed near the end of the previous section from Asteman et al. and Segerdahl et al. [60, 61]. By this mechanism the rate of reactive evaporation of chromium exceeds the rate at which chromium may be replenished in the scale, resulting in localized breakdown of protective behavior and a fast growing oxide island. By reducing ingress of oxygen and water vapor, inflating the H_2/H_2O ratio, and slowing egress of volatile chromium species the volatilization rate slows. From this work it appears to slow enough to prevent the breakaway corrosion mechanism from occurring in the fiber region.

This mechanism is incompatible with oxide island formation in the moist N_2 exposures as these are low pO_2 conditions. An alternative mechanism was proposed in the paper in which alloy segregation, which may be observed from suboxide formation (morphology resembling weld beads in Figures 31c,d and 32 c,d), was largely responsible for oxide island formation. Alloy segregation is driven by Gibbs energy of segregation shown in Equation 2.56.

$$\Delta G_I = \Delta G_I^0 + \Delta \bar{G}_I^E \tag{2.56}$$

$$\Delta G_I^0 = \left(\mu_{I(M)}^{\phi,0} + \mu_M^{V,0}\right) - \left(\mu_{I(M)}^{V,0} + \mu_M^{\phi,0}\right) \tag{2.57}$$

$$\Delta \bar{G}_I^E = RT \cdot \ln\left(\frac{\gamma_I^{\phi}\gamma_M^{V}}{\gamma_I^{V}\gamma_M^{\phi}}\right) \tag{2.58}$$

ΔG_I – Gibbs energy of segregation

ΔG_I^0 – Standard molar Gibbs energy of segregation

$\Delta \bar{G}_I^E$ – Partial molar excess Gibbs energy of segregation

I – Solute

M – Solvent

ϕ – Interface

V – Bulk volume

γ – Activity coefficient

Gibbs energy of segregation is the addition of the standard molar Gibbs energy of segregation and the partial molar excess Gibbs energy of segregation. The standard molar Gibbs energy of segregation is the difference between the sum of the chemical potential

of pure solute occupying an interfacial position and solvent in the bulk, and the sum of the chemical potential of solute in the bulk and solvent in the interface. The partial molar excess Gibbs energy of segregation represents the deviation between ideal behavior (ΔG_I^0) and real behavior. It takes into account the activity coefficients, which when multiplied by concentration gives activity. Examination of Equation 2.58 shows that when the product of activity coefficients of solute in interface and solvent in bulk is less than the product of the opposite, then solute segregation to the interface is energetically favorable. Limited reactivity at the surface leads to an attenuated driving force toward the surface for atoms in the bulk. Solutes, in this case elements such as Mn, Cr, and Ti may segregate to grain boundaries seeking lower energy states and engage in accelerated diffusion toward the surface. This leaves surface regions not supplied by grain boundaries susceptible to localized breakaway corrosion.

Factors which may exacerbate this process include the dissolution of protons into the scale, potentially increasing the solubility and/or diffusivity of iron in chromia [89], and water ingress through micro-cracks forming H_2O-H_2 bridges which may cause internal oxidation and form volatile iron hydroxide [64]. These bridges allow for water ingress, which may then dissociate with hydrogen escaping out the micro-crack and oxygen interacting with iron to form iron oxide. Alternatively, water may react with iron oxides to form iron hydroxide leading to void formation and porosity within the scale. As was noted at the end of the last section, Ehlers et al. [64] also reported that gas environments where the pH_2O/pO_2 ratio is ≥ 1 will result in water outcompeting oxygen for adsorption sites. Water will preferentially adsorb with lower isoelectric point

magnetite/hematite versus chromia [64, 90, 91] further exacerbating breakdown of the protective scale. These factors were believed to result in the formation of iron oxide islands in low pO_2 environments, with the proposed mechanism displayed in Figure 33. Differences in island agglomeration (Figure 31d) vs standalone units (Figure 32d) was believed to be due to the fibers acting as a barrier to mass transport resulting in less extensive oxidation.

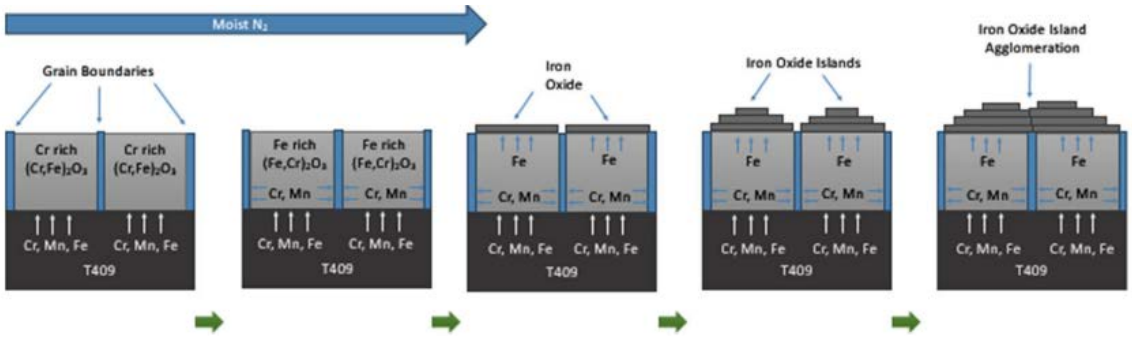


Figure 33 - Proposed mechanism for iron oxide island formation in non-contacting/contacting moist N_2.

Whisker formation was also notably influenced by fiber contact and water content. Formation of iron oxide whiskers is well understood to be heavily influenced by the presence of water vapor [92]. The diffusion of iron through parallel dislocations allows for a fast-growing surface region, resulting in a high energy irregular mound which attracts oxidant molecules. Upon adsorption, water dissociates more quickly than oxygen which allows for rapid growth of the whisker. It has also been noted that water will preferentially adsorb with hematite/magnetite if the pH_2O/pO_2 ratio is ≥ 1. This matches the experimental results, as non-contacting moist air (Figure 31b) formed few, low aspect ratio whiskers with non-negligible Cr and Mn content, whereas non-

contacting moist N_2 (Figure 31d) formed many high aspect ratio whiskers lacking Cr or Mn. The “veins” seen in Figure 34 likely formed by the same mechanism, but were not free to grow in any direction as they were in direct contact with fiber barriers. Iron transport form dislocations was perhaps led in circuitous routes on the oxide surface due to impeding fiber barriers. The irregular formation still presented a high energy location attracting water molecules which then dissociated to grow surface veins.

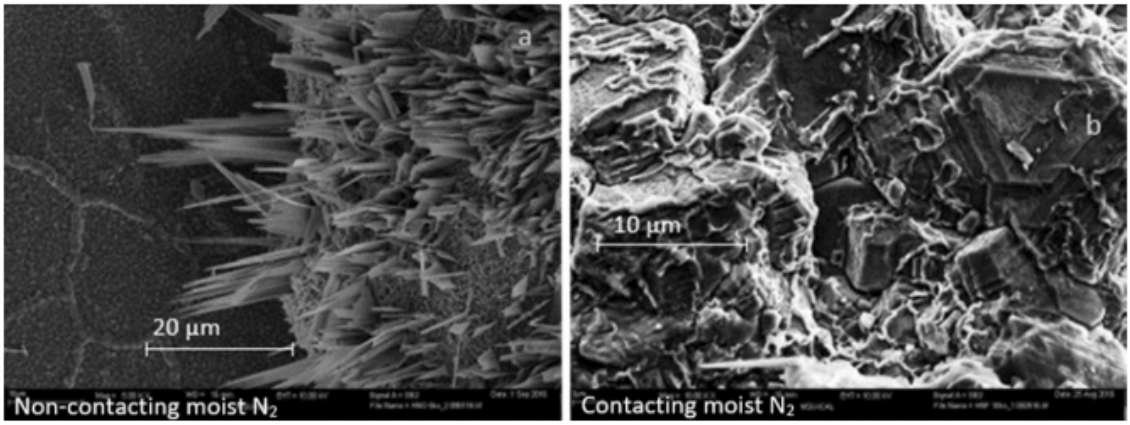


Figure 34 – Whiskers a) formed in non-contacting case versus b) formed in contacting case.

Lastly, fibers were analyzed for evidence volatile chromium species reactive condensation via inductively coupled plasma mass spectroscopy (ICP-MS). Fibers in dry and moist N_2 did not collect enough chromium to meet the detection limit for the technique (0.005 mg/L). The importance of oxygen for chromium volatility has been discussed. If fibers are to possess chromium in experiments with low pO_2 values, then the chromium must transfer from FSS T409 via solid-state diffusion.

While solid-state diffusion of chromium into glass has been observed [93, 94], it does not appear to be a prominent transport mechanism in these experiments. It is

possible that solid-state diffusion did occur, but the fibers did not present many flush contacting points for this to occur appreciably. Fibers in dry and moist air exposures did possess detectable levels of total chromium, with 0.03 and 0.054 mg/L total chromium, respectively. Table 2 shows the total chromium content for each gas exposure.

Table 2 - Total chromium content on fibers for each gas exposure. ND – Not detected.

Gas Exposure	Total Chromium Content (mg/L)
Dry air	0.03
Dry N_2	ND
Moist air	0.054
Moist N_2	ND

Due to the lack of evidence for solid-state diffusion, the chromium present on fibers exposed in dry/moist air is likely a result of reactive evaporation and condensation. For moist air, $CrO_2(OH)_2$ is the dominant volatile chromium product, whereas CrO_3 is the dominant product in the dry air [31-36]. An investigation of the interaction between volatile chromium species and aluminosilicate fibers, in addition to other ceramic materials, is presented in Chapter 5.

CHAPTER THREE

VOLATILE CHROMIUM SPECIES AND SOLID OXIDE FUEL CELLS

Content in Chapter Three

Chapter Three contains information on the basic operating principle of SOFCs, materials of construction for various SOFC components, and literature on the interaction of chromium vapor species and SOFC components. Experts in this area may proceed to Interactions between Volatile Chromium Species and Solid Oxide Fuel Cell Components to examine the relevant literature presented. None of the work presented in this chapter is attributable to the author of this dissertation.

Solid Oxide Fuel Cell Basics

As was mentioned in the introduction, a SOFC consists of two electrodes separated by an electrolyte which conducts oxide ions. Hydrogen (or other fuels, e.g., CO, CH_4) is oxidized at the anode/electrolyte interface and the electrons created serve to generate a current and reduce oxygen at the cathode/electrolyte interface. This process is illustrated in Figure 35.

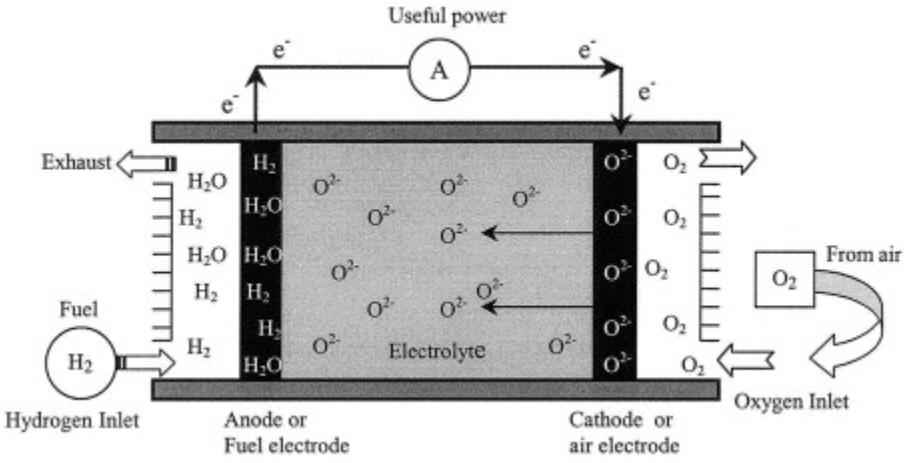


Figure 35 - Schematic of SOFC [21].

One cell, consisting of the anode, cathode, and electrolyte, produces less than 1 Volt [22]. For practical use of SOFC technology, cells must be stacked and interconnected to obtain higher voltage and power. Stacked cells, in planar and tubular configuration, are displayed in Figures 36-38. Figure 36 displays an illustration of the various components of a planar repeating unit, with Figure 37 showing a scaled 5 kW SOFC planar stack from the Jülich Research Centre. Figure 38 is an illustration of a tubular design in which air may enter a tube in the center of the open side, proceed to the end of the closed tube, and be routed out along the outside of the inlet tube flowing countercurrent to the inlet air.

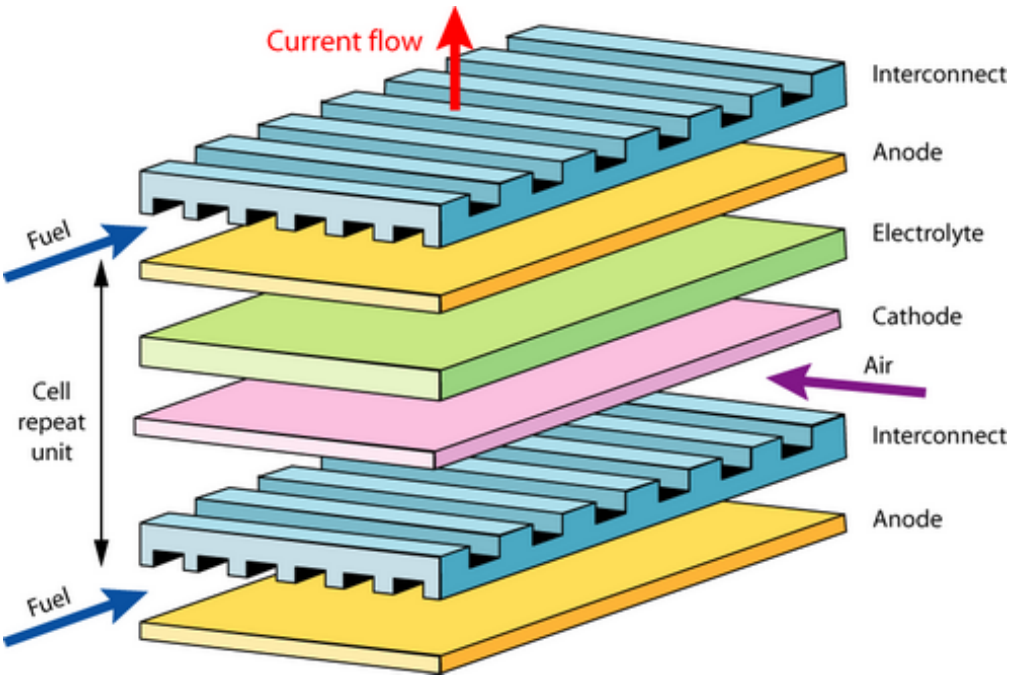


Figure 36 - Planar stacked SOFC schematic. Credit: doitpoms.ac.uk.



Figure 37 - Planar stack SOFC capable of producing 5 kW. Credit: Research Centre Jülich.

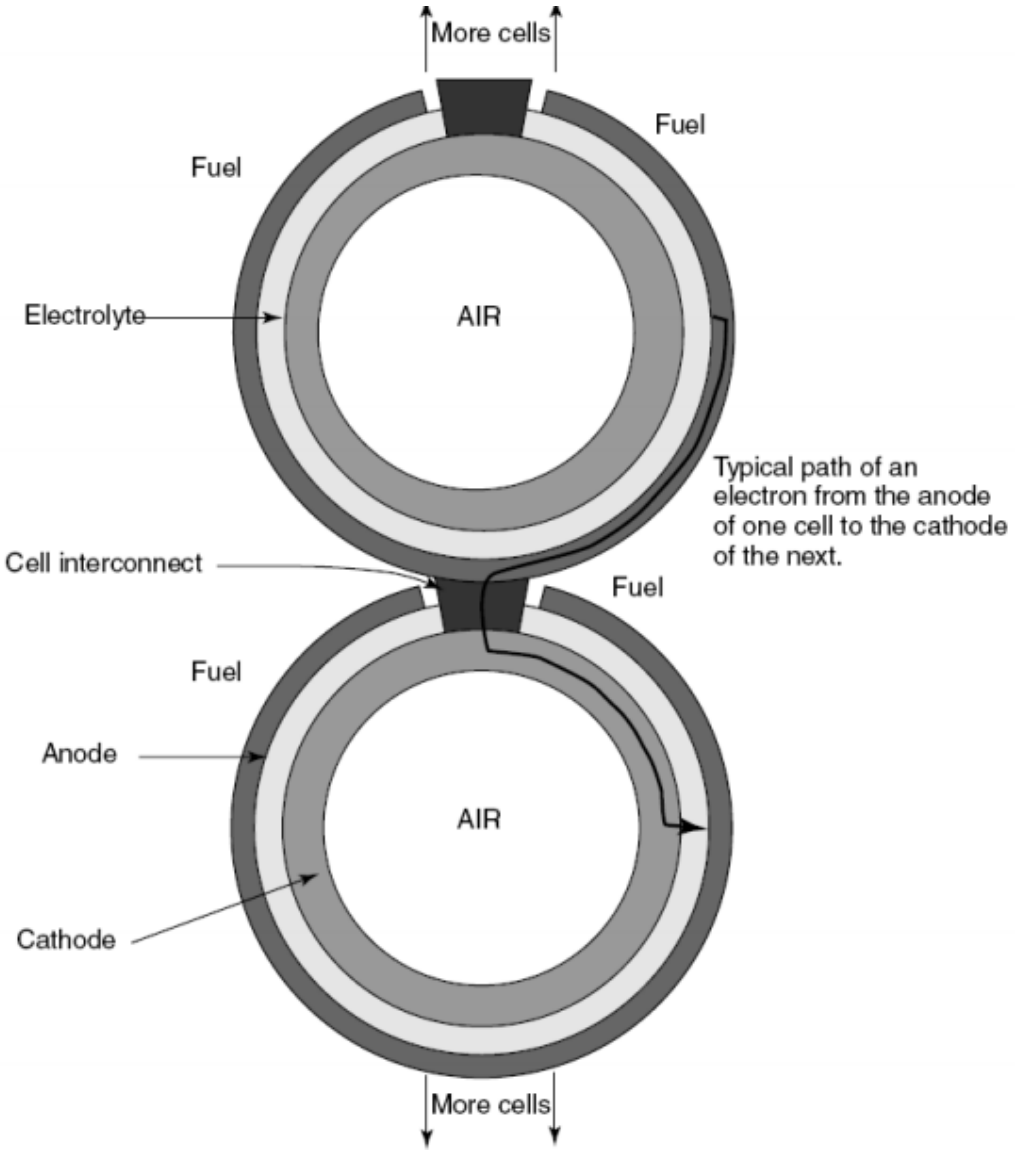


Figure 38 - Tubular stacked SOFC schematic [95].

Planar stacks have the advantage of higher areal power density [22], but require high temperature sealant to keep fuel and air streams from mixing. Tubular designs do not require this sealant, as separation of fuel and air is intrinsic to the tubular design. Tubular designs of this kind have one end open and one closed, so air may enter and exit through this open end and fuel may be flowed past the closed end of the tube. Alternative

tubular geometries are being developed, however, in an effort to increase the areal power density [97].

Each component in a SOFC must meet several requirements in order to produce an efficient and lasting system. General considerations include: chemical compatibility with other components, chemical and phase stability in its respective gas environment, a low vapor pressure, similar coefficients of thermal expansion, and cost competitive in terms of fabricability and material cost [22, 96, 97].

Material Selection for Solid Oxide Fuel Cell Components

As a SOFC requires separation of fuel and air/oxygen, the electrolyte must be sufficiently dense to preclude mixing of the gases. The electrolyte must be an ionic conductor and an electronic insulator. An ionic conductivity on the order of 0.01 S/cm or greater at or above 600°C is the lower bound of an acceptable conductivity [71]. Yttria stabilized zirconia (YSZ) is often used due it its superior oxygen ion conductivity, low electronic conductivity, and high chemical and thermal stability [71]. Zirconia is doped with ≥ 8 mol% yttria to stabilize the cubic phase well below the phase transformation temperature of 2680°C for pure zirconia [71]. Stabilizing the cubic phase is useful as it has a greater oxygen ion conductivity than the monoclinic or tetragonal phases [71]. As attempts to reduce operating temperatures continue, alternative materials with higher ionic conductivities such as doped ceria and doped lanthanum gallate are being considered [71]. While having higher ionic conductivity, tradeoffs of doped ceria include low mechanical strength and chemical stability, and lanthanum gallate is not chemically compatible with NiO anodes [98]. There are also attempts to reduce the electrolyte

thickness to minimize ohmic losses for YSZ at lower temperatures. Current thicknesses of ~150 μm are being reduced as much as sub-micron thickness with some success [99, 100], but questions of scalability and cost considerations for mass production of kW-MW scale SOFCs have been raised [101].

Cathode materials must be sufficiently porous (~30-40% [71]) to allow oxygen access and be chemically stable in gas atmospheres where $pO_2 \geq 20$ kPa. They must also have excellent catalytic activity for the oxygen reduction reaction (ORR), a large triple phase boundary region with minimal interfacial reactions, and high electronic and ionic conductivity [102]. Perovskites are commonly used as cathode materials, with examples being lanthanum strontium manganite (LSM), lanthanum strontium-cobalt ferrite (LSCF), and lanthanum nickel ferrite (LNF). As LSM has poor ionic conductivity, the ORR is restricted to the TPB, whereas LSCF and LNF are both mixed ionic and electronic conductors (MIECs) which allows for electrochemical reactions at two phase cathode/gas interfaces [24, 102]. Of LNF and LSCF, LNF has shown superior resistance to Cr poisoning [103, 104], but LNF is also quite reactive towards zirconia based electrolytes, forming an insulating $La_2Zr_2O_7$ product during sintering [105]. There are barrier coatings, such as gadolinia doped ceria (GDC), which may serve to prevent insulating phase formation between cathode and electrolyte materials such as the reaction with LNF and zirconia based electrolytes [102]. Additional approaches include combining the beneficial properties of different cathode materials by thin film coating a MIEC such as LSCF with LSM, granting the benefits of ionic conductivity and high catalytic activity [106].

Anode materials must has porosity similar to cathode materials to allow ingress of fuel, but the chemical stability required is for gas atmospheres where $pO_2 \leq 10^{-17}$ kPa. The fuel for a SOFC is flexible so catalytic activity will be tailored to the fuel. In the case of hydrogen fuel, Ni/YSZ cermet materials are a common choice due to the high catalytic activity of Ni for H-H bond dissociation and the relatively low cost of Ni [71]. Nickel in these cermets tends to agglomerate and coarsen over time, reducing porosity, TPB access, and cell performance [107]. In the case of hydrocarbon based fuels Ni/YSZ is not appropriate as they are not sufficiently resistant to coking, or the deposition of carbon rich solids [108]. Alternative materials, such as copper-gadolinium doped ceria are being developed which resist coking and have suitable conductivity [108].

Interconnects must separate fuel and air streams, provide structural support for the SOFC, and be electronically conductive. An upper limit for SOFC interconnector area specific resistance (ASR) is generally accepted to be 0.1 Ω cm^2 [109, 110]. With the transition to lower operating temperatures (650-800°C) more easily fabricable metallic interconnect materials have replaced ceramic interconnects. Based on required coefficients of thermal expansion (CTE) ($\sim$10 x 10^{-6} °C^{-1} from 25-1000°C [111, 112]), acceptable high temperature oxidation resistance, and conductivity requirements ferritic stainless steels are often chosen as metallic interconnect materials. Austenitic stainless steels do not met CTE requirements. Alloys may not be alumina formers as alumina scales are insulating. Silicon content in amounts greater than $\sim$0.5 wt% is also not desirable due to a tendency for insulating silica layers to form [81, 112]. While meeting the baseline requirements, ferritic stainless steels still present several issues as

interconnect materials. The ASR increases precipitously as the oxide scale thickens [113] and with interfacial imperfections at the metal/oxide interface such as voids [114]. Surface modifications, such as shot peening and polishing, introduce dislocations at the surface. These dislocations provide accelerated diffusion paths for chromium, and if above the recovery and recrystallization temperature, allow for the formation of a thin, fine grained protective oxide [11, 115]. This would minimize scale thickness, but chromium volatilization and subsequent poisoning of the cathode may proceed unmitigated. Coatings of reactive element oxide, perovskite, and spinel may allow for thin, conductive scales which are resistant to Cr volatility [116-119]. Examples include Y or Co/Ce coatings [66, 120], lanthanum strontium chromites/ferrites [34, 118] and $(Mn,Co)_3O_4$ or $(Mn,Cu)_3O_4$ [68, 83, 121]. Alternative alloys are also being developed which reduce Si and Al impurities and may include reactive elements which are theorized to segregate to grain boundaries to block/slow short circuit diffusion, and serve as closely spaced surface nucleation points to promote a thin, fine grained scale [65]. Alloys of this type include Crofer 22 APU and ZMG232 [122].

Sealant material for SOFCs must be stable over the range of pO_2 for both the fuel and air side, be minimally reactive with surrounding materials, and remain impermeable for the lifetime of the system. Commonly employed seals are glass-ceramics such as silicates, borosilicates, and boroaluminosilicates [123]. These materials have a suitable CTE and glass transition temperature (T_g) [124], which is the temperature at which a glassy material transitions to a viscous liquid state. A low T_g is desirable to combat thermal stress generation in the seal which may cause brittle failure, but the T_g must high

enough to provide mechanical integrity and prevent the sealant from flowing ($\mu \sim 10^3$ Pa s). Alternatively, brazes comprised of noble metals such as silver and gold may be used which may better deform to tolerate thermal stresses. These brazes often poorly wet the metal/ceramic surfaces alone, so composites such as Ag-CuO are used, where increasing CuO content increases surface wetting [123]. The glass-ceramic and brazes described are rigid seals, but compressive seals are also being pursued. Compressive seals have the advantage of not requiring precise matching of CTE, though constant pressure is required throughout operation. Mica-based compressive seals where a mica layer is infiltrated with a compound to fill void space (such as $Bi(NO_3)_3$) and sandwiched between glass or silver layers have demonstrated low leak rates and excellent durability [125].

Interactions between Volatile Chromium Species and Solid Oxide Fuel Cell Components

Cathode and Electrolyte.

Volatile chromium species have been observed to interact at both two phase and triple phase boundaries. Electrochemical deposition at the TPB is shown in Figure 39, in which chromium oxyhydroxide is reduced and deposited as chromia with hole transport through the cathode and oxygen vacancy transport through the electrolyte. Electron holes, or holes, are the absence of an electron in the valence band. Electron transport may be facilitated using these holes analogously to atomic transport through vacancy diffusion. Materials which conduct holes are classified as p-type.

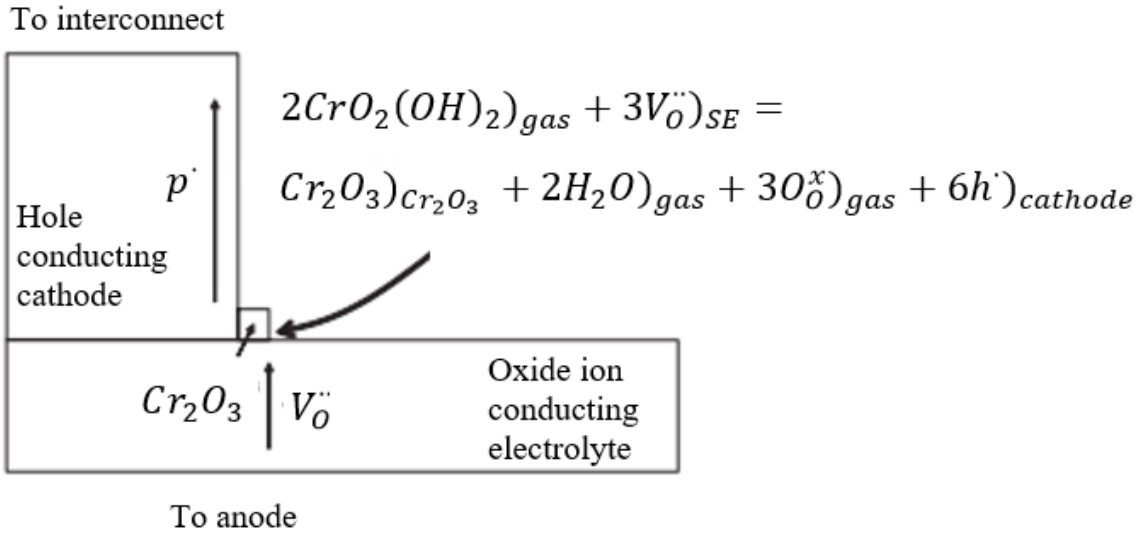


Figure 39 - Electrochemical deposition of chromium oxyhydroxide at TPB. Redrawn from [24].

$V_o^{\cdot\cdot}$ – Oxygen vacancy with double positive charge

$p^{\cdot}/h^{\cdot}$ – Electron hole with single positive charge

O_o^x – Oxygen in oxygen site with neutral charge

Two phase boundary interactions include both gas/cathode and gas/electrolyte [24]. At gas/electrolyte surfaces, chromia has been observed to deposit hundreds of microns away from a TPB site [24]. Paulson and Birss [126] proposed that this actually constituted an extension of the TPB, as the conductivity of chromia at high temperature (0.2 to 0.02 S/cm at 800°C [126]) may be on the same order as the hole conducting cathode. Figure 40 displays a continuous layer of chromia acting as a p-type conductor in the electrochemical reduction of chromium oxyhydroxide with oxygen vacancies supplied by the electrolyte.

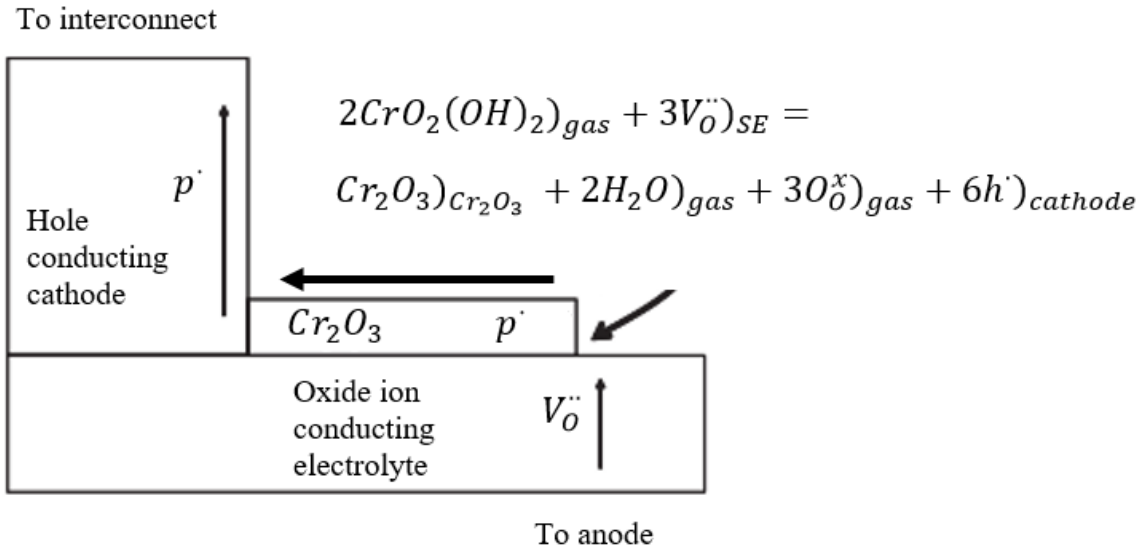


Figure 40 - Extension of TPB through p-type chromia. Redrawn from [24].

It was also noted by Fergus [24] that this chromia layer need not be continuous if the electrolyte is an MIEC. An MIEC is capable of the requisite oxygen vacancy and hole transport, so isolated pockets of chromia formed by electrochemical reduction of chromium oxyhydroxide away from the TPB is possible and shown in Figure 41.

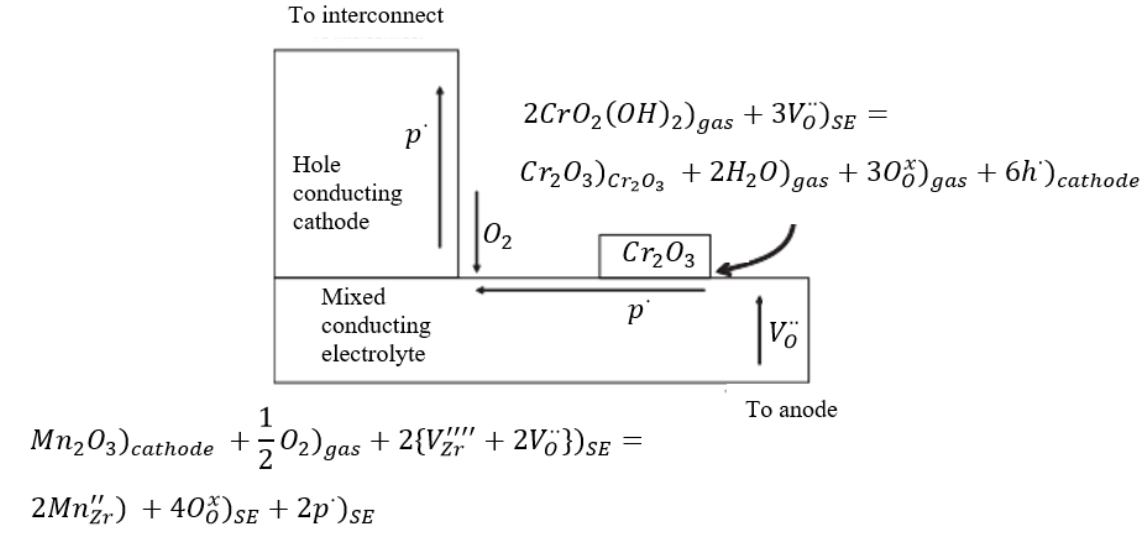


Figure 41 - Extension of the TPB with an MIEC electrolyte. Redrawn from [24].

V_{Zr}'''' – Zirconium vacancy with quadruple negative charge

Mn_{Zr}'' – Manganese in zirconium site with double negative charge

In the case of a MIEC cathode, then electrochemical deposition may take place at the cathode/gas interface as shown in Figure 42.

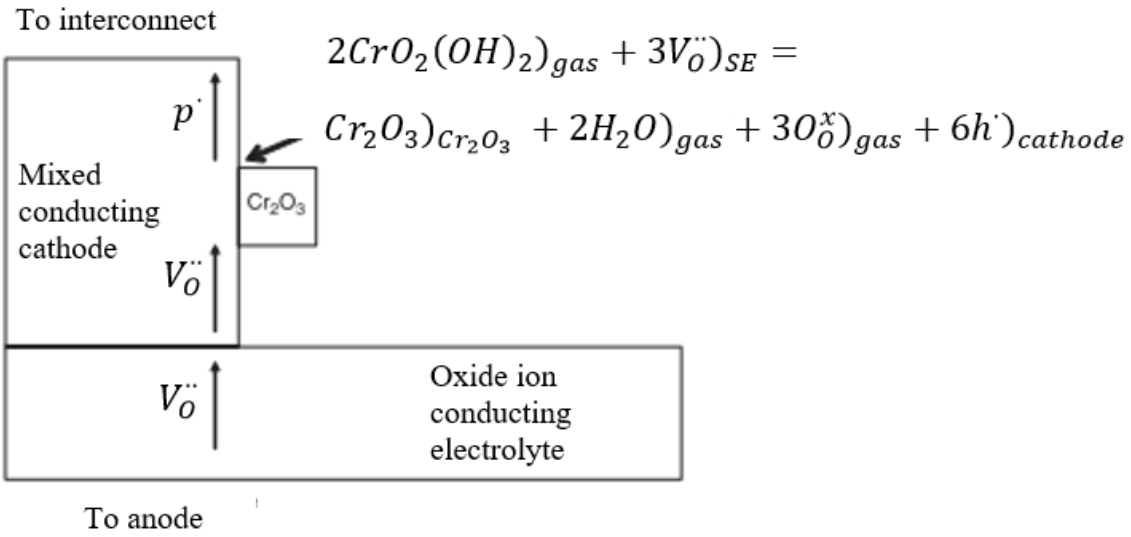


Figure 42 - Electrochemical deposition of chromia at cathode/gas interface. Redrawn from [24].

While there is evidence for preferential electrochemical reduction of chromium oxyhydroxide [24, 112, 128, 129], open circuit chemical reactions have also been observed with cathodes containing Mn or Sr [103]. Figure 43 shows chemical deposition of chromium oxyhydroxide at the TPB for a p-type cathode and oxygen ion conducting electrolyte. According to the model proposed by Jiang et al. [129], Mn^{3+} at the LSM surface is reduced to Mn^{2+} during polarization which reacts with chromium oxyhydroxide to form Cr-Mn-O nuclei with oxygen vacancies supplied by the electrolyte. These nuclei may continue to react with chromium oxyhydroxide to form chromia and $(Cr,Mn)_3O_4$.

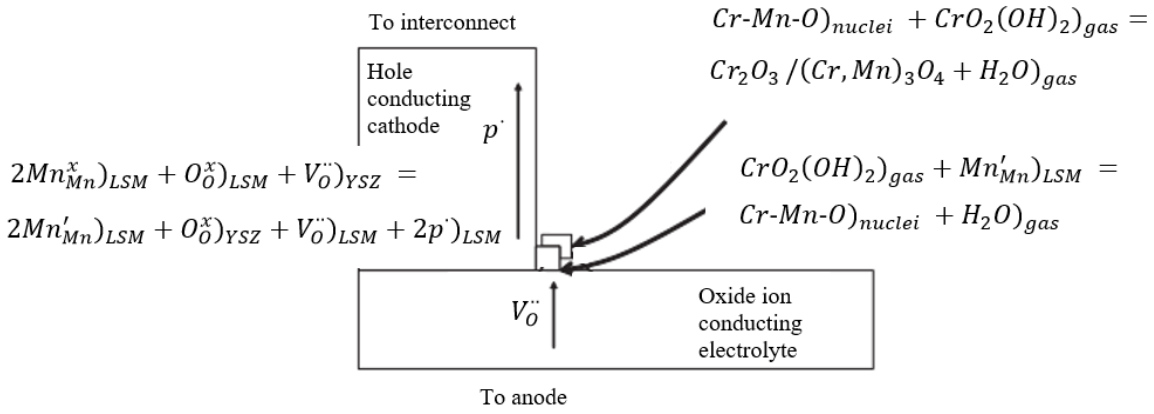


Figure 43 - Chemical deposition with p-type cathode. Redrawn from [24].

Mn_{Mn}^{x}– Manganese in manganese site with neutral charge

$Mn_{Mn}^{\prime}$– Manganese in manganese site with single negative charge

In the case of LSCF, or SrO coated LSM, then chemical deposition may take place at the cathode/gas interface as shown in Figure 44. In this model strontium oxide may react with chromium oxyhydroxide to form Cr-Sr-O nuclei which may continue to react to form chromia and strontium chromate.

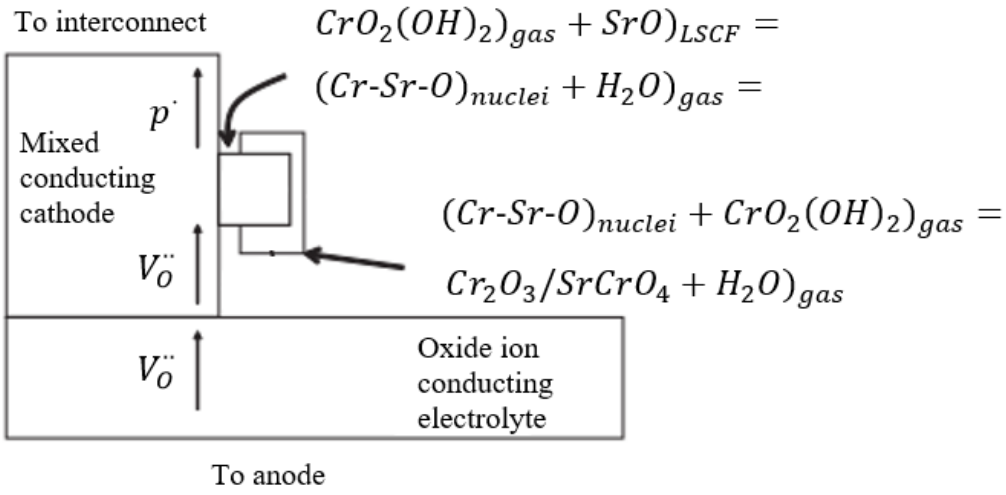


Figure 44 - Chemical deposition with LSCF cathode. Redrawn from [24].

Tucker et al. [130] reported similar findings, with both strontium oxide and LSCF allowing for significant vapor and solid state transport of Cr at 700-1000°C for 150 hour exposures. Manganese oxide and LSM allowed for significant solid state diffusion of Cr with contacting steel, but MnO only demonstrated trace vapor deposition whereas chromium was not detectable on LSM through vapor transport. Similar observations were reported by Lau et al. [103] who exposed LSM, LSCF, and LNF to 700°C environments containing volatile chromium species for 300 hours. Part of these surfaces were in contact with stainless steel interconnects and chromia blocks. Reaction couples were also created by mixing chromia and the cathode materials, pressing them into pellets, and exposing them to 700°C air for 300 hours. Both LSM and LSCF reaction couples were observed to react with chromia to produce $(Cr,Mn)_3O_4$ and $SrCrO_4$, respectively. The reaction with LSM was deemed minor as pure chromia and LSM peaks still dominated the XRD pattern, but LSCF was observed to undergo vigorous reaction as no pure chromia or LSCF was retained in the XRD pattern. No reaction was detectable for the LNF-chromia reaction couple. With respect to solid state and vapor transport, similar observations were made to those made in the Tucker et al. study [130] where surface diffusion of Cr was observed for both LSM and LSCF, but vapor transport was not observed on LSM while being significant on LSCF. While showing minimal reactivity, LNF was observed to collect chromium through both solid state diffusion and vapor transport.

Sealing Glass. Strontium chromate formation as observed between volatile chromium species and LSCF has also been observed with SrO containing sealing glass. Zhang et al. [131] joined G#36 pastes to 430SS substrate surface and held them in air at

800°C for up to two weeks. Figure 45 shows the G#36/430SS at the start, after 1 week, and after 2 weeks of exposure. Yellow discoloration of the glass is observed to form around the edges and progress inward over time. Auger electron depth profiling revealed diffusion of chromium into the glass, with a greater Cr/Si ratio observed near the edge than in the center as shown in Figure 46.

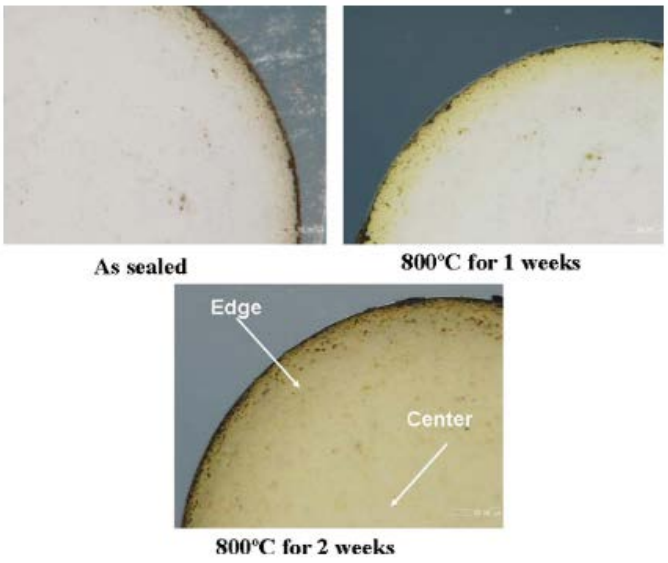


Figure 45 - G#18/430SS exposed to air at 800°C for up to two weeks. Yellow discoloration represents SrCrO4 formation [131].

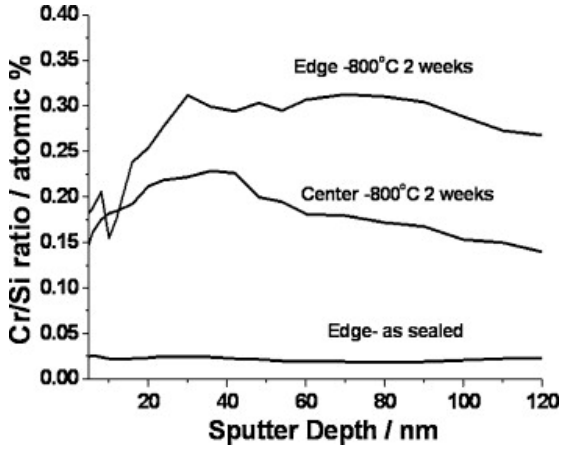


Figure 46 - AES depth profiling of joined G#36/430SS [131].

Thermodynamic modeling was also performed in which the formation of strontium chromate from chromia and strontium oxide was noted to be energetically favorable beyond 1000°C with 0.2 atm pO_2. At 900°C, a pO_2 of ~$10^{-7.2}$ atm or greater was calculated as necessary for energetic favorability. Modeling was also performed for strontium chromate formation at 0.2 atm pO_2 from CrO_3(g) and SrO which was also reported to be energetically favorable over 1000°C.

Chromia and G#18 powder were mixed and heated in air to 950°C for 24 hours, and the yellow discolored product was subjected to XRD analysis which confirmed the formation of $SrCrO_4$. The study's authors propose that strontium chromate formation occurs near the edge with a high pO_2 through interaction with chromia and/or CrO_3, and ingress of oxygen is facilitated by separation of the glass-ceramic from the metal due to differences in CTE and due to formation of a more porous $SrCrO_4$ phase. The reaction proceeds inward as the oxygen partial pressure rises to allow reaction with chromia and/or non-negligible partial pressure of CrO_3.

Similar findings have been reported by Yang et al. [132] using barium-calcium-aluminosilicate based glass-ceramic G18 and ferritic stainless steels. The G18 samples were tape cast and joined between FSS coupons at 850°C for one hour and then lowered to 750°C for four hours. Barium oxide reacted with chromia and/or volatile chromium species to form $BaCrO_4$ which resulted in de-adhesion of G18 and FSS 446 as shown in Figure 47. Separation of G18 and FSS 446 was due to differences in CTE between $BaCrO_4$ and G18/FSS 446. Yellow discoloration was observed on G18 and attributed to $BaCrO_4$ formation. While $BaCrO_4$ was not identified using a phase identification

technique in this study, a separate study performed by Yang et al. [133] identified this phase using XRD.

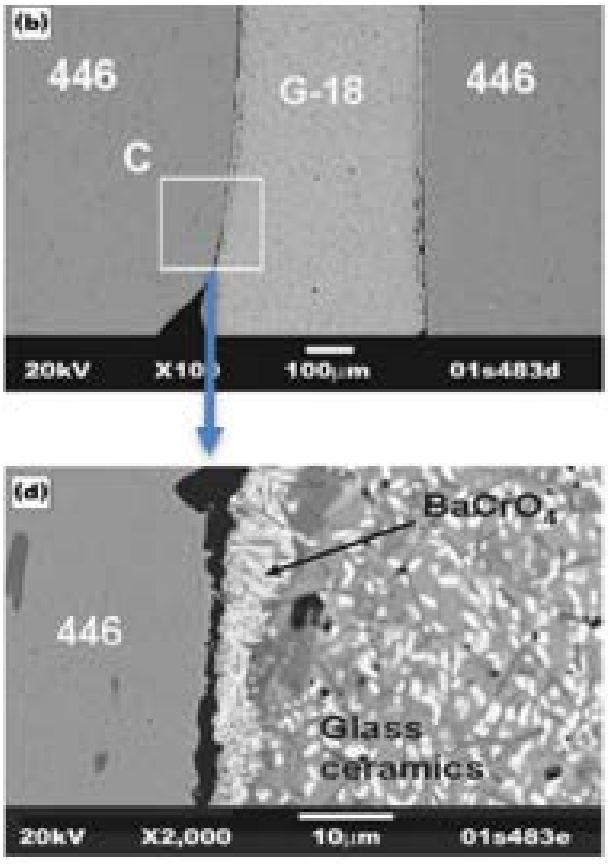


Figure 47 - Interfacial interaction between G18 and FSS 446.

Interior regions where $BaCrO_4$ did not form were still well adhered. Energy dispersive x-ray spectroscopy was used to observe the diffusion of chromium into G18, forming a solid solution in these well adhered regions.

The above overview shows the potential for volatile chromium species to reactively condense onto a variety of ceramic surfaces. Both chromia (Cr(III)) and chromate (Cr(VI)) were observed, with chromate formation being encouraged by the

presence of strontium and/or barium. Alkaline earth metals are not required for chromate formation, however, as ceramic chromium oxide catalyst supports often lack these elements but still exhibit chromate formation.

CHAPTER FOUR

CHROMIUM ON CERAMIC CATALYST SUPPORTS

Content in Chapter Four

Chapter Four contains background information on the use of chromium supported catalyst supports and their preparation, as well as literature observations for surface chromium speciation on these supports under hydrated and calcined conditions. Experts in this area may proceed to Surface Chromium Compound Formation to examine the relevant literature. None of the work presented in this chapter is attributable to the author of this dissertation.

Catalyst Supports

Over a third of all polyethylene is produced by polymerization of olefins, or alkenes, over supported chromium oxide catalysts [134]. Polyethylene is used in a variety of products ranging from plastic bags to toys to hip replacement implants, and with 100 million tonnes produced annually it accounts for 31% of the global plastics market [135, 136]. Alkenes containing no more than eight carbon atoms are able to be polymerized and create over fifty different types of polyethylene [134]. There are several industrial modes in which this polymerization process takes place. The first is a solution process, in which monomer and polymer in a cycloalkane solvent interact with suspended catalyst particles at 125-175°C and 20-30 bar. The catalyst is removed by filtration and monomer and solvent are evaporated off the product. The world-wide licensed Phillips-particle

form process is similar in solvent and suspended catalyst particles, though the catalyst particles undergo continuous fragmentation in the loop reactor system which each form polymer three orders of magnitude larger than the particle [134, 137]. There is also a gas phase process, widely known as the UNIPOL process, in which ethylene gas and a co-monomer such as 1-hexene pass through a fluidized bed of chromium supported catalyst around 100°C and 20 bar.

Due to its industrial importance, a large investigative effort has been undertaken on chromium supported catalysts since Phillips Petroleum discovered the process in 1951. Many questions still remain after 70+ years of research such as the oxidation state and structure of the active site and the polymerization mechanism. Interest in this dissertation runs parallel to the latter questions of structure and oxidation state of surface chromium.

Cr-Catalyst Preparation Method

It is important to note the method of chromium surface attachment as it differs from the method used in Chapter 5 of this work, potentially leading to different behavior of anchored/deposited chromium. Preparation of industrial catalysts involves impregnating support materials such as silicas, aluminas, and aluminosilicates in an aqueous or non-aqueous solution containing chromium oxides, sulfates, or acetates [134]. This may take place using techniques such as wetness impregnation or incipient wetness impregnation. Wetness impregnation involves submerging the support in solvent, and subsequently introduces the impregnating solution which diffuses from the bulk into support pores. Incipient wetness impregnation introduces impregnating solution equal to

the pore volume of the support which is drawn in by capillary action. The impregnated support is then dried around 120°C and calcined at temperatures ranging from 500-1000°C.

Surface Chromium Compound Formation

The development of surface chromium on catalyst supports has been observed to depend on the support material, temperature, and chromium loading. Related to temperature, behavior of chromium compound formation is dependent on the presence or absence of aqueous media. A hydrated surface will consist of ionic chromium compounds with the most prevalent being Cr^{6+} and Cr^{3+}. When hydrated trivalent chromium forms a complex ion with a maximum of six water ligands. Hexaaquachromium (III) ions are stable at low pH, but tends to hydrolyze to form hydroxide ligands as shown in Equation 4.1.

$$Cr(H_2O)_6^{3+} \rightleftarrows [Cr(H_2O)_5(OH)]^{2+} \rightleftarrows [Cr(H_2O)_n(OH)_m]^{3+-m} \rightleftarrows Cr(OH)_3 \quad (4.1)$$

At a pH range of 6-7, trivalent chromium is expected to primarily exist as a solid chromium hydroxide precipitate [138]. Hexavalent chromium, however, is stable over the entire pH range and is governed by pH dependent reactions as shown in Equations 4.2-4.5 [48, 139].

$$Cr(OH)_3 + 5OH^- \rightleftarrows CrO_4^{2-} + 4H_2O + 3e^- \quad (4.2)$$

$$2CrO_4^{2-} + 2H^+ \rightleftarrows Cr_2O_7^{2-} + H_2O \quad (4.3)$$

$$3Cr_2O_7^{2-} + 2H^+ \rightleftarrows 2Cr_3O_{10}^{2-} + H_2O \quad (4.4)$$

$$4Cr_3O_{10}^{2-} + 2H^+ \rightleftarrows 3Cr_4O_{13}^{2-} + H_2O \quad (4.5)$$

The hydroxyl populations of catalyst supports are also influenced by pH. Each catalyst support material will have an isoelectric point (IEP) which is the pH at which the surface of the oxide has zero net charge. If the solution pH is above the IEP of the catalyst support then the surface will have a net negative charge. If the solution pH is below the IEP then the opposite is true. This is shown in Figure 48 and governed by Equations 4.6-4.8.

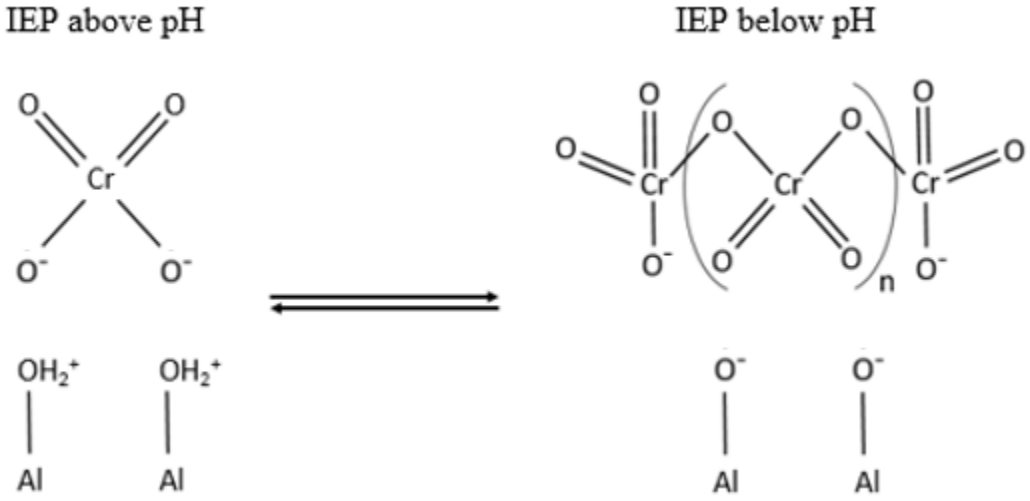


Figure 48 - Catalyst support hydroxyl groups influenced by IEP and pH.

$$M - OH_2^+ \rightleftharpoons M - OH + H_s^+ \quad (4.6)$$

$$M - OH \rightleftharpoons M - O^- + H_s^+ \quad (4.7)$$

$$H_s^+ \rightleftharpoons H^+ \quad (4.8)$$

H_s^+ – Surface proton

H^+ – Solution proton

When calcined, however, chromium species have been observed to interact with catalyst supports [140-146]. The focus here will be on alumina and silica supports, but others such as zirconia, titania, and niobia have also been examined [147-149]. As alumina and silica supports loaded with chromium are calcined, the chromium may undergo an esterification reaction with surface hydroxyl groups. Esterification is the production of an ester in which a hydroxyl group is replaced by an –O–R group, where "R" is an unspecified compound. The transition between hydrated and calcined conditions are shown in Figure 49.

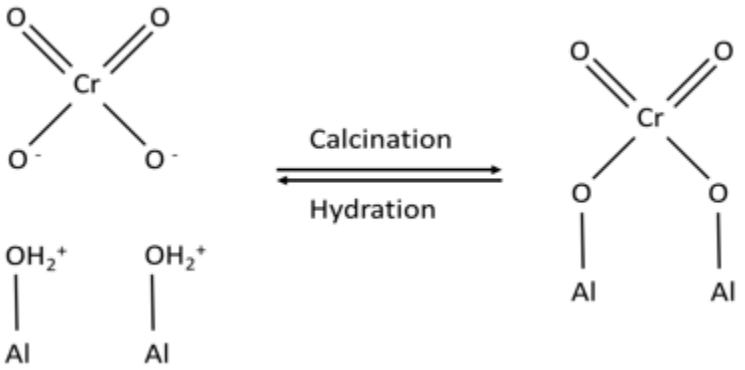


Figure 49 - Chromate under hydrated and calcined conditions on alumina catalyst support.

Evidence for the esterification reaction has been given in several forms. Infrared spectroscopy has been performed on silica supports which demonstrates the consumption of hydroxyl groups as chromium loading increases [147, 149, 150]. McDaniel [151] performed silanol (Si-OH) measurements by reacting methyl magnesium iodide with hydroxyl groups, where the evolution of methane gas was collected and related to a hydroxyl concentration. For temperatures ranging from 200-800°C, increasing chromium loading decreased surface hydroxyl populations. Silica exposed to CrO_2Cl_2 has also been

demonstrated to release HCl, attributed to gas interaction with hydroxyl groups [152]. Dry HCL exposure to these samples reproduced CrO_2Cl_2 vapor. Differential thermal analysis has also been performed in which an exothermal peak around 250°C was attributed to the esterification reaction [134, 143, 153]. The temperature at which esterification takes place has been reported over a range in literature from 150-300°C [48, 154, 155].

The stability of these anchored chromate species depends on factors such as support material, temperature, and chromium loading. Altering the chromium loading on the same material and at the same temperature has been observed to influence speciation. McDaniel [156] examined chromium supported on silica from 200-900°C in a variety of gas atmospheres for two hour exposures. Reflectance infrared spectroscopy was used to characterize Cr loading from 1-5 wt% in oxygen at 425, 650, and 870°C. As loading increased, the trivalent chromium band was observed to increase by an order of magnitude for all spectra. The gas atmosphere in which calcination took place was also observed to have an effect. Dry oxygen resulted in more stable chromium surface species than wet oxygen due to the greater tendency for anchored chromate to volatilize.

Vuurman et al. [147] examined both alumina and silica supports with chromium loading ranging from 0.5-9 wt% for alumina and 1-3 wt% for silica. Samples were calcined overnight in 500°C air. The study's authors report that chromia did not form on alumina up to 12 wt%, but formed at 3 wt% on silica. In a separate study [157] focused on alumina loaded with 1-30 wt% chromium exposed in air at 550°C for four hours, the study's authors found that increasing the weight percent resulted in the polymerization of

surface chromate. The observations were monochromate for 1 wt%, dichromate for 5-15 wt%, trichromate for 20-30 wt% with crystalline CrO_3 present at 30 wt%. Chromate on silica has also been shown to polymerize with increased loading, though at lower loading weight percent. Weckhuysen et al. [158], for example, showed the propensity of alumina supports to stabilize the monochromate species versus silica supports. Alumina and silica loaded with 0.2 wt% chromium and calcined at 550°C in air for six hours were reported to have chromate:dichromate ratios of ∞ and 0.56 for alumina and silica, respectively. The stability of chromate species on alumina is attributed to its larger monolayer coverage of 2.2 Cr/nm^2 for silica (amorphous) and about double for alumina (γ-Al_2O_3) [156, 159]. Silica has roughly double the surface area, but a hydroxyl population up to four times lower than that of alumina [152, 160-162] which may explain why alumina has double the surface coverage. Several other studies support the general trend of greater stability of surface chromate and hexavalent species generally on alumina versus silica [46, 48, 49, 163].

It may be noted that while stability on silica may be lesser, surface chromium species have been observed to be highly mobile on silica by McDaniel [164]. Chromia in a silica fixed bed was observed to spread down the bed and result in the oxidation of chromium when flowing oxygen at 800°C. This effect was also observed when mixing chromia on silica powder with four parts pure silica powder at 900°C. When mixed the surface chromium species largely re-oxidized based on the color change of green to yellow. Re-oxidation behavior is related to chromium loading and mobility. These observations show a silica surface may “unload” chromium through migration of surface

chromium species to “clean” surfaces thereby decreasing the chromium loading on the original surface and allowing for re-oxidation. To the best knowledge of the author of this dissertation similar mobility studies have not been pursued with other materials.

Alternative to varying the chromium loading, several studies have varied the temperature at a given chromium weight percent and material. Fouad et al. [165] exposed silica and alumina loaded with 10 mole% chromium precursor and exposed them in air at 300 or 600°C for five hours. Silica supports did not yield a defined diffraction pattern using XRD at 300°C but at 600°C crystalline Cr_2O_3 was observed. Alumina, however, only displayed weak diffraction features of chromia at 600°C. Surface chromium species were assigned as chromates from UV-Vis spectra analysis. Best et al. [140] reported a similar finding for 8 wt% silica exposed to temperatures ranging from 300-600°C. X-ray photoelectron spectroscopic analysis revealed a predominance of Cr^{6+} after the 300°C exposure but negligible Cr^{6+} at 500 and 600°C. As for alumina, Vuurman et al. [139] reported similar behavior to Fouad et al. [165] when exposing 5 wt% alumina in air from 250-1050°C for 16 hours. Surface chromium species were observed to be stabilized in the hexavalent form as chromates through Raman spectroscopy, with di/trichromates present at higher temperatures. Differences in behavior between alumina and silica are attributed to differences in hydroxyl groups on these materials. It has been mentioned that hydroxyl populations may be up to four times as numerous on certain phases of alumina, such as γ-Al_2O_3 when compared to amorphous silica. It may also be noted that Al^{3+} is a harder Lewis acid than Si^{4+}. Hard in this sense is in reference to the Hard Soft Acid Base (HSAB) theory. Hard acids are small, high oxidation state, and have low-polarizability

whereas hard bases are also small and weakly polarizable with a high electronegativity. Hard acid-hard base interactions have a large difference in electronegativity and therefore the bonding has a large ionic character. Oxygen is a hard base and given that aluminum is a harder acid than silicon, the bonding is predicted to be more stable between aluminum and oxygen compared to silicon and oxygen. This is important to note as ceramic surfaces undergo dehydroxylation as the temperature increases. The stronger bonding between oxygen and alumina may be seen by the greater retention of hydroxyl groups by alumina as the temperature increases. At 400°C amorphous silica has been reported to possess 2.35 OH/nm^2 [152] whereas γ-Al_2O_3 has been observed to possess 4-6 OH/nm^2 [160]. The general trends from this section may be briefly summarized as the following: alumina is able to stabilize Cr^{6+} at higher temperatures than silica whereas silica promotes chromia formation at lower temperatures than alumina.

Consensus and Contradiction

There are several areas of consensus in the catalyst support literature. Chromium anchors to hydroxyl groups with more basic hydroxyl groups being consumed before less basic sites [46, 48, 147, 149, 156, 166]. Chromium loading, temperature, and the support material have been observed to influence chromium compound speciation [157, 158, 165, 167-169]. Chromate is formed at lower temperature and chromia is favored at higher temperature. Alumina is better capable of stabilizing chromate species for higher loadings and temperatures than silica. It may also be noted that certain colors have been attributed to chromium oxidation states and/or compounds. Blue has been observed for Cr^{2+}, green for Cr^{3+}, and black-brown for Cr^{4+} [48]. Hexavalent chromium has been observed in a

range of colors, so colors are attributed to specific hexavalent compounds as opposed to the general oxidation state. Yellow has been reported for chromate, orange for dichromate, red for trichromate, and red-brown for chromium trioxide [45, 48, 170].

There is not consensus regarding the oxidation state of certain chromium compounds. Chromium compounds with oxidation states 2-6, such as chromates, CrO_3, Cr_2O_3, CrO_2, Cr_2O_5, Cr_3O_8, and CrO have been reported in literature [48, 139, 140, 143, 155, 167, 171, 172]. Chromium (II) oxide has only been observed under reducing conditions [49, 143] and is therefore not considered relevant for this study in oxidizing conditions. All of the other chromium compounds listed have been observed in oxidizing conditions. While repeatedly observed, the oxidation state(s) of Cr_2O_5 and Cr_3O_8 are under contention. Hewston and Chamberland [172] noted Cr_2O_5 may exist as Cr^{5+}, Cr^{3+}/Cr^{6+}, or Cr^{4+}/Cr^{6+}, whereas Cr_3O_8 may exist as either mixed valence variant. To determine which are correct, the study's authors prepared Cr_2O_5 and Cr_3O_8 from a CrO_3 precursor. The phases were confirmed using XRD and the stoichiometry through thermal gravimetric analysis. Infrared spectroscopy revealed the two compounds have similar spectra with regions resembling regions from chromate, dichromate, and CrO_6 octahedral groups. Electron paramagnetic resonance spectra supported the presence of Cr^{3+} in Cr_2O_5 and Cr_3O_8 and magnetic susceptibility behavior was consistent with the presence of Cr^{3+}/Cr^{6+}. X-ray photoelectron spectroscopy performed by Tsutsumi et al. [173] supports this conclusion. Spectra of $K_2Cr_2O_7$, Cr_2O_5, Cr_3O_8, and Cr_2O_3 were compared and the spectra for Cr_2O_5 and Cr_3O_8 were nearly indistinguishable. Both appeared as a combination the hexavalent compound ($K_2Cr_2O_7$) and the trivalent compound (Cr_2O_3)

spectra. Maslar et al. [174] also attributed these compounds as mixed valence Cr^{3+}/Cr^{6+}, instead using Raman spectroscopy.

Fouad et al. [165] instead contend that Cr_2O_5 is a Cr^{4+}/Cr^{6+} mixed valence compound. Chromium trioxide supported on alumina and silica (10 mole% loading) was observed to from Cr_2O_5 based on XRD analysis. The study's authors appear to put forward the Cr^{4+}/Cr^{6+} mixed valence state of Cr_2O_5 as supposition. The study's authors appear to reason that as Cr_2O_5 is an intermediate compound between CrO_3 and CrO_2, one may describe Cr_2O_5 as a combination of $CrO_3 \cdot CrO_2$. The author is not aware of any additional studies claiming Cr_2O_5 as a Cr^{4+}/Cr^{6+} mixed valence species.

Claims of Cr_2O_5 as a Cr^{5+} compound are more numerous in literature. Liu et al. [155] inferred the presence of Cr_2O_5 with a Cr $2p_{3/2}$ binding energy of 577.6 eV. The study's authors reported chromium calcined on silica over a range of temperatures, with the precursor being Cr^{3+}, and the 120°C exposure in air converting all of the precursor to Cr^{6+} with a binding energy of 579.1 eV. At 200°C, the spectrum was claimed to consist of the Cr^{6+} species at 579.8 eV and the Cr^{5+} component (attributed to Cr_2O_5) with a binding energy of 577.6 eV. While the study's authors put forward an oxidation state of Cr^{5+}, the evidence presented does not preclude a mixed valence Cr^{3+}/Cr^{6+} species in place of the Cr^{5+} assignment. Okamoto et al. [175] claimed to observe Cr^{5+} in reducing conditions and based the assignment of Cr^{5+} largely on spin orbit splitting values (ΔE). The rational being that ΔE tends to increase with decreasing oxidation number due to the exchange interaction of 2p and unpaired 3d electrons [176, 177]. Contributions assigned as Cr^{5+} were observed to have ΔE values near hexavalent, but binding energies nearer to

trivalent. This approach appears to be of questionable accuracy for a couple reasons. This method examines about an electron volt range (≈9-9.9 eV ΔE) with 0.1 eV increments for spectra with large (estimated 3-6 eV) full width at half maximum (FWHM) single fit peaks which are often asymmetric. Approximating ΔE in this way will introduce error on the order of tenths of an electron volt. It may also be noted that no argument presented necessitates the presence of Cr^{5+}. For example, there are several exposures which yielded a Cr $2p_{3/2}$ binding energy of 577.8 eV, but a range of ΔE values. A ΔE of 9.1 eV is assigned as 5+, 9.4 eV as 5+, (3+) where parenthesis indicate minor contribution, and 9.6 eV as 3+, (5+). The study's authors note that the ΔE appears largely unaffected by an oxidation state change of one for Cr^{6+} to Cr^{5+} and Cr^{4+} to Cr^{3+}. As the binding energy for the assignments listed above didn't change, by this line of argumentation there's no reason why an assignment of 5+/3+ couldn't instead be 6+/4+ or 6+/3+.

Electron spin resonance spectroscopy has also been used by Weckhuysen et al. [49] and Poole et al. [178] which claims the presence of Cr^{5+} calcined chromium supports. Both note a γ-signal attributed to Cr^{5+}, but neither assigns this to Cr_2O_5. To the contrary, Weckhuysen et al. [49] describe this signal as isolated mononuclear Cr^{5+}. Kazanski and Turkevich [179] also attribute this signal to isolated mononuclear Cr^{5+}, proposing that chromium replaces a silicon atom to form a distorted tetrahedron with three single bonds to oxygen and one double bond to oxygen. Given these arguments, Cr_2O_5 and Cr_3O_8 will be inferred as mixed valence Cr^{3+}/Cr^{6+} species in this work.

In summary, chromium has been observed to exist in a variety of compounds (M-CrO_4, Cr_2O_3, CrO_2, Cr_2O_5, Cr_3O_8, CrO, etc.) and oxidation states (2-6) on ceramic

surfaces. Which species form depends on the material, temperature, and amount of chromium loaded on the ceramic surface. These findings were made by calcining a chromium oxide catalyst support which was prepared in a chromium solution and dried at a lower temperature to control for chromium weight percent loaded. While directly analogous to industrial catalysts, these conditions differ from the focus of this work. Volatile chromium species reactively condensing onto surfaces free of chromium, and at temperature, was observed to yield similar yet importantly differing behavior than controlled loading of chromium solutions at lower temperature. Deposition at high temperature may be largely uninhibited or precluded, depending on the ceramic surface.

CHAPTER FIVE

INVESTIGATION OF SURFACE INTERACTIONS BETWEEN VOLATILE CHROMIUM SPECIES AND CERAMICS

Content in Chapter Five

Chapter Five contains two first author publications from the author of this dissertation. The first paper is titled XPS Characterization of Aluminosilicate Fibers Post Interaction with Chromium Oxyhydroxide at 100-230°C and was published in The Journal of the Electrochemical Society in July 2018 [2]. Co-authors in the Department of Chemical and Biological Engineering at Montana State University include Dr. Paul Gannon, Nolan Swain, and Ryan Mason. Co-authors in the Department of Mechanical Engineering at Montana State University include Emily Remington and Spencer Dansereau. The second paper is titled Surface Interactions between Volatile Chromium Species and Ceramics and is under review for publication in Surface and Interface Analysis [3]. Co-authors in the Department of Chemical and Biological Engineering at Montana State University include Dr. Paul Gannon, Nolan Swain, and Ryan Mason. Co-authors in the Department of Mechanical Engineering at Montana State University include Emily Remington and Spencer Dansereau.

Interactions on Aluminosilicate Fibers

The following data is taken from XPS Characterization of Aluminosilicate Fibers Post Interaction with Chromium Oxyhydroxide at 100-230°C which was published in

The Journal of the Electrochemical Society in July 2018 [2]. The findings were also presented in poster format at a Gordon Research Conference/Seminar and at the Sixth International School for Materials for Energy and Sustainability in July 2017. In this work aluminosilicate fibers were exposed to volatile chromium species for 150 hours at 100-230°C and the resulting condensed species were correlated with different discolored regions on exposed fibers. X-ray photoelectron spectroscopic analysis revealed Cr(VI) and Cr(III) content varied by region in accordance with compounds inferred to comprise each region.

Methods

Sheets of FSS T409 (see Table 1 for composition) were cut lengthwise using foot shears into strips of approximate dimensions 125 mm × 14 mm × 1.48 mm. Four strips of T409 were used in each experiment which were each measured, massed, and stamped for identification pre-exposure. These strips were used to generate volatile chromium species to contaminate aluminosilicate fibers of approximate mass 2 g which were placed downstream of the chromium source. The strips were placed in a quartz crucible which was housed in the center of a 30 mm OD quartz tube as illustrated in Figure 50. The quartz tube was placed in a GSL-1100x tube furnace and flanges sealed with O-rings were used to connect the quartz tube to inlet and outlet tubing. The inlet to the furnace was supplied using house air and controlled by an Omega FL-3613 G rotameter to establish a flow rate of 900 sccm. A three-way valve was used to direct flow to a 1 L glass bubbler which was fitted with a frit of porosity rating P1. The bubbler was filled with water and heated to approximately 55°C, yielding an estimated P_{H20} of ~0.16 bar.

The inlet gas/vapor interacts with stainless steel strips at 700°C and passes through aluminosilicate fibers outside of the furnace. Condensation zones of 100–230°C were observed on the fibers using an Amprobe IR608A infrared thermometer. After passing through the fibers, effluent was initially routed into a 500 mL Erlenmeyer flask to condense water vapor. Condensate was assumed to contain negligible chromium, in line with previous unpublished results. The effluent is then directed to a fume hood for venting. See Figure 50 for clarification.

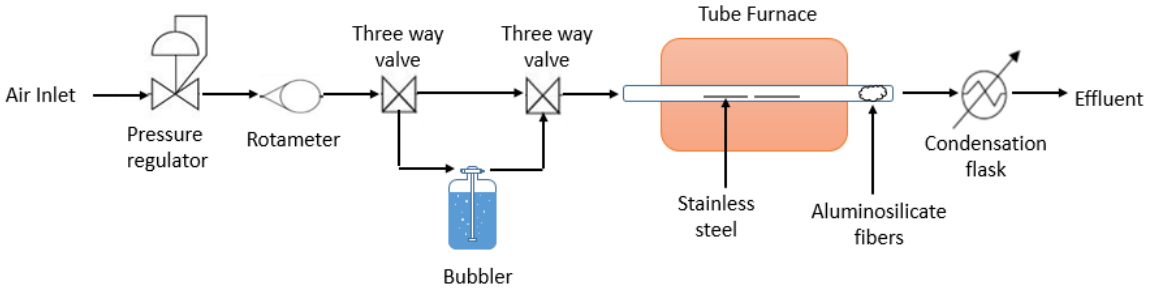


Figure 50 – Schematic illustration of the experimental setup in XPS Characterization of Aluminosilicate Fibers Post Interaction with Chromium Oxyhydroxide at 100-230°C [2].

The furnace ramp rate was 30°C/min and exposure time at 700°C was 150 hours. After the exposure period elapsed, power to the furnace was discontinued and dry air was used during cool down. Upon cooling to room temperature, steel strips and fiber were re-massed. A Physical Electronics 5600 X-ray Photoelectron Spectrometer (XPS) system was used to characterize discolored regions on aluminosilicate fibers. To compensate for the insulating nature of these samples, a stainless-steel mesh screen was placed over fiber samples, and an electron flood gun was used. The stainless steel mesh screen is attached to a conductive metal frame, which is grounded to the sample mount. Emission of photoelectrons from insulating samples may lead to differential charging due to a buildup

of positive charges on the surface. Using a stainless steel mesh screen, in addition to a flood gun supplying low energy electrons, allows for a more uniform electric potential at the sample surface, and swift supply of electrons to areas beginning to accumulate positive charges. It will be noted that chromium signal from the mesh was precluded, as the mesh consists of 2 mm × 2 mm square sizes, with an analysis area of 1 mm × 1 mm which is marked on the sample image screen for easy targeting. The reliability of this targeting is checked by Image and Chemical Analysis Laboratory staff at Montana State University. Spectra were adjusted as necessary by setting Al 2p to 74.4 eV. A pass energy of 46.95 eV was used with 0.2 eV/step and 40 ms/step, and the collection area was set to a +/−7° solid angle.

It will be noted here that some compounds to be examined, such as Cr_2O_3, may have a finely structured multiplet splitting pattern [180, 181]. These structures are uncovered through XPS examination of a high purity compound. In the analysis of surfaces with mixtures of compounds which follows, these structures would quickly become numerous and unwieldy, and so broad Gaussian-Lorenzian (GL) peak fits are used instead. It may be imagined that convolution of the finely structured multiplet splitting structures would result in the displayed broad GL peaks. This is demonstrated visually in Figure 51, where work from Biesinger et al. [181] (left), and Pradier et al. [169] (right) is compared. The left spectrum is high purity Cr_2O_3, whereas the spectrum on the right consists of a mixture of chromium containing oxides. The boxed broad GL peak in the right spectrum can be imagined to be a convolution of the multiplet splitting structure of the high purity Cr_2O_3 spectrum on the left.

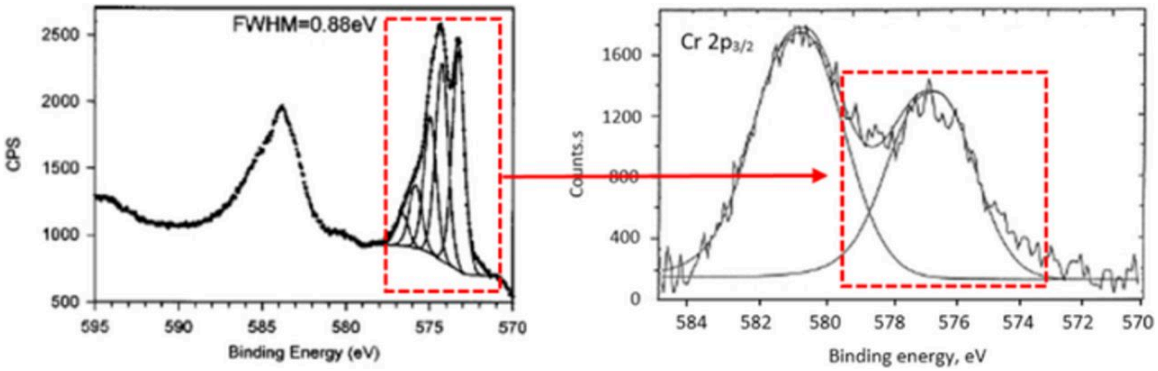


Figure 51 - Comparison of high purity Cr2O3 multiplet spliting structure (left) [181] with broad GL peak fit representation for mixed Cr oxides (right) [169].

Observations and Interpretations

Aluminosilicate fibers were observed to discolor upon exposure to volatile chromium species for 150 hours at 100-230°C. Figure 52 displays a color gradient of what appears to be dark brown to light brown (right to left) corresponding with high to low temperature.

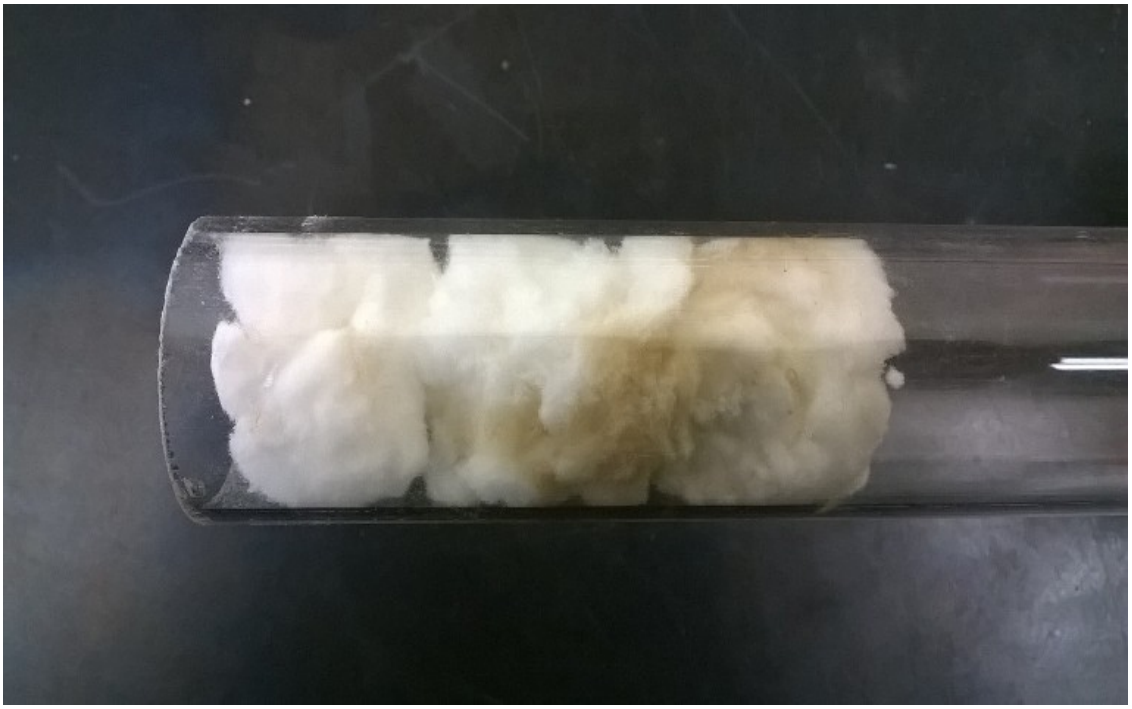


Figure 52 - Representative staining observed on aluminosilicate fibers post exposure.

When the fiber sample displayed in Figure 52 was broken up, three distinct colors were observed: brown, green, and yellow. These discolorations are displayed in Figure 53.

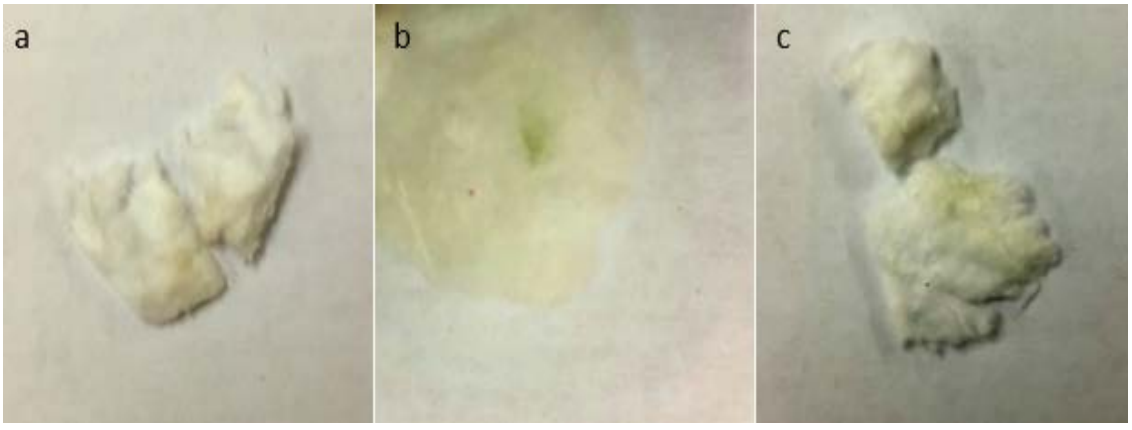


Figure 53 - Stained regions on aluminosilicate fibers examined using XPS. From left to right: brown (a), green (b), and yellow (c).

As mentioned in Chapter four, certain colors have been attributed to different chromium oxidation states and compounds. Brown and yellow have been attributed to the

presence of hexavalent chromium and green to the presence of trivalent chromium [45, 48, 170]. While this visual inspection may give some insight into chromium oxidation state and speciation on a given surface, the human eye is inadequate for discerning subtle mixtures of color. For example discerning “pure” brown from “mixed” brown. It is therefore reasonable to expect to see a mixture of compounds in all spectra performed.

Figures 54-56 are Cr $2p_{3/2}$ energy windows ranging from about 572-582 eV for brown, green, and yellow staining, respectively. Tables 3-5 give peak information for Figures 54-56, respectively.

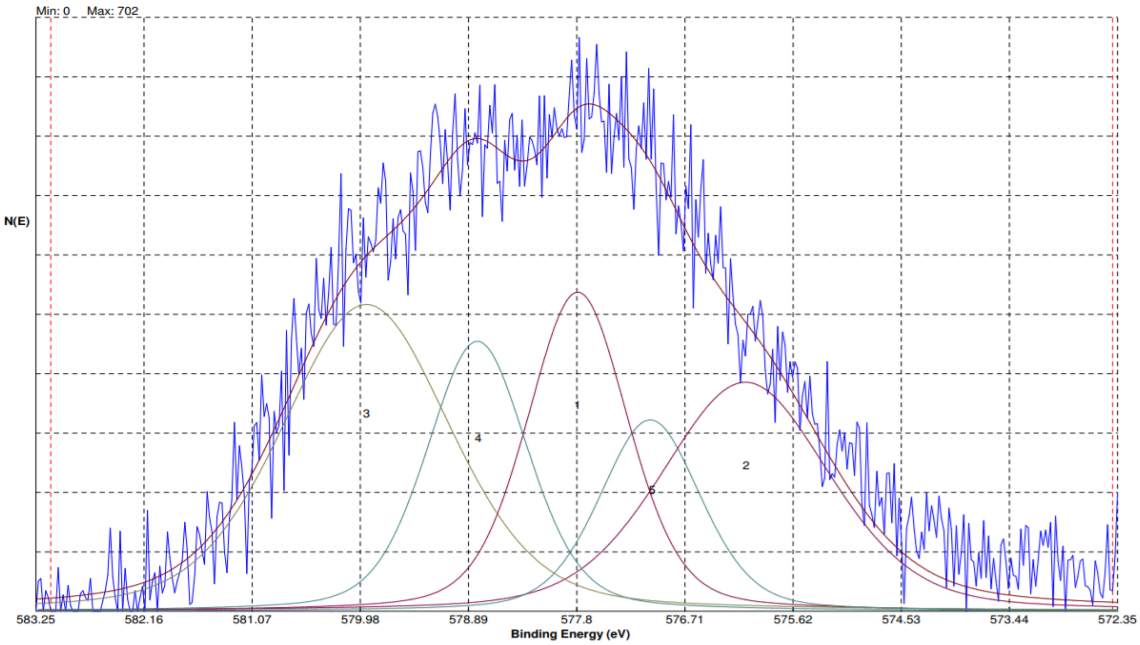


Figure 54 - Cr $2p_{3/2}$ energy window for brown staining on aluminosilicate fibers. Peaks 1, 2, 4, and 5 are trivalent multiplet-split components. Peak 3 is the hexavalent component.

Table 3 – Peak information for brown staining on aluminosilicate fibers (Figure 54). Secondary inferred compounds are compounds which are believed to contribute to some extent to the peak signal, but to a lesser degree than the primary inferred compound.

Peak	Area %	Peak Position	Oxidation State	Primary Inferred Compound(s)	Secondary Inferred Compound(s)	Intensity	FWHM	% Gauss
1	19.1	577.79	+3	Cr_2O_5 and/or Cr_3O_8	-	390	1.2	70
2	22.8	576.10	+3	Cr_2O_3	-	280	2	70
3	30.6	579.92	+6	CrO_3	Chromate species, Cr_2O_5 and/or Cr_3O_8	375	2	70
4	16.1	578.80	+3	Cr_2O_5 and/or Cr_3O_8	-	330	1.2	70
5	11.4	577.06	+3	Cr_2O_5 and/or Cr_3O_8	-	234	1.2	70

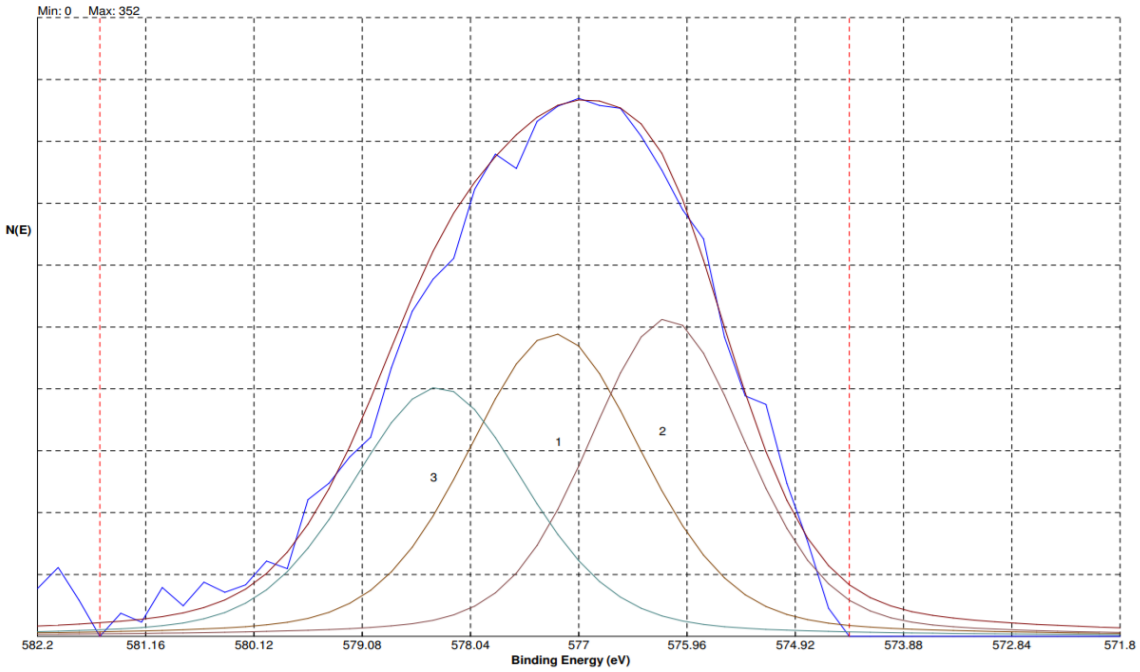


Figure 55 - Cr 2p3/2 energy window for green staining on aluminosilicate fibers. Peaks 1 and 2 are trivalent multiplet-split components. Peak 3 is the hexavalent component.

Table 4 - Peak information for green staining on aluminosilicate fibers (Figure 55). Secondary inferred compounds are compounds which are believed to contribute to some extent to the peak signal, but to a lesser degree than the primary inferred compound.

Peak	Area %	Peak Position	Oxidation State	Primary Inferred Compound(s)	Secondary Inferred Compound(s)	Intensity	FWHM	% Gauss
1	40.4	577.64	+3	Cr_2O_5 and/or Cr_3O_8	-	280	2	90
2	40.9	576.30	+3	Cr_2O_3	-	260	2	70
3	18.7	579.00	+6	Chromate species	CrO_3, Cr_2O_5 and/or Cr_3O_8	130	2	90

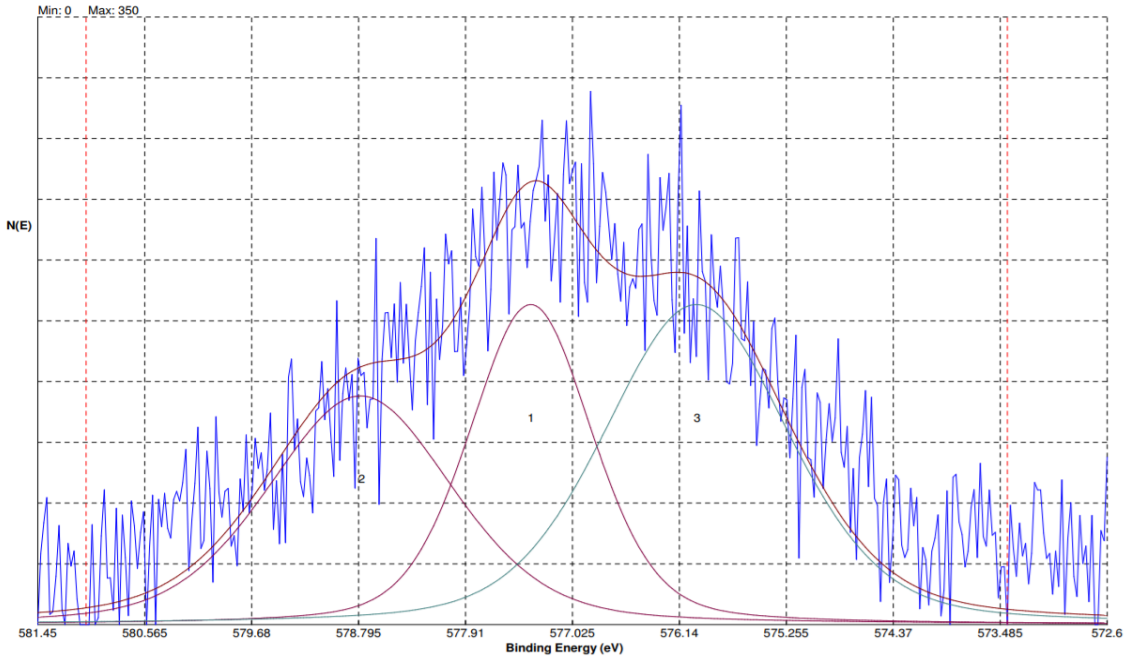


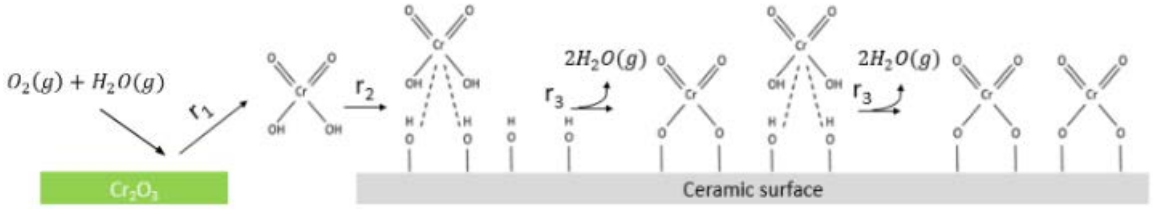
Figure 56 - Cr 2p3/2 energy window for yellow staining on aluminosilicate fibers. Peaks 1 and 3 are trivalent multiplet-split components. Peak 2 is the hexavalent component.

Table 5 - Peak information for yellow staining on aluminosilicate fibers (Figure 56). Secondary inferred compounds are compounds which are believed to contribute to some extent to the peak signal, but to a lesser degree than the primary inferred compound.

Peak	Area %	Peak Position	Oxidation State	Primary Inferred Compound(s)	Secondary Inferred Compound(s)	Intensity	FWHM	% Gauss
1	48.5	577.25	+3	Cr_2O_5 and/or Cr_3O_8	-	197	1.2	90
2	26.9	579.10	+6	Chromate species	CrO_3, Cr_2O_5 and/or Cr_3O_8	100	2	70
3	24.6	576.00	+3	Cr_2O_3	-	100	2	90

Prior to providing spectra interpretation, a sequence of events will be proposed based on the literature review in the previous section to better understand why regions may be differently discolored. This sequence of events is illustrated below in Figures 57-59. Chromium oxyhydroxide, the dominant volatile chromium product formed in air and water vapor, comes into contact with aluminosilicate fiber surfaces over 100–230°C. At this temperature range, the volatile chromium species is likely physisorbed to the surface. Physisorption is likely as the temperature is near/below the condensation point of the gas, and since this deposition has been precluded in literature if the temperature rises too far above the upper limit on the range [31]. Physisorbed $CrO_2(OH)_2$ may dehydrate to form CrO_3. Chromate species may form from CrO_3 through an esterification reaction with the surface [149-155]. Hydroxyl groups act as anchoring points which allow for stabilization and dispersion of hexavalent chromate [46, 48, 147, 149, 156, 166]. Up to this point, monolayer coverage of the surface has not been achieved, as an insufficient amount of

chromium has been loaded. The color of the material loaded with these well dispersed chromate species would appear to be yellow [46].



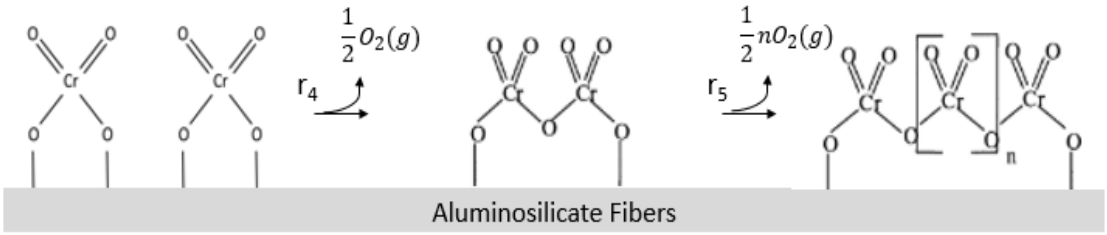
$$r_1: \frac{1}{2}Cr_2O_3(s) + \frac{3}{4}O_2(g) + H_2O(g) \rightleftharpoons CrO_2(OH)_2(g)$$

$$r_2: CrO_2(OH)_2(g) \rightleftharpoons CrO_2(OH)_2(a)$$

$$r_3: CrO_2(OH)_2(a) + 2M - OH(s) \rightleftharpoons M_2CrO_4(s) + 2H_2O(g)$$

Figure 57 - Sequence of steps illustrating the formation of chromate species on aluminosilicate fibers. Volatile chromium species $CrO_2(OH)_2$ is generated from T409 (r_1), and subsequently undergoes physisorption (r_2), dehydration and esterification (r_3) to yield chromate species. Formation of these species would lend the fibers a yellow color.

As chromium loading increases, hydroxyl groups diminish and chromate species may form O-Cr-O bonds resulting in polychromated species, and eventually CrO_3 [153, 182]. The agglomerated chromate species are minimally anchored to the surface and therefore are minimally stabilized. At this stage the color would appear to be brown [157].

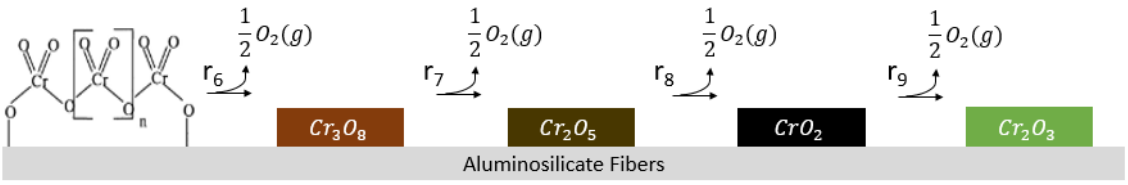


r_4: $2M_2CrO_4(s) \rightleftharpoons \mathrm{M_2Cr_2O_7(s)} + \frac{1}{2}\mathrm{O_2(g)}$

$r_5 \rightarrow CrO_3(s)\ for\ large\ values\ of\ n$

Figure 58 - Sequence of steps illustrating the formation of CrO_3 on aluminosilicate fibers. Monochromate species form O-Cr-O bonds resulting in polychromated species (r_4, r_5), and eventually CrO_3. Formation of this species would lend the fibers a brown color. Middle and right illustration taken from Liu et al. [182]. Note that "n" represents an integer value.

Thermal decomposition of CrO_3 would ensue. Oxygen is lost over time which may result in the formation of Cr_3O_8, then Cr_2O_5, followed by CrO_2, and lastly Cr_2O_3. At this stage the color would appear to be green [178]. Decomposition of CrO_3 to Cr_2O_3 would likely leave remaining surface chromate species as the primary hexavalent species. Figures 54-56 will now be discussed given this proposed sequence of events.



$$r_6: 3CrO_3(s) \rightleftharpoons Cr_3O_8(s) + \frac{1}{2}O_2(g)$$

$$r_7: Cr_3O_8(s) \rightleftharpoons \frac{3}{2}Cr_2O_5(s) + \frac{1}{2}O_2(g)$$

$$r_8: Cr_2O_5(s) \rightleftharpoons 2CrO_2(s) + \frac{1}{2}O_2(g)$$

$$r_9: 2CrO_2(s) \rightleftharpoons Cr_2O_3(s) + \frac{1}{2}O_2(g)$$

Figure 59 - Sequence of steps illustrating the formation of Cr_2O_3 on aluminosilicate fibers. Thermal decomposition of CrO_3 results in loss of oxygen over time as shown in r_6, r_7, r_8, and r_9. Deoxygenation of surface chromium species gives rise to Cr_2O_3. Formation of this species would lend the fibers a green color. Left illustration taken from Liu et al. [182].

In Figures 54-56 and subsequent spectra to be presented in the following section, the highest binding energy peak was assigned as hexavalent chromium. The greatest proportion of hexavalent chromium was observed in the brown staining, followed by the yellow staining, with the least observed on the green staining. This aligns with what one might expect based on the colors. Literature reports a range of binding energies for chromate and chromium trioxide, from 578.3-581.1 eV [155, 169, 180, 181, 183-185] with some studies reporting chromate higher and others reporting chromium trioxide higher. These overlapping binding energies make it impossible to differentiate which compound is present based on binding energy alone, but on the basis of color one will expect yellow staining to be associated more with hexavalent monochromate and brown staining with hexavalent chromium trioxide.

The lowest binding energy peak has been assigned as Cr^{3+}. This peak is inferred to represent a contribution from chromia given the proposed sequence. The binding energy range of 576-576.3 eV matches well for literature reporting of Cr_2O_3 [139, 183, 185]. It is possible to propose this peak contribution represents Cr^{4+} likely in the form of CrO_2 given the proposed sequence of events. The Cr $2p_{3/2}$ peak for CrO_2 is anticipated to appear around 575.2 eV [184, 186]. While this value may seem to be in contradiction with the chemical shift theory, CrO_2 has been observed to have a lower binding energy than Cr^{3+} species repeatedly [177, 169, 184, 186]. This peak does not appear to be present with appreciable intensity for any of the stains, but it is possible that the binding energy of CrO_2 may be inflated due to dehydroxylation of silica/alumina surfaces as the temperature increases. As more hydroxyl sites are lost, the electron density of the surface diminishes. This decreased electron density likely results in a decrease in electron density of anchored chromium species, thereby increasing the binding energy. The impact of this effect and the influence of temperature has been reported by Liu et al. [155] for hexavalent species from 100–800°C, over which the binding energy rises approximately 3 eV. The effect of this potential confound may be tested by examining the binding energy of Cr^{6+}. The binding energy of Cr^{6+} presented in this study ranges from 579–579.92 eV. These values are well within known norms for the binding energy of Cr^{6+} species [158, 180, 181, 183]. It seems that for these conditions, the extent of dehydroxylation was minimal. This in turn means the peaks observed to range from 576–576.3 eV (lowest binding energy peak in each spectrum) are not due to an inflated Cr^{4+} signal, but rather from Cr^{3+}.

Ruling out an inflated signal from Cr^{4+} as the lowest binding energy peaks holds implications for the middle peaks in the spectra. If the lowest binding energy peaks were Cr^{4+} then the middle peaks would be reasonable assigned as an inflated Cr^{3+} signal also due to the dehydroxylation effect. Instead the lowest were assigned as Cr^{3+} and inferred to represent Cr_2O_3 with the highest binding energy peaks assigned to Cr^{6+}. Peaks in the Cr_2O_3 multiplet splitting structure have been observed to span approximately 3 eV, but the two major peaks in the structure are located near 576–577 eV [180, 181]. Given these facts, the presence of a compound other than Cr_2O_3 or Cr^{6+} appears necessary. All of the spectra have significant peak contributions at binding energies exceeding the dominant multiplet components of Cr_2O_3. It is in this way that one may infer the middle peak(s) are attributable to Cr_2O_5 and/or Cr_3O_8, as these compounds are commonly observed in literature under these conditions [48, 172, 174, 187, 188] and have been observed to possess Cr^{3+} peak contributions near those reported here [173] . Alternatively, one might assign the middle peak as chromium hydroxide since the binding energy matches literature reporting [181] and it is a possible reaction product from chromate and water. To the knowledge of the authors, however, no publications have claimed to observe chromium hydroxide in similar conditions. Therefore, it seems more reasonable to assign this middle peak to the Cr^{3+} contribution of mixed valence Cr^{3+}/Cr^{6+} species.

Interactions on Alumina, Quartz Wool, and Mica

The following data was taken from Investigation of Surface Interactions between Volatile Chromium Species and Ceramics. This work was submitted to Surface and

Interface Analysis in July 2018 and is currently under review [3]. The data was also presented in oral format at the 233rd ECS Conference in May 2018. This study expands on XPS Characterization of Aluminosilicate Fibers Post Interaction with Chromium Oxyhydroxide at 100-230°C by exposing alumina, quartz wool, and mica to humidified air ranging from 150-900°C for 24 and 100 hour exposures with subsequent XPS analysis. The influence of temperature, material, and exposure time was observed to be determinative of surface chromium speciation and the extent of chromium deposition.

Methods

The experimental setup used in this study is similar to the previous study, but differs in the chromium source, exposed ceramics, temperatures, and times. Chromia powder of purity ≥98% was used to generate volatile chromium species to contaminate quartz wool, mica wafers ($KAl_3Si_3O_{10}(OH)_2$), and alumina (99.69% purity α-Al_2O_3) wafers. In each experiment, ceramic samples were placed both in the center of the furnace, designated as the “hot zone”, and just outside the furnace, designated as the “cold zone”. Three furnace temperatures were used: 500, 700, and 900°C. This resulted in three hot zone exposures at temperature (500, 700, and 900°C) and three corresponding cold zone temperatures of 250-300°C, 200-250°C, and 150-200°C, respectively. The cold zone temperature ranges were determined using an Amprobe IR608A infrared thermometer. The same exposure gas, furnace system, and method of analysis as the previous study was used in this study. Figure 60 displays the change in chromium source and clarification of sample positioning.

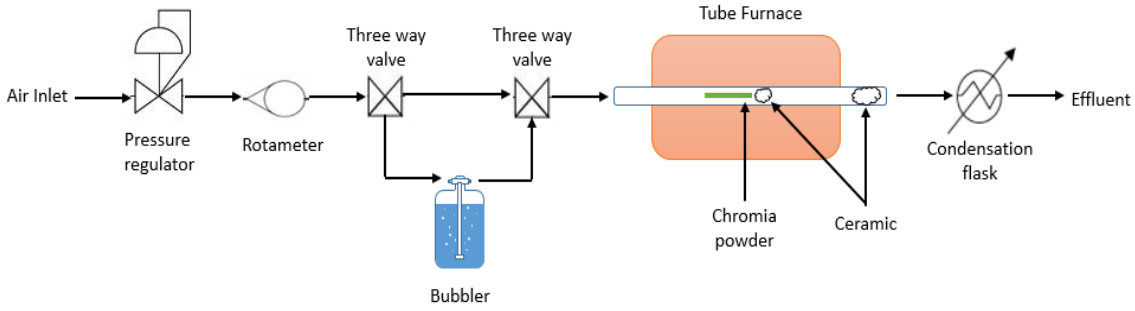


Figure 60 - Schematic illustration of the experimental system used in Investigation of Surface Interactions between Volatile Chromium Species and Ceramics.

Observations and Interpretations

Interpretation of spectra is in line with the previous study interpretations and is summarized in Figure 61. Table 6 is a record of which exposures possessed detectable levels of chromium using XPS (threshold ≈ 0.1 at%).

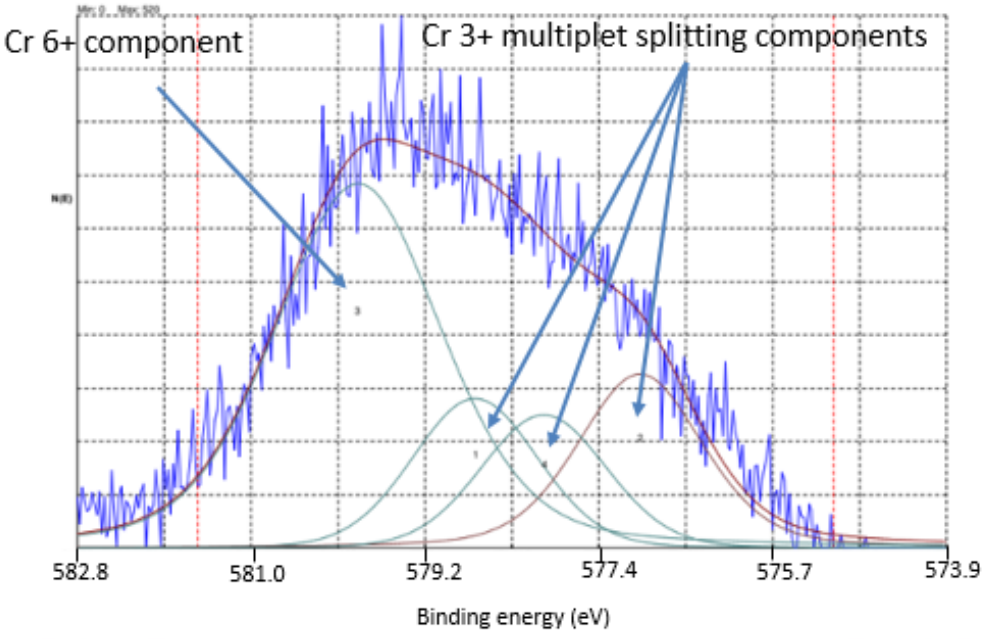


Figure 61 - Interpretation of spectra, with the highest binding energy peak representing Cr 6+, the lowest binding energy peak inferred to represent chromia, and the middle two peaks inferred to represent the trivalent multiplet splitting components of Cr 6+/Cr 3+ mixed valence species.

Table 6 - Record of which exposed samples possessed dectectable levels of chromium using XPS, where an "x" denotes Cr detection, a "-" represents a sample which has not been characterized, and a blank represents undetectable levels of Cr.

	Alumina – Top	Alumina – Bottom	Mica – Top	Mica – Bottom	Quartz Wool
900°C, 100 hr	X	X	X		
900°C, 24 hr	X		X	X	
700°C, 100 hr	X	X	X		
700°C, 24 hr	X				
500°C, 100 hr	X	X			
500°C, 24 hr	X	-			
250-300°C, 100 hr	X	X	X		X
250-300°C, 24 hr	X	X	X		X
200-250°C, 100 hr	X	X	X	X	X
200-250°C, 24 hr	X	X	X	X	X
150-200°C, 100 hr	X	X	X	X	
150-200°C, 24 hr	X	-			

Examining Table 6, different behavior for each material is notable. Alumina appears to collect more chromium than mica, which appears to collect more chromium than quartz wool. Additionally, the bottom side of the wafers appear to collect less chromium than the top sides. This is the only trend which the authors could distinguish for chromium collection dependence based on which wafer side was used. It will be noted here, as was mentioned in the limitations section, that some anomalous behavior was observed for chromium deposition depending on flow conditions. For both the 100 and 24 hour 250-300°C alumina exposures, green staining was observed on the bottom side, whereas brown/yellow staining was observed on the top side. Based on the experimental set up, the top side of the wafer has greater access to flow. Greater access to flow would suggest more Cr available to deposit, and based on the proposed mechanism one might expect green on top and brown on bottom, but the opposite was observed. None of the other wafers displayed this behavior and so, for this study at least, the observations were taken as anomalous. All subsequent discussion of wafers will be in regard to the top side.

Lastly, whereas alumina collects sufficient chromium at all temperatures and exposure times, mica and quartz wool do not collect enough chromium to meet the detection limit in 500°C hot and cold zones. Quartz wool shows negligible collection for both the hot and cold zones at 500°C, for both exposure times, whereas mica only differs in detectable chromium for the 150-200°C, 100 hour exposure. This may, in part, be attributable to the fact that the vapor pressure of chromium oxyhydroxide varies with temperature, with 500°C having a partial pressure three orders of magnitude less than 900°C according to thermodynamic modeling of similar conditions [19, 32]. This explanation is not sufficient, however, as it can be seen from Table 6 that quartz wool exposed to volatile chromium at the 900°C vapor pressure collects less Cr than alumina at 500°C vapor pressure. This suggests an effect of "substrate material" on which Cr-vapor condenses. The influence of material, in addition to time, and temperature on chromium loading will now be explored in more detail.

Many of the same colors as were noted in the previous study appear on quartz wool and alumina wafers. Figures 62 and 63 display yellow, brown, and green discoloration present on quartz wool and alumina wafers. These colors were not observed on mica (Figure 64) which remained transparent below 700°C but became opaque, expanded in thickness, and given a silver luster above this temperature. This is likely due to a dehydroxylation effect in which hydroxyl groups interact to form water, which then generate sufficient pressure to cause delamination of muscovite sheets, subsequently accelerating water loss and resulting in the formation of muscovite dehydroxylate [189].



Figure 62 - Representative discoloration on quartz wool after exposures. From left to right: non-exposed quartz wool, yellow, light brown, and dark brown.

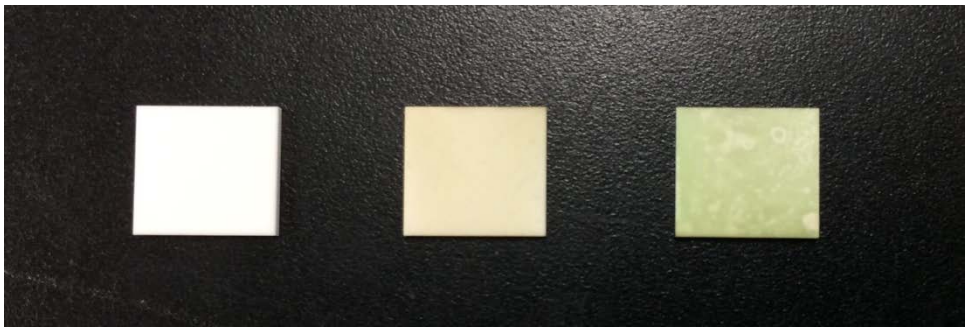


Figure 63 - Representative discoloration on alumina after exposures. From left to right: non-exposed alumina, brown, and green.



Figure 64 - Representative mica samples and thicknesses post exposure. From left to right: non-exposed mica, 150-500°C mica, and 700-900°C mica with top view (a) and side view (b).

In the previous section it was remarked that green is attributable to trivalent chromium species whereas brown and yellow are ascribed to hexavalent species. Compounds assigned to these colors in the last study included CrO_3 (brown staining), chromate (yellow staining), and Cr_2O_3 (green staining).

Examination of exposed quartz wool, mica, and alumina XPS spectra in Figures 65-68 reveals several general trends. Materials in hot regions collected less chromium than those in cold regions, and generally did not show a tendency to form one oxidation state over another at long times (Figures 66e,f and 68). Concerning hot regions, aluminum containing ceramics were observed to collect more chromium than silicon containing ceramics. This can be seen as silica (quartz wool) did not possess detectable levels of chromium for any hot zone exposure, mica possessed enough for 3/6 hot zone runs, and alumina did for all six exposures. The signal to noise ratio for cold zone spectra also appears to be higher than hot zone spectra. Short term (24 hour) exposures generally favored Cr^{6+} over chromia for all materials (Figures 65a,b, 66a,c,e, 67a,c,e, and 68a,c,e). Mica was observed to favor Cr^{3+} over time in cold zones (Figure 66a,b,c,d), but quartz wool developed Cr^{6+} over time (Figure 65). The behavior of alumina was observed to be more complicated and will be discussed after interpretation of these general trends.

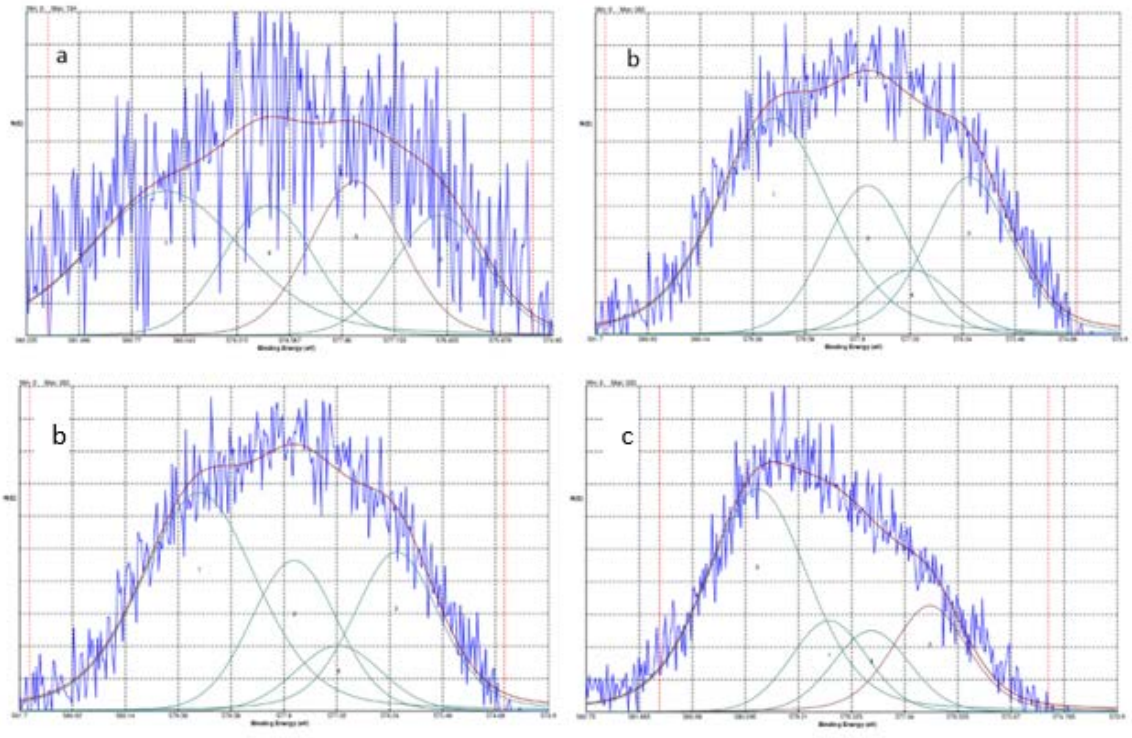


Figure 65 - X-ray photoelectron spectra for quartz wool exposed at 250-300°C for: 24 hours with yellow discoloration (a) and brown discoloration (b), and 100 hours with brown discoloration (c).

Table 7 - Peak information for spectra shown in Figure 65.

Figure 65a	Area %	Peak Position	Oxidation State		Figure 65b	Area %	Peak Position	Oxidation State
1	39.4	580.36	+6		1	44.9	579.05	+6
2	18.0	576.51	+3		2	21.3	577.65	+3
3	23.1	577.67	+3		3	24.5	576.14	+3
4	19.5	578.88	+3		4	9.3	577.00	+3
Figure 65b					Figure 65c			
1	44.9	579.05	+6		1	14.9	578.70	+3
2	21.3	577.65	+3		2	18.9	577.02	+3
3	24.5	576.14	+3		3	52.9	579.89	+6
4	9.3	577.00	+3		4	13.3	578.00	+3

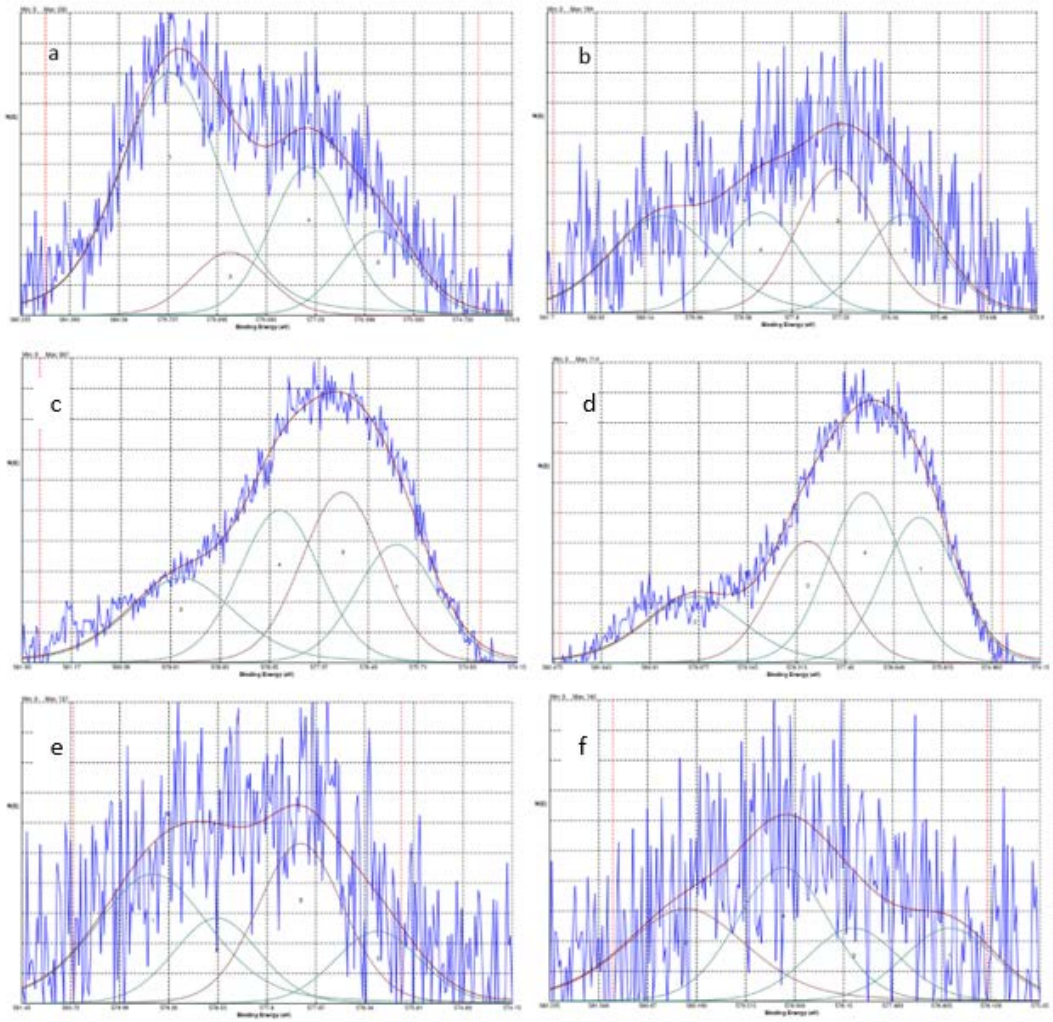


Figure 66 - X-ray photoelectron spectra for mica exposed at: 250-300°C for 24 hours (a) and 100 hours (b), 200-250°C for 24 hours (c) and 100 hours (d), and 900°C for 24 hours (e) and 100 hours (f).

Table 8 - Peak information for spectra shown in Figure 66.

Figure 66a	Area %	Peak Position	Oxidation State		Figure 66b	Area %	Peak Position	Oxidation State
1	54.4	579.69	+6		1	20.4	576.00	+3
2	13.0	576.17	+3		2	29.2	579.86	+6
3	9.7	578.68	+3		3	29.7	577.08	+3
4	22.9	577.36	+3		4	20.7	578.29	+3
Figure 66c					Figure 66d			
1	20.9	576.05	+3		1	27.2	576.21	+3
2	21.8	579.44	+6		2	18.1	580.05	+6
3	30.2	576.91	+3		3	22.8	578.12	+3
4	27.0	577.89	+3		4	31.9	577.14	+3
Figure 66e					Figure 66f			
1	37.2	579.50	+6		1	17.7	576.70	+3
2	14.3	576.15	+3		2	17.7	578.03	+3
3	31.6	577.30	+3		3	32.5	580.34	+6
4	16.9	578.55	+3		4	32.2	579.00	+3

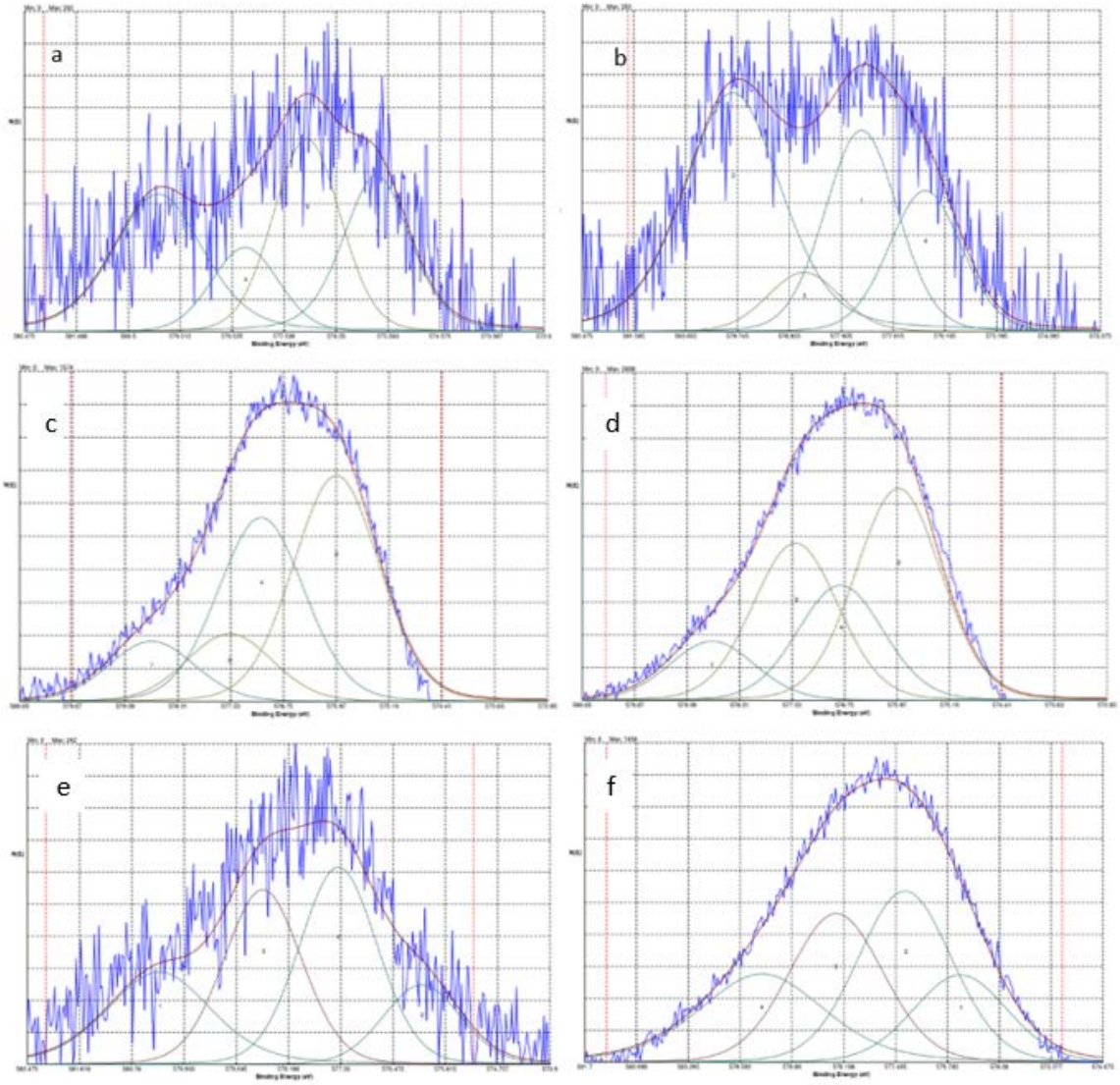


Figure 67 - X-ray photoelectron spectra for alumina exposed at: 250-300°C for 24 hours (a) and 100 hours (b), 200-250°C for 24 hours (c) and 100 hours (d), and 150-200°C for 24 hours (e) and 100 hours (f).

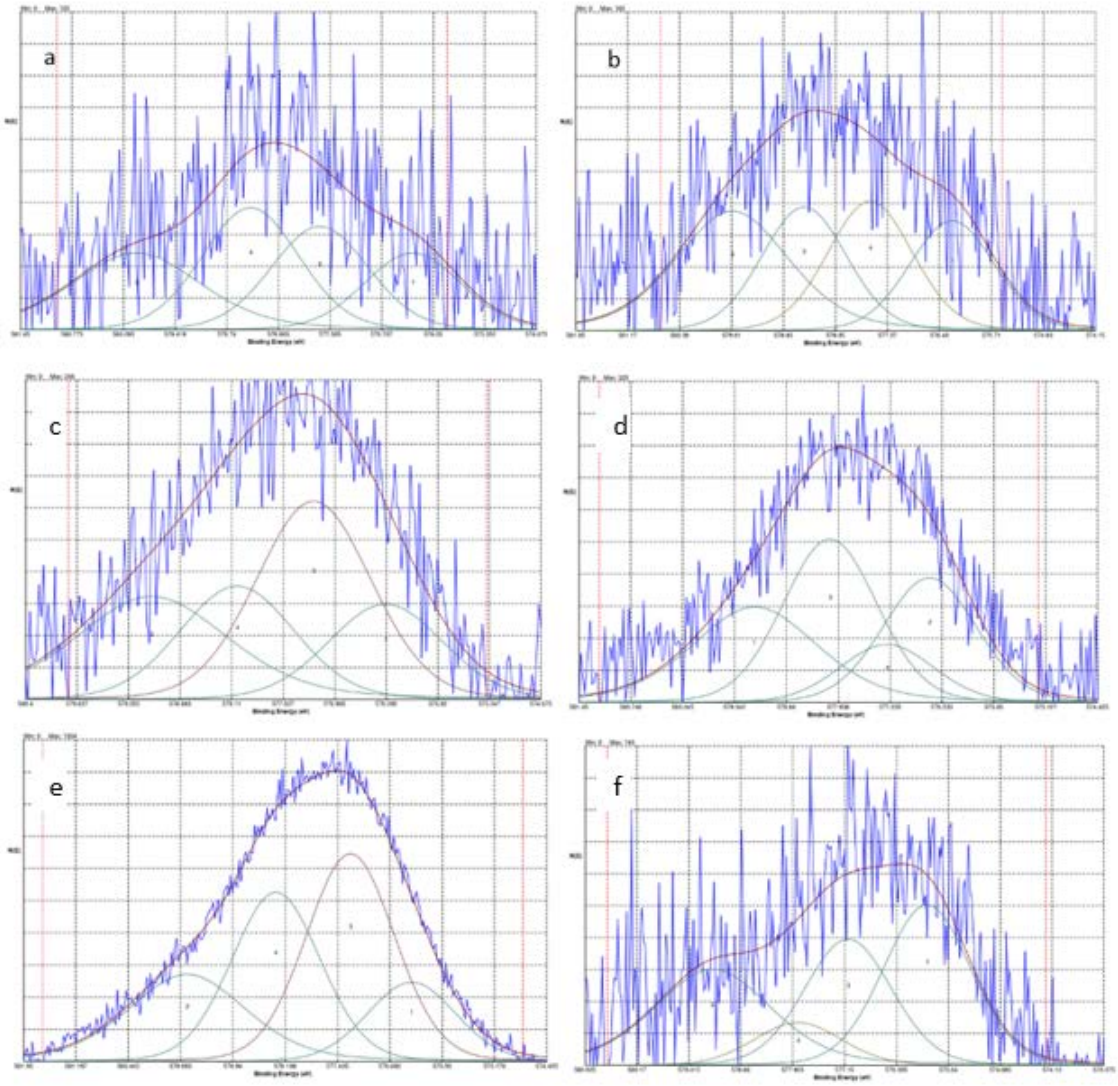


Figure 68 - X-ray photoelectron spectra for alumina exposed at: 900°C for 24 hours (a) and 100 hours (b), 700°C for 24 hours (c) and 100 hours (d), and 500°C for 24 hours (e) and 100 hours (f).

Table 9 - Peak information for spectra shown in Figures 67 and 68.

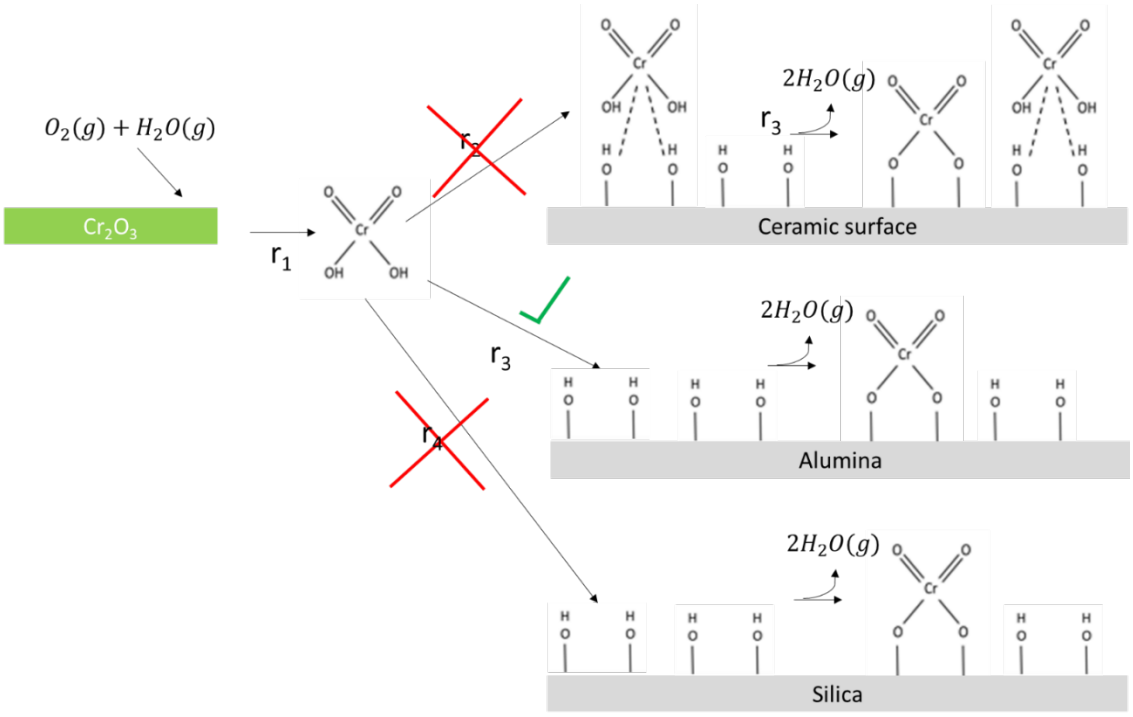
Figure 67a	Area %	Peak Position	Oxidation State		Figure 67b	Area %	Peak Position	Oxidation State
1	26.3	575.78	+3		1	26.9	577.57	+3
2	30.9	579.93	+6		2	46.4	579.83	+6
3	29.8	577.11	+3		3	7.9	578.58	+3
4	13.0	578.28	+3		4	18.8	576.45	+3
Figure 67c					Figure 67d			
1	11.2	578.70	+6		1	10.9	578.72	+6
2	42.0	575.97	+3		2	39.0	575.95	+3
3	12.6	577.55	+3		3	28.9	577.48	+3
4	34.2	577.08	+3		4	21.2	576.81	+3
Figure 67e					Figure 67f			
1	23.0	580.31	+6		1	16.3	576.61	+3
2	13.5	576.00	+3		2	32.0	577.36	+3
3	29.8	578.61	+3		3	27.8	578.29	+3
4	33.6	577.37	+3		4	24.0	579.30	+6
Figure 68a					Figure 68b			
1	17.1	576.40	+3		1	28.7	579.07	+6
2	26.9	579.00	+6		2	25.7	576.70	+3
3	35.6	577.20	+3		3	33.7	578.05	+3
4	20.4	578.05	+3		4	12.0	577.28	+3
Figure 68c					Figure 68d			
1	18.6	576.30	+3		1	20.5	576.30	+3
2	27.0	579.93	+6		2	32.4	579.60	+6
3	25.0	577.52	+3		3	23.0	578.52	+3
4	29.5	578.43	+3		4	24.1	577.53	+3
Figure 68e					Figure 68f			
1	13.6	576.37	+3		1	34.2	575.95	+3
2	21.8	579.60	+6		2	29.8	579.07	+6
3	35.6	577.25	+3		3	26.9	577.10	+3
4	29.0	578.32	+3		4	9.1	577.83	+3

Short term exposures, to various extent, tended to favor Cr^{6+} species over chromia. This is congruent with the general mechanism proposed in the previous study, where at low surface loading, surface chromium takes the form of monochromate. Also in line with the proposed mechanism is the trend for mica to develop Cr^{3+} to a greater

extent when comparing the short and long term exposures (Figure 66a,b,c,d). As the exposure time increases, the amount of chromium loading will also increase which has been noted to favor Cr_2O_3 formation. This trend was not observed on quartz wool, but it is likely due to a difference in surface area of approximately five orders of magnitude between the mica wafers (≈1 cm^2) and quartz wool [190]. Chromium collected on quartz wool may still be relatively well dispersed, leaving chromium at an intermediate stage in the proposed mechanism of CrO_3 formation. Given the literature background on silica supporting chromium, it is assumed that given a longer exposure time Cr_2O_3 formation will predominate, though additional testing is required to verify this assumption.

Some trends are not immediately reconciled by the proposed mechanism and so it must be adjusted. In the proposed mechanism volatile chromium species first physisorb and then chemisorb to a ceramic surface via esterification reactions with hydroxyl groups. These species are chemisorbed as chromate, which may then decompose with increased Cr loading to form several Cr compounds, with Cr_2O_3 formation at the end of the pathway. This mechanism must be adjusted at high (≥500°C) temperatures, as the equilibrium of the adsorption step will shift to favor desorption. For Cr surface species to form at high temperature, volatile chromium must collide, with sufficient energy and the correct orientation, with hydroxyl groups. Since hydroxyl groups act as Cr anchors, their properties will impact Cr collection and stabilization. Alumina, mica, and quartz wool will have different hydroxyl group properties, some beneficial for Cr uptake and some detrimental. Alumina has more hydroxyl groups which are of greater basicity, and more resistant to dehydroxylation than those found on silica [46-51]. This is in line with the

HSAB theory, as aluminum is a harder acid than silicon and is therefore predicted to form a more stable, higher ionic content bond with oxygen acting as a hard base. This results in a higher electron density for hydroxyl groups on alumina which translates to enhanced Lewis basicity. More hydroxyl groups mean more interaction area on the surface for volatile Cr to anchor. The more basic nature of these hydroxyls will allow for a stronger bond to form with volatile Cr acting as a Lewis acid. Additionally, since silica surfaces dehydrate more easily and to a greater extent than alumina surfaces, Cr uptake is diminished. Lastly, the volatility of silica is greater than that of alumina given these conditions [191, 192]. Volatilizing silica would require volatile Cr to counter diffuse past in the boundary layer and would likely disrupt surface hydroxyl sites. These considerations lead to an adjustment of the general mechanism, illustrated in Figure 69. The top pathway, involving physisorption, is precluded at or above 500°C. The pathways requiring direct collisions are the middle and bottom, where the bottom pathway is less favorable for the reasons given above.



$$r_1: \frac{1}{2}Cr_2O_3(s) + \frac{3}{4}O_2(g) + H_2O(g) \rightleftharpoons CrO_2(OH)_2(g)$$

$$r_2: CrO_2(OH)_2(g) \rightleftharpoons CrO_2(OH)_2(a)$$

$$r_3: CrO_2(OH)_2(g) + 2Al - OH(s) \rightleftharpoons Al_2CrO_4(s) + 2H_2O(g)$$

$$r_4: CrO_2(OH)_2(g) + 2Si - OH(s) \rightleftharpoons Si_2CrO_4(s) + 2H_2O(g)$$

Figure 69 - Adjusted mechanism for samples exposed at 500°C and above where physisorption (top pathway) is precluded. The other two pathways, without physisorption, show negligible collection of volatile chromium species on silica compared to collection on alumina.

The trends for alumina at long times have not yet been discussed as they don't exhibit a general trend. Long term exposures for alumina favor Cr 6+ for 250-300°C (Figure 67a, b), Cr 3+ for 200-250°C (Figure 67c,d), and no oxidation state preference for the other temperatures (Figures 67 e,f and 68). Due to the stabilizing influence of Al

discussed previously, surface chromate species on alumina may remain stable at higher Cr loadings than chromate species anchored with Si. This would explain the trend observed for alumina at 250-300°C, but not for the other two temperature ranges. This latter temperature range is unique for this system, as CrO_3 melts at approximately 200°C, and decomposes around 250°C [193]. It is likely that CrO_3 would exist as a liquid in this temperature range, increasing the contact area of CrO_3 with the alumina lattice. Chromium is completely soluble in α-Al_2O_3 [194], with a similar valence, atom size, crystal structure and electronegativity. Given this solubility and enhanced diffusion over the solid state, Cr 3+ may become stabilized in the alumina lattice, resulting in a corundum type solid solution in the form of $(Al,Cr)_2O_3$ near the surface. This is supposition, and will need to be supported using complementary techniques such as XRD to observe the suspected lattice distortion, or time of flight secondary ion mass spectroscopy (ToF-SIMS) elemental depth profiling.

While the previous two temperature ranges strongly favored an oxidation state over time, the 150-200°C did not. One might expect this temperature range to favor Cr 6+ as the 250-300°C range did, since CrO_3 is only assumed to exist in the liquid state from 200-250°C. The difference in behavior may be attributable to the decomposition temperature of CrO_3, previously noted as 250°C. The 250-300°C range exists above the decomposition point of CrO_3, which would result in a high energy intermediate compound when progressing from surface chromate to chromia, as illustrated in Figure 70. This high energy intermediate would serve to stabilize surface chromate, thereby stabilizing Cr 6+. Higher temperatures (500-900°C in Figure 71) likely provide sufficient

energy to proceed past this high energy intermediate, but as chromate species have been observed to be stable up to 1000°C, neither end of the pathway may be favored. At 150-200°C CrO_3 is neither above its decomposition point, nor in a liquid state. Chromium incorporation into the lattice would likely be negligible, and CrO_3 would be a stable surface species. This may allow for a stable equilibrium which does not strongly favor either end of the pathway, surface chromate or chromia, over time.

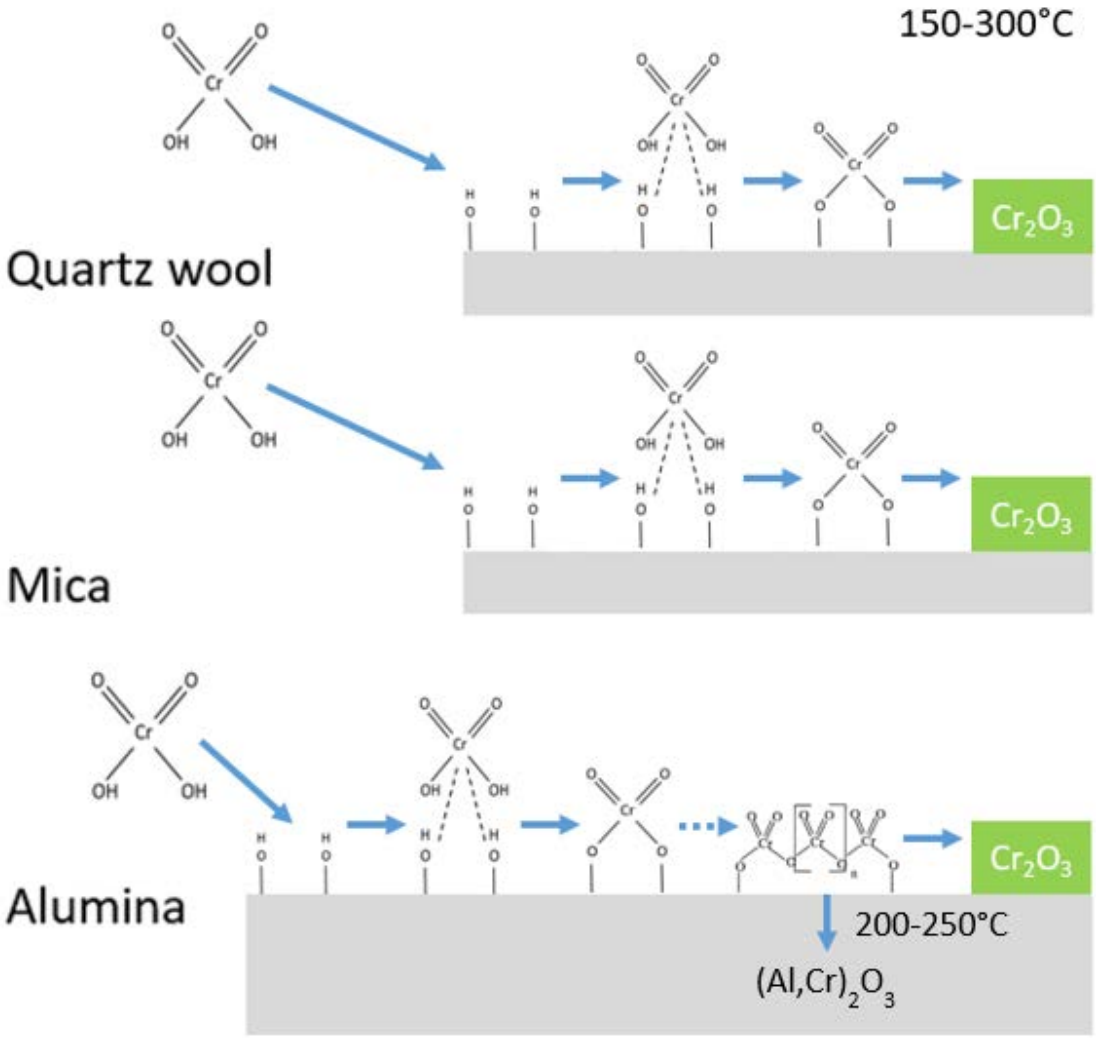


Figure 70 - Mechanisms for each material exposed in cold zones. Note that dashed arrows represent a qualitatively slower reaction rate in the forward direction.

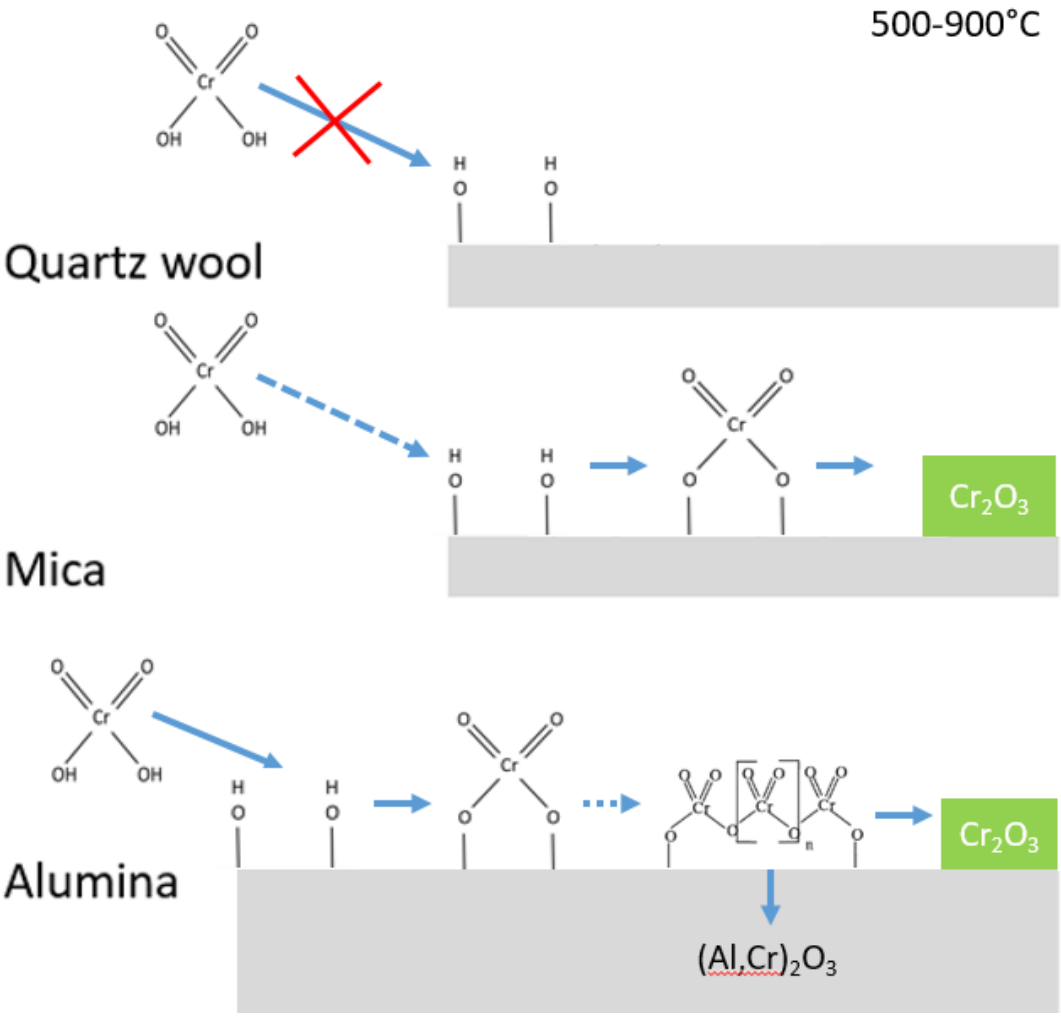


Figure 71 - Mechanisms for each material exposed in hot zones. Note that dashed arrows represent a qualitatively slower reaction rate in the forward direction.

While the mechanisms presented in Figures 70 and 71 are useful to gain a general understanding of how chromium vapor species interact with these surfaces, there is additional nuance which may be noted. As has been discussed, surface hydroxyl groups serve as anchoring points for chromium vapor species. The hydroxyl populations and their basicity vary by material, but also vary on each material. Infrared spectroscopy of alumina surfaces typically reveals at least five OH stretching bands [195] with more basic

OH groups at higher stretching frequencies [196], supported by preferential consumption of OH groups upon chromium loading [166] and stability at elevated temperatures [46]. Three OH stretching bands have been identified using the same technique on silica [197]. Infrared spectroscopic observations of hydroxyl group differences on alumina and silica surfaces are supported by measurement of pKa values. Silica is observed to have bimodal behavior with pKa values of 4.5 and 8.5 [198], with more complex behavior on alumina showing pKa values < 3 and of 4.5, 6.7, and 9.5-9.8 [196].

Including these observations to describe Figures 70 and 71, it may be clarified that each material surface does not possess homogeneous, interchangeable hydroxyl groups. As a result, chromium deposition on these surfaces is not equally likely for any hydroxyl group. This would likely result in preferential attachment on more basic hydroxyl groups first and least basic hydroxyl groups last, in accordance with literature observations [166].

The work presented above comprises a distillation of roughly 70 years of literature relevant to chromium speciation on ceramic surfaces into a general mechanism in which chromium compounds undergo the following: esterification reactions with surface hydroxyl groups to form monochromate, interact as chromium loading increases to form polychromate up to CrO_3, and subsequently decompose into Cr_2O_5, Cr_3O_8, CrO_2, and end at Cr_2O_3. This general mechanism was expanded upon to incorporate the impact of varied temperature ranges for chromium vapor species on silica, mica, and alumina.

CHAPTER SIX

CONCLUSION

Summary and Implications

Work performed regarding the condensation of volatile chromium species on ceramics and XPS characterization thereof highlighted the importance of material, temperature, and chromium loading on surface compound speciation. Speciation was linked to different colors observed on regions of ceramic substrates which were isolated and characterized using XPS. Examination of Cr $2p_{3/2}$ peaks revealed distinct Cr^{6+} content and Cr^{3+} multiplet-split behaviors for each stain color. Brown staining was attributed to CrO_3, yellow to monochromate, and green to Cr_2O_3. The presence of mixed valence Cr^{3+}/Cr^{6+} species were also inferred based on the spectra and relevant literature observations. These compounds were proposed to anchor to ceramic surfaces first by physisorption and subsequent chemisorption (≤300°C) or by only chemisorption (≥500°C) with surface hydroxyl groups. Chemisorbed chromium species originate as monochromate species, which with increased chromium loading may polymerize to form CrO_3. Chromium trioxide may melt and decompose at 200 and 250°C, respectively, resulting in an effervescence of oxygen and formation of Cr_3O_8, Cr_2O_5, CrO_2, and lastly Cr_2O_3.

The material which volatile chromium deposited on was observed to significantly impact collection and speciation of Cr surface compounds. The greater the aluminum content in a ceramic, the more capable that surface was of collecting chromium from

150-900°C. Silicon containing ceramics were only observed to collect chromium up to 300°C, and ceramics containing both were observed to have mixed behavior, collecting at temperatures ≤300°C or ≥700°C. Speciation on silicon containing ceramics was in part observed, and in part assumed in accordance with evidence from relevant literature to favor the formation of Cr_2O_3 with increased Cr loading. This was observed on mica, and assumed to be true for silica which, in the form of quartz wool, had a large surface area on which Cr deposition could occur. Compound formation was observed to be highly temperature dependent on alumina with 250-300°C stabilizing Cr 6+, 200-250°C stabilizing chromia, and 150-200°C, in addition to hot zones, not favoring either side of the pathway. These differences were hypothesized to arise due to the melting and decomposition temperature of CrO_3 being at 200 and 250°C, respectively. As a liquid, CrO_3 would have enhanced contact and diffusion of Cr^{3+} into the corundum type lattice. Above its decomposition temperature CrO_3 would exist as a high energy intermediate, stabilizing the hexavalent chromate species. At temperatures below melting neither side of the pathway has reason to be favored, likewise at temperatures well above the decomposition point sufficient energy to progress beyond the high energy intermediate would prevent favoring of either side of the pathway.

Hydroxyl group population/properties on a ceramic appear to be an important consideration for the reactive condensation of volatile chromium species. Materials with numerous tightly bound hydroxyl groups, such as alumina, allow for numerous anchoring points which have been observed to be stable up to 1000°C. Materials with hydroxyl groups which are more susceptible to dehydroxylation with increased temperature, such

as silica, lose their anchoring points and were observed to collect negligible amounts of chromium. The relative stability of hydroxyl groups for various ceramics was rationalized using hard soft acid base theory. Aluminum is a harder acid than silicon, and thus the ionic content and electron density of hydroxyl groups on aluminum will be greater. This allows for a more stable bond to the support and enhanced Lewis basicity allowing for a more stable bond with chromium acting as a Lewis acid.

The impact of the generation of volatile chromium species from FSS 409 was also examined with and without aluminosilicate fiber contact. The fibers were observed to have a substantial impact on corrosion behavior. Smaller oxide nodules were observed in contacting regions, and evidence of localized breakaway corrosion in moist air was no longer evident in the contacting condition. The effect was attributed to the fibers acting as a mass transport barrier to corrosive gas species, resulting in a decrease in pO_2 and an increase in the H_2/H_2O ratio in the fiber contacting regions. This behavior could prove valuable to attenuate oxide scale formation and the reactive evaporation of chromium if getter materials on fibrous supports are implemented in SOFCs.

A variety of ceramic materials in this work were observed to collect chromium vapor species. Collection of chromium was hypothesized to be facilitated by surface hydroxyl groups. This was supported by chromium collection on various ceramics at or below 300°C, a temperature condition in which hydroxyl groups are largely available on all materials, but negligible collection at or above 500°C for materials which are expected to be largely dehydroxylated. This suggests ceramics with a dearth of hydroxyl groups are less likely to collect chromium vapor species. Attached chromium species are also

dependent on hydroxyl groups, with surfaces densely populated with hydroxyl groups able to stabilize hexavalent chromate species at higher chromium loadings than surfaces sparsely populated with hydroxyl groups. The latter are less capable of dispersing chromium species, resulting in agglomeration and subsequent formation of chromia at lower chromium loadings.

Limitations and Future Work

There are several ways in which future work may test and expand on the claims made herein. Different phases of alumina (e.g. α, γ, η, θ, etc.) have been observed to possess similar hydroxyl populations [160, 195, 199] but varying acidity [160, 195, 200]. They also vary in surface area, but as was seen in this study between quartz wool and alumina, at temperatures of 500°C or greater the ability of a material to stabilize hydroxyl groups appears to be more important for Cr condensation. If more acidic alumina phases, such as γ-alumina [195, 200, 201], collect more Cr than less acidic phases, such as θ-alumina [195, 200, 201], then this would support the claims of the importance of Lewis acidity made here. A similar experiment to the one pursued in this investigation could be performed. Various alumina phases may be exposed to volatile chromium species over a range of temperatures, such as 300, 500, 700, and 900°C for a time period of 50 hours. If Lewis acidity is an important factor, then one might not expect to see a difference in collection and/or speciation at low temperatures, but at higher temperatures, given the findings in this work, increased Lewis acidity should result in greater chromium collection at higher temperature.

Alternative materials with a lower hardness than Al^{3+}, but hydroxyl populations greater than silica, such as ceria and titania [202], may be tested to see if these materials show intermediate behavior as the mica did in this study. It may also be of benefit to use aluminosilicates with a range of compositions (e.g. Al_2O_3, 20% SiO_2 · 80% Al_2O_3, 40% SiO_2 · 60% Al_2O_3, 60% SiO_2 · 40% Al_2O_3, 80% SiO_2 · 20% Al_2O_3, SiO_2) as Weckhuysen et al. have repeatedly done [45, 49, 203]. If these materials do show intermediate behavior, then it would support the hypothesis and the broad applicability of the hypothesis. Reactive condensation on materials of interest to SOFCs such as LSCF and its constituent single element oxides, similar to the work performed by Tucker et al. [130] but more surface sensitive, may be of value to improve the mechanism proposed here. Chromium is not believed to react with quartz wool, mica, or alumina supports in this study to form a new phase. Constituents from LSCF (e.g. SrO, La_2O_3, etc.), however, have been observed to form $FeCr_2O_4$ above 600°C [204], $SrCrO_4$ above 700°C [103], $CoCr_2O_4$ [27], and $LaCrO_3$ 800°C [23]. The mechanism proposed herein does not account for reaction with the substrate material. A possible experiment could include exposure of SrO, and varied compositions of $SrO{\cdot}SiO_2{\cdot}Al_2O_3$ glass to varied temperature and chromium loading. There may also be value in varying the degree of crystallinity of $SrO{\cdot}SiO_2{\cdot}Al_2O_3$ compounds to examine if the crystalline character of a ceramic has an impact of chromium collection or subsequent surface chromium compound speciation.

The mobility of surface chromium species may also be explored further in the future. Mobility was examined for a chromium on a silica fixed bed and silica powder by McDaniel [164]. As alumina surfaces are proposed to stabilize surface chromium more

effectively than silica, it may be expected that the mobility of surface chromium species on alumina is lesser than on silica. This would have implications on the re-oxidation of chromium on alumina, as this mobility was noted to be an unloading mechanism for surfaces which possess chromium, and the degree of chromium loading has been observed to impact chromium speciation and oxidation state(s).

Additionally, experiments varying the flow rate may be performed to test for potential impacts on chromium deposition and speciation. This may be done by using one low flow rate and one high flow rate. Varying the flow rate would also vary the amount of chromium transported, and so the experiment would have to compensate. For example if flow rate “A” is four times larger than flow rate “B”, then the exposure for flow rate “B” may be four times as long. This is assuming a linear relationship between flow rate and chromium transported. It would be prudent to test this by first running flow rates A and B for the time selected for the flow rate experiment and quantifying the chromium transported. This may be accomplished by using a quartz wool collector downstream of the chromium vapor species for ten hours in flow rate A, and a separate quartz wool collector for ten hours in flow rate B, both collecting at the same temperature. Quartz wool collectors may then be washed in 1% nitric acid and subsequently quantified using ICP-MS. The extra time which flow rate “B” would need to be exposed could be determined based on this quantification.

The additional time at temperature is another confound in such an experiment which would need to be considered. To see if this additional time would be an issue, two equivalent samples could be run side by side in the furnace such that they should form the

same surface compounds. One may be removed, but the other held at temperature for the amount of additional time required in the experiment without any flow or chromium source. If the two samples still exhibit similar behavior despite one being held at temperature long after the other, then running flow rate “B” four times longer than flow rate “A” shouldn’t introduce a confounding factor. It may also be of value to perform high velocity flow rate testing, possibly in collaboration with the Opila research group at the University of Virginia which possesses a steam jet furnace capable of delivering flow rates of 150-200 m/s.

Lastly, several limitations of this study may also be addressed in future work. Longer exposure times would be useful to ensure sufficient coverage for high surface area materials, such as quartz wool in this study, to check for adherence to the proposed mechanism, and to test if there is a long term saturation condition in which materials will no longer collect chromium. Chromium content could be checked using ICP-MS for exposure times of 200, 500, and 1000 hours, for example. Alternative characterization techniques, especially those capable of phase identification such as XRD or EBSD, may be pursued to support or contest findings here.

REFERENCES CITED

1. Tatar, G., Gannon, P., Swain, N., Remington, E., and Dansereau, S. (2018). "Surface Studies of T409 Stainless Steel at 700 °C in Wet or Dry Air or N2 With and Without Contacting Ceramic Fibers." Oxidation of Metals.

2. Tatar, G., Gannon, P., Swain, N., Mason, R., Remington, E., and Dansereau, S. (2018). "XPS Characterization of Aluminosilicate Fibers Post Interaction with Chromium Oxyhydroxide at 100–230°C." Journal of The Electrochemical Society **165**(10): C624-C632.

3. Tatar, G., Gannon, P., Swain, N., Mason, R., Remington, E., and Dansereau, S. "Investigation of Surface Interactions between Volatile Chromium Species and Ceramics." Manuscript submitted for publication.

4. Aller, J., Swain, N., Baber, M., Tatar, G., Jacobson, N., and Gannon, P. (2017). "Influence of silicon on high-temperature (600°C) chlorosilane interactions with iron." Solar Energy Materials and Solar Cells **160**: 410-417.

5. Aller, J., Mason, R., Walls, K., Tatar, G., Jacobson, N., and Gannon, P. (2016). "High-Temperature (550–700°C) Chlorosilane Interactions with Iron." Journal of The Electrochemical Society **163**(10): C666-C674.

6. McHenry H.I. (1983) The Properties of Austenitic Stainless Steel at Cryogenic Temperatures. In: Reed R.P., Horiuchi T. (eds) Austenitic Steels at Low Temperatures. Springer, Boston, MA.

7. Young, D. J. *High temperature oxidation and corrosion of metals / David J. Young*, 2nd ed.; Elsevier: Amsterdam, 2016.

8. Wilbur, S., Abadin, H., Fay, M., Yu, D., Tencza, B., Ingerman, L., Koltzbach, J., and James, S. (2012). "Toxicological Profle for Chromium." Agency for Toxic Substances and Disease Registry.

9. Katz, S. A. and H. Salem (1993). "The toxicology of chromium with respect to its chemical speciation: A review." Journal of Applied Toxicology **13**(3): 217-224.

10. Saha, R., Nandi, R., and Saha, B. (2011). "Sources and toxicity of hexavalent chromium." Journal of Coordination Chemistry **64**(10): 1782-1806.

11. Cooper, L., Benhaddad, S., Wood, A., and Ivey, D. G. (2008). "The effect of surface treatment on the oxidation of ferritic stainless steels used for solid oxide fuel cell interconnects." Journal of Power Sources **184**(1): 220-228.

12. Froitzheim, J., Meier, G. H., Niewolak, L., Ennis, P. J., Hattendorf, H., Singheiser, L., and Quadakkers, W. J. (2008). "Development of high strength ferritic steel for interconnect application in SOFCs." Journal of Power Sources **178**(1): 163-173.

13. Froitzheim, J., Larsson, E., Johansson, L. G., Svensson, J. E. (2009). "Cr Evaporation of Metallic Interconnects: A Novel Method for Quantification." ECS Transactions **25**(2): 1423-1428.

14. Asteman, H., Svensson, J. E., and Johansson, L. G. (2002). "Evidence for Chromium Evaporation Influencing the Oxidation of 304L: The Effect of Temperature and Flow Rate." Oxidation of Metals **57**(3): 193-216.

15. Asteman, H., Svensson, J. E., Johansson, L. G., and Norell, M. (1999). "Indication of Chromium Oxide Hydroxide Evaporation During Oxidation of 304L at 873 K in the Presence of 10% Water Vapor." Oxidation of Metals **52**(1): 95-111.

16. Segerdahl, K., Svensson, J.-E. and Johansson, L.-G. (2002). "The high temperature oxidation of 11% chromium steel: Part I – Influence of pH2O." Materials and Corrosion **53**(4): 247-255.

17. Collins, C., Lucas, J., Buchanan, T. L., Kopczyk, M., Kayani, A., Gannon, P., Deibert, M. C., Smith, R. J., Choi, D. S., and Gorokhovsky, V.I. (2006). "Chromium volatility of coated and uncoated steel interconnects for SOFCs." Surface and Coatings Technology **201**(7): 4467-4470.

18. Holcomb, G. R. and D. E. Alman (2006). "The effect of manganese additions on the reactive evaporation of chromium in Ni–Cr alloys." Scripta Materialia **54**(10): 1821-1825.

19. Hilpert, K., Das, D., Miller, M., Peck, D. H., Wei, R. (1996). "Chromium Vapor Species Over Solid Oxide Fuel Cell Interconnect Materials and Their Potential for Degradation Processes." Journal of the Electrochemical Society **143**(11): 3642-3647.

20. Peck, D.-H., Miller, M., and Hilpert, K. (2001). "Vaporization and thermodynamics of La1−xSrxCrO3−δ investigated by Knudsen effusion mass spectrometry." Solid State Ionics **143**(3): 401-412.

21. Stambouli, A. B. and E. Traversa (2002). "Solid oxide fuel cells (SOFCs): a review of an environmentally clean and efficient source of energy." Renewable and Sustainable Energy Reviews **6**(5): 433-455.

22. Badwal, S. P. S. and K. Foger (1996). "Solid oxide electrolyte fuel cell review." Ceramics International **22**(3): 257-265.

23. Fontana, S., Amendola, R., Chevalier, S., Piccardo, P., Caboche, G., Viviani, M., Molins, R., and Sennour, M. (2007). "Metallic interconnects for SOFC: Characterisation of corrosion resistance and conductivity evaluation at operating temperature of differently coated alloys." Journal of Power Sources **171**(2): 652-662.

24. Fergus, J. W. (2007). "Effect of cathode and electrolyte transport properties on chromium poisoning in solid oxide fuel cells." International Journal of Hydrogen Energy **32**(16): 3664-3671.

25. Jiang, S. P. and X. Chen (2014). "Chromium deposition and poisoning of cathodes of solid oxide fuel cells – A review." International Journal of Hydrogen Energy **39**(1): 505-531.

26. Liang, C., Hu, B., Aphale, A., Venkataraman, M., Mahapatra, M. K., and Singh, P. (2017). "Mitigation of Chromium Assisted Degradation of LSM Cathode in SOFC." ECS Transactions **75**(28): 57-64.

27. Komatsu, T., Chiba, R., Arai, H., and Sato, K. (2008). "Chemical compatibility and electrochemical property of intermediate-temperature SOFC cathodes under Cr poisoning condition." Journal of Power Sources **176**(1): 132-137.

28. Vora, S. (2016). Department of Energy Office of Fossil Energy's Solid Oxide Fuel Cell (SOFC) Program. Presentation. 17th Annual SOFC Workshop, Pittsburgh, PA.

29. Menzler, N. H., Batfalsky, P., Gro, S., Shemet, V., and Tietz, F. (2011). "Post-Test Characterization of an SOFC Short-Stack after 17,000 Hours of Steady Operation." ECS Transactions **35**(1): 195-206.

30. Malzbender, J., Batfalsky, P., Gro, S., Shemet, V., and Tietz, F. (2012). "Component interactions after long-term operation of an SOFC stack with LSM cathode." Journal of Power Sources **201**: 196-203.

31. Opila, E. J., Myers, D. L., Jacobson, N., Nielsen, I. M. B., Johnson, D. F., Olminsky, J. K., and Allendrof, M. D. (2007). "Theoretical and Experimental Investigation of the Thermochemistry of CrO2(OH)2(g)." ChemInform **38**(23): 1971-1980.

32. Jacobson, N., Myers, D., Opila, E., and Copland, E. (2005). "Interactions of water vapor with oxides at elevated temperatures." Journal of Physics and Chemistry of Solids **66**(2): 471-478.

33. Gindorf, C., Singheiser, L, and Hilpert, K. (2005). "Vaporisation of chromia in humid air." Journal of Physics and Chemistry of Solids **66**(2): 384-387.

34. Kurokawa, H., Jacbonson, C. P., DeJonghe, L. C., and Visco, S. J. (2007). "Chromium vaporization of bare and of coated iron–chromium alloys at 1073 K." Solid State Ionics **178**(3): 287-296.

35. Stanislowski, M., Froitzheim, J., Niewolak, L., Quaddakers, W. J., Hilpert, K., Markus, T., and Singheiser, L. (2007). "Reduction of chromium vaporization from SOFC interconnectors by highly effective coatings." Journal of Power Sources **164**(2): 578-589.

36. Holcomb, G. R. (2008). "Calculation of Reactive-evaporation Rates of Chromia." Oxidation of Metals **69**(3): 163-180.

37. Key, C., Eziashi, J., Froitzheim, J., Amendola, R., Smith, R., and Gannon, P. (2014). "Methods to Quantify Reactive Chromium Vaporization from Solid Oxide Fuel Cell Interconnects." Journal of The Electrochemical Society **161**(9): C373-C381.

38. Eziashi, J. J., Key, C., Smith, R., Amendola, R., Gannon, P., and Froitzheim, J. (2013). "Measuring Cr Volatility from Ferritic Stainless Steels: Novel and Conventional Methods Compared." ECS Transactions **50**(44): 43-49.

39. Koukkari, P. (2014). “Introduction to constrained Gibbs energy methods in process and materials research.” (VTT Technology; Vol. 160). Espoo: VTT Technical Research Centre of Finland.

40. Wichterle, I., Linek, J., Wagner, Z., Fontaine, J. C., Sosnkowska, K. K., and Kehiaian, H. V. (2008). Vapor-Liquid Equilibrium of the Mixture CF4 + CHF3 (LB3808, EVLM 1131). Binary Liquid Systems of Nonelectrolytes. Part 2. H. V. Kehiaian. Berlin, Heidelberg, Springer Berlin Heidelberg**:** 3260-3262.

41. Yamamoto, H., Hiyama, T., Kanie, K., Kusumoto, T., Morizawa, Y., and Shimzu, M. (2013). Organofluorine Compounds: Chemistry and Applications, Springer Berlin Heidelberg.

42. Costa, J. C. S., Mendes, A. Santos, L. M. N. F. (2018). "Chain Length Dependence of the Thermodynamic Properties of n-Alkanes and their

Monosubstituted Derivatives." Journal of Chemical & Engineering Data **63**(1): 1-20.

43. Johnson, J. R. T. and I. Panas (2000). "Hydrolysis on Transition Metal Oxide Clusters and the Stabilities of M−O−M Bridges." Inorganic Chemistry **39**(15): 3192-3204.

44. Johnson, J. R. T. and I. Panas (2000). "Water Adsorption and Hydrolysis on Molecular Transition Metal Oxides and Oxyhydroxides." Inorganic Chemistry **39**(15): 3181-3191.

45. Weckhuysen, B. M., Verberkmoes, A. A., Buttiens, A. L., and Schoonheydt, R. A. (1994). "Diffuse reflectance spectroscopy study of the thermal genesis and molecular structure of chromium-supported catalysts." The Journal of Physical Chemistry **98**(2): 579-584.

46. Hardcastle, F. D. and I. E. Wachs (1988). "Raman spectroscopy of chromium oxide supported on Al2O3, TiO2 and SiO2: a comparative study." Journal of Molecular Catalysis **46**(1): 173-186.

47. K. Jozwiak, W. and I. G. Dalla Lana (1997). "Interactions between the chromium oxide phase and support surface; redispersion of [small alpha]-chromia on silica, alumina and magnesia." Journal of the Chemical Society, Faraday Transactions **93**(15): 2583-2589.

48. Weckhuysen, B. M., Wachs, I. E., and Schoonheydt, R. A. (1996). "Surface Chemistry and Spectroscopy of Chromium in Inorganic Oxides." Chemical Reviews **96**(8): 3327-3350.

49. Weckhuysen, B. M., De Ridder, L. M., Grobet, P. J., and Schoonheydt, R. A. (1995). "Redox Behavior and Dispersion of Supported Chromium Catalysts." The Journal of Physical Chemistry **99**(1): 320-326.

50. McCafferty, E. and Wightman. J. P. (1998). "Determination of the concentration of surface hydroxyl groups on metal oxide films by a quantitative XPS method." Surface and Interface Analysis **26**(8): 549-564.

51. Fouad, N. E., Knözinger, H., Zaki, M. I., and Mansour, S. A. A. (1991). Chromia on Silica and Alumina Catalysts. Zeitschrift für Physikalische Chemie. **171:** 75.

52. Tripp, H. P. and B. W. King (1955). "Thermodynamic Data on Oxides at Elevated Temperatures." Journal of the American Ceramic Society **38**(12): 432-437.

53. Zhou, G. (2009). "Nucleation thermodynamics of oxide during metal oxidation." Applied Physics Letters **94**(20): 201905.

54. Palacio, C., Mathieu, H. J., and Landolt, D. (1987). "AES, XPS and EELS study of the initial oxidation of polycrystalline chromium." Surface Science **182**(1): 41-55.

55. Evans, H. E. (1995). "Stress effects in high temperature oxidation of metals." International Materials Reviews **40**(1): 1-40.

56. Ebbinghaus, B. B. (1993). "Thermodynamics of gas phase chromium species: The chromium oxides, the chromium oxyhydroxides, and volatility calculations in waste incineration processes." Combustion and Flame **93**(1): 119-137.

57. Golden, R. A. and E. J. Opila (2016). "A method for assessing the volatility of oxides in high-temperature high-velocity water vapor." Journal of the European Ceramic Society **36**(5): 1135-1147.

58. Gindorf, C., Hilpert, K., Nabielek, H., and Singheiser, L. (2001). "Chromium Release from Metallic Interconnects with and without coatings." Conference Paper.

59. Abelián, J. P., Shemet, V., Tietz, F., Singheiser, L., Quadakkers, W. J., and Gil, A. (2001). "Ferritic Steel Interconnect for Reduced Temperature SOFC." ECS Proceedings Volumes **2001-16**: 811-819.

60. Segerdahl, K., Svensson, J. E., Halvarsson, M., Panas, I., and Johansson, L. G. (2005). "Breakdown of the protective oxide on 11 % Cr steel at high temperature in the presence of water vapor and oxygen, the influence of chromium vaporization." Materials at High Temperatures **22**(1-2): 69-78.

61. Asteman, H., Svensson, J. E., Norell, M., and Johansson, L. G. (2000). "Influence of Water Vapor and Flow Rate on the High-Temperature Oxidation of 304L; Effect of Chromium Oxide Hydroxide Evaporation." Oxidation of Metals **54**(1): 11-26.

62. A. P. Sutton and R. W. Balluffi, (1995). “Interfaces in Crystalline Materials.” Chap. 8 Oxford Science, New York.

63. Essuman, E., Meier, G. H., Zurek, J., Hänsel, M., Singheiser, L. and Quadakkers, W. J. (2007). "Enhanced internal oxidation as trigger for breakaway oxidation of Fe–Cr alloys in gases containing water vapor." Scripta Materialia **57**(9): 845-848.

64. Ehlers, J., Young, D. J., Smaardijk, E. J., Tyagi, A. K., Penkalla, H. J., Singheiser, L., and Quadakkers, W. J. (2006). "Enhanced oxidation of the 9%Cr steel P91 in water vapour containing environments." Corrosion Science **48**(11): 3428-3454.

65. Pint, B. A. (1996). "Experimental observations in support of the dynamic-segregation theory to explain the reactive-element effect." Oxidation of Metals **45**(1): 1-37.

66. Qu, W., Jian, L., Ivey, D. G., and Hill, J. M. (2006). "Yttrium, cobalt and yttrium/cobalt oxide coatings on ferritic stainless steels for SOFC interconnects." Journal of Power Sources **157**(1): 335-350.

67. Zhu, J. H., Zhang, Y., Basu, A., Lu, Z. G., Paranthaman, M., Lee, D. F., and Payzant, E. A. (2004). "LaCrO3-based coatings on ferritic stainless steel for solid oxide fuel cell interconnect applications." Surface and Coatings Technology **177**: 65-72.

68. Shaigan, N., Qu, W., Ivey, D. G., and Chen, W. (2010). "A review of recent progress in coatings, surface modifications and alloy developments for solid oxide fuel cell ferritic stainless steel interconnects." Journal of Power Sources **195**(6): 1529-1542.

69. Anderson, H. U. (1992). "Review of p-type doped perovskite materials for SOFC and other applications." Solid State Ionics **52**(1): 33-41.

70. Jun, A., Kim, J., Shin, J., and Kim, G. (2016). "Perovskite as a Cathode Material: A Review of its Role in Solid-Oxide Fuel Cell Technology." ChemElectroChem **3**(4): 511-530.

71. Taroco, H. A., Santos, J. A. F., Domingues, R. Z., and Matencio, T. (2011). "Ceramic Materials for Solid Oxide Fuel Cells." Advances in Ceramics.

72. Yang, Z., Xia, G. G., Maupin, G. D., and Stevenson, J. W. (2006). "Evaluation of Perovskite Overlay Coatings on Ferritic Stainless Steels for SOFC Interconnect Applications." Journal of The Electrochemical Society **153**(10): A1852-A1858.

73. Feng, Z. J., Xu, Y. X., and Zeng, C. L. (2013). "Preparation and high temperature performances of DyCrO3-based coatings on a ferritic stainless steel interconnect material." Journal of Power Sources **235**: 54-61.

74. Lee, S., Chu, C. L., Tsai, M. J., and Lee, Jye. (2010). "High temperature oxidation behavior of interconnect coated with LSCF and LSM for solid oxide fuel cell by screen printing." Applied Surface Science **256**(6): 1817-1824.

75. Yang, Z., Xia, G. G., Li, X. H., and Stevenson, J. W. (2007). "(Mn,Co)3O4 spinel coatings on ferritic stainless steels for SOFC interconnect applications." International Journal of Hydrogen Energy **32**(16): 3648-3654.

76. Yang, Z., Xia, G., and Stevenson, J. (2005). "Mn1.5Co1.5 O 4 Spinel Protection Layers on Ferritic Stainless Steels for SOFC Interconnect Applications." Electrochemical and Solid-State Letters **8**(3): A168-A170.

77. Bateni, M. R., Wei, P., Deng, X., and Petric, A. (2007). "Spinel coatings for UNS 430 stainless steel interconnects." Surface and Coatings Technology **201**(8): 4677-4684.

78. Larring, Y. and T. Norby (2000). "Spinel and Perovskite Functional Layers Between Plansee Metallic Interconnect (Cr-5 wt % Fe-1 wt % Y 2 O 3) and Ceramic (La0.85Sr0.15) 0.91MnO3 Cathode Materials for Solid Oxide Fuel Cells." Journal of The Electrochemical Society **147**(9): 3251-3256.

79. Qu, W., Jian, L., Hill, J. M., and Ivey, D. G. (2006). "Electrical and microstructural characterization of spinel phases as potential coatings for SOFC metallic interconnects." Journal of Power Sources **153**(1): 114-124.

80. Limooei, M. B., Ebrahimifar, H., and Hosseini, S. (2013). "Study of the Oxidation Resistance of Coated AISI 441 Ferritic Stainless Steel for SOFCs." International Journal of Chemical, Molecular, Nuclear, Materials and Metallurgical Engineering **7**(7): 571-574.

81. Yang, Z. G., Hardy, J. S., Walker, M. S., Xia, G., Simner, S. P., and Stevenson, J. W. (2004). "Structure and Conductivity of Thermally Grown Scales on Ferritic Fe-Cr-Mn Steel for SOFC Interconnect Applications." Journal of the Electrochemical Society, **151**(11): A1825: A1831.

82. Hua, B., Pu, J., Gong, W., Zhang, J., Lu, F., Jian, L. (2008). "Cyclic oxidation of Mn–Co spinel coated SUS 430 alloy in the cathodic atmosphere of solid oxide fuel cells." Journal of Power Sources **185**(1): 419-422.

83. Chen, X., Hou, P. Y., Jacobson, C. P., Visco, S. J., and De Jonghe, L. C. (2005). "Protective coating on stainless steel interconnect for SOFCs: oxidation kinetics and electrical properties." Solid State Ionics **176**(5): 425-433.

84. Trebbels, R., Markus, T., and Singheiser, L. (2009). "Investigation of Chromium Vaporization From Interconnector Steels With Spinel Coatings." Journal of Fuel Cell Science and Technology **7**(1): 011013-011013-011016.

85. Yang, Z., Xia, G., Nie, Z., Templeton, J., and Stevenson, J. W. (2008). "Ce-Modified (Mn , Co) 3O4 Spinel Coatings on Ferritic Stainless Steels for SOFC Interconnect Applications." Electrochemical and Solid-State Letters **11**(8): B140-B143.

86. Montero, X., Tietz, F., Sebold, D., Buchkremer, H. P., Ringuede, A., Cassir, M., Laresgoiti, A., and Villarreal, I. (2008). "MnCo1.9Fe0.1O4 spinel protection layer on commercial ferritic steels for interconnect applications in solid oxide fuel cells." Journal of Power Sources **184**(1): 172-179.

87. Park, B.-K., Lee, J. W., Lee, S. B., Lim, T. H., Park, S. J., Park, C. O., and Song, R. H. (2013). "Cu- and Ni-doped Mn1.5Co1.5O4 spinel coatings on metallic interconnects for solid oxide fuel cells." International Journal of Hydrogen Energy **38**(27): 12043-12050.

88. Singh, P. (2017). Materials and Approaches for the Mitigation of SOFC Cathode Degradation in SOFC Power Systems. Presentation. 18th Annual SOFC Program Review Meeting.

89. Tveten, B., Hultquist, G., and Norby, T. (1999). "Hydrogen in Chromium: Influence on the High-Temperature Oxidation Kinetics in O2, Oxide-Growth Mechanisms, and Scale Adherence." Oxidation of Metals **51**(3): 221-233.

90. Galerie, A., Henry, S., Wouters, Y., Mermoux, M., Petit, J. P., and Antoni, L. (2005). "Mechanisms of chromia scale failure during the course of 15–18Cr ferritic stainless steel oxidation in water vapour." Materials at High Temperatures **22**(1-2): 105-112.

91. Parks, G. A. (1965). "The Isoelectric Points of Solid Oxides, Solid Hydroxides, and Aqueous Hydroxo Complex Systems." Chemical Reviews **65**(2): 177-198.

92. Raynaud, G. M. and R. A. Rapp (1984). "In situ observation of whiskers, pyramids and pits during the high-temperature oxidation of metals." Oxidation of Metals **21**(1): 89-102.

93. Jiang, N. and J. Silcox (2000). "Observations of reaction zones at chromium/oxide glass interfaces." Journal of Applied Physics **87**(8): 3768-3776.

94. Smeacetto, F., Salvo, M., Ferraris, M., Cho, J., and Boccaccini, A. R. (2008). "Glass–ceramic seal to join Crofer 22 APU alloy to YSZ ceramic in planar SOFCs." Journal of the European Ceramic Society **28**(1): 61-68.

95. Yuan, D. J. (2008). Solid Oxide Fuel Cells. Presentation. Department of Energy Sciences, Lund Institute of Technology, Sweden.

96. Singhal, S. C. (2000). "Advances in solid oxide fuel cell technology." Solid State Ionics **135**(1): 305-313.

97. Ivers-Tiffée, E., Weber, A., and Herbstritt, D. (2001). "Materials and technologies for SOFC-components." Journal of the European Ceramic Society **21**(10): 1805-1811.

98. Liu, M., Dong, D., Peng, R., Gao, J., Diwu, J., Lui, X., and Meng, G. (2008). "YSZ-based SOFC with modified electrode/electrolyte interfaces for operating at temperature lower than 650°C." Journal of Power Sources **180**(1): 215-220.

99. Will, J., Mitterdorfer, A., Kleinlogel, C., Perednis, D., and Gauckler, L. J. (2000). "Fabrication of thin electrolytes for second-generation solid oxide fuel cells." Solid State Ionics **131**(1): 79-96.

100. Oh, E.-O., Whang, C. M., Lee, Y. R., Lee, J. H., Yoon, K. J., Kim, B. K., Son, J. W., Lee, J. H., and Lee, H. W. (2012). "Thin film yttria-stabilized zirconia electrolyte for intermediate-temperature solid oxide fuel cells (IT-SOFCs) by chemical solution deposition." Journal of the European Ceramic Society **32**(8): 1733-1741.

101. Tarancón, A. (2009). "Strategies for Lowering Solid Oxide Fuel Cells Operating Temperature." Energies **2**(4).

102. Sun, C., Hui, R., and Roller, J. (2010). "Cathode materials for solid oxide fuel cells: a review." Journal of Solid State Electrochemistry **14**(7): 1125-1144.

103. Lau, G. Y., Tucker, M. C., Jacobson, C. P., Visco, S. J., Gleixner, S. H., and De Jonghe, L. C. (2010). "Chromium transport by solid state diffusion on solid oxide fuel cell cathode." Journal of Power Sources **195**(22): 7540-7547.

104. Komatsu, T., Arai, H., Chiba, R., Nozawa, K., Arakawa, M., and Sato, K. (2006). "Cr Poisoning Suppression in Solid Oxide Fuel Cells Using LaNi (Fe) O3 Electrodes." Electrochemical and Solid-State Letters **9**(1): A9-A12.

105. Orui, H., Watanabe, K., Chiba, R., and Arakawa, M. (2004). "Application of LaNi (Fe) O 3 as SOFC Cathode." Journal of The Electrochemical Society **151**(9): A1412-A1417.

106. Liu, Z., Liu, M., Yang, L., and Liu, M. (2013). "LSM-infiltrated LSCF cathodes for solid oxide fuel cells." Journal of Energy Chemistry **22**(4): 555-559.

107. Simwonis, D., Tietz, F., and Stöver, D. (2000). "Nickel coarsening in annealed Ni/8YSZ anode substrates for solid oxide fuel cells." Solid State Ionics **132**(3): 241-251.

108. Shaikh, S. P. S., et al. (2015). "A review on the selection of anode materials for solid-oxide fuel cells." Renewable and Sustainable Energy Reviews **51**: 1-8.

109. Piccardo, P., et al. (2007). "ASR evaluation of different kinds of coatings on a ferritic stainless steel as SOFC interconnects." Surface and Coatings Technology **202**(4): 1221-1225.

110. Zhu, W. Z. and S. C. Deevi (2003). "Opportunity of metallic interconnects for solid oxide fuel cells: a status on contact resistance." Materials Research Bulletin **38**(6): 957-972.

111. Fergus, J. W. (2005). "Metallic interconnects for solid oxide fuel cells." Materials Science and Engineering: A **397**(1): 271-283.

112. Badwal, S. P. S., Muchtar, A., and Somalu, M. R. (1997). "Interaction between chromia forming alloy interconnects and air electrode of solid oxide fuel cells." Solid State Ionics **99**(3): 297-310.

113. Huang, K., Hou, P. Y., and Goodenough, J. B. (2000). "Characterization of iron-based alloy interconnects for reduced temperature solid oxide fuel cells." Solid State Ionics **129**(1): 237-250.

114. Shaigan, N., Ivey, D. G., and Chen, W. (2009). "Metal–Oxide Scale Interfacial Imperfections and Performance of Stainless Steels Utilized as Interconnects in Solid Oxide Fuel Cells." Journal of The Electrochemical Society **156**(6): B765-B770.

115. Bagheri, S. and M. Guagliano (2009). "Review of shot peening processes to obtain nanocrystalline surfaces in metal alloys." Surface Engineering **25**(1): 3-14.

116. Gindorf, C., Singheiser, L., and Hilpert, K. (2001). "Chromium vaporisation from Fe,Cr base alloys used as interconnect in fuel cells." Steel Research **72**(11-12): 528-533.

117. Oishi, N., Namikawa, T., and Yamazaki, Y. (2000). "Oxidation behavior of an La-coated chromia-forming alloy and the electrical property of oxide scales." Surface and Coatings Technology **132**(1): 58-64.

118. Linderoth, S. (1996). "Controlled reactions between chromia and coating on alloy surface." Surface and Coatings Technology **80**(1): 185-189.

119. Paknahad, P., Askari, M., and Ghorbanzadeh, M. (2014). "Application of sol–gel technique to synthesis of copper–cobalt spinel on the ferritic stainless steel used for solid oxide fuel cell interconnects." Journal of Power Sources **266**: 79-87.

120. Harthøj, A., Holt, T., and Møller, P. (2015). "Oxidation behaviour and electrical properties of cobalt/cerium oxide composite coatings for solid oxide fuel cell interconnects." Journal of Power Sources **281**: 227-237.

121. Froitzheim, J., Canovic, S., Nikumaa, M., Sachitanand, R., Johansson, L. G., and Svensson, J. E. (2012). "Long term study of Cr evaporation and high temperature corrosion behaviour of Co coated ferritic steel for solid oxide fuel cell interconnects." Journal of Power Sources **220**: 217-227.

122. Yang, Z. (2008). "Recent advances in metallic interconnects for solid oxide fuel cells." International Materials Reviews **53**(1): 39-54.

123. Fergus, J. W. (2005). "Sealants for solid oxide fuel cells." Journal of Power Sources **147**(1): 46-57.

124. Zhu, Q., Peng, L., and Zhang, T. (2007). Stable Glass Seals for Intermediate Temperature (IT) SOFC Applications. Fuel Cell Electronics Packaging. K. Kuang and K. Easler. Boston, MA, Springer US**:** 33-60.

125. Chou, Y.-S. and J. W. Stevenson (2006). "Compressive mica seals for solid oxide fuel cells." Journal of Materials Engineering and Performance **15**(4): 414-421.

126. Paulson, S. C. and V. I. Birss (2004). "Chromium Poisoning of LSM-YSZ SOFC Cathodes: I. Detailed Study of the Distribution of Chromium Species at a Porous, Single-Phase Cathode." Journal of The Electrochemical Society **151**(11): A1961-A1968.

127. Matsuzaki, Y. and I. Yasuda (2001). "Dependence of SOFC Cathode Degradation by Chromium-Containing Alloy on Compositions of Electrodes and Electrolytes." Journal of The Electrochemical Society **148**(2): A126-A131.

128. Matsuzaki, Y. and I. Yasuda (2000). "Electrochemical properties of a SOFC cathode in contact with a chromium-containing alloy separator." Solid State Ionics **132**(3): 271-278.

129. Jiang, S. P., Zhang, S., and Zhen, Y. D. (2005). "Early interaction between Fe–Cr alloy metallic interconnect and Sr-doped LaMnO3 cathodes of solid oxide fuel cells." Journal of Materials Research **20**(3): 747-758.

130. Tucker, M. C., Kurokawa, H., Jacobson, C. P., De Jonghe, L. C., and Visco, S. J. (2006). "A fundamental study of chromium deposition on solid oxide fuel cell cathode materials." Journal of Power Sources **160**(1): 130-138.

131. Zhang, T., Brow, R. K., Fahrenholtz, W. G., and Reis, S. T. (2012). "Chromate formation at the interface between a solid oxide fuel cell sealing glass and interconnect alloy." Journal of Power Sources **205**: 301-306.

132. Yang, Z., Xia, G., Meinhardt, K. D., Weil, K. S., and Stevenson, J. W. (2004). "Chemical stability of glass seal interfaces in intermediate temperature solid oxide fuel cells." Journal of Materials Engineering and Performance **13**(3): 327-334.

133. Yang, Z. G., Meinhardt, K. D., and Stevenson, J. W. (2003). "Chemical Compatibility of Barium-Calcium-Aluminosilicate Based Sealing Glasses with Ferritic Stainless Steel Interconnect in SOFCs." Journal of the Electrochemical Society, 150(8):A1095-A1101: A1095-A1101.

134. Weckhuysen, B. M. and R. A. Schoonheydt (1999). "Olefin polymerization over supported chromium oxide catalysts." Catalysis Today **51**(2): 215-221.

135. World Polyethylene. (2014, October). Retrieved from https://www.freedoniagroup.com/industry-study/world-polyethylene-3210.htm

136. Commodity Plastic Market to 2022. (2018, July 12). Retrieved from https://www.marketwatch.com/press-release/commodity-plastic-market-to-2022-industry-analysis-top-companies-material-trends-business-development-consumption-status-2018-07-12

137. Ruddick, V. J. and J. P. S. Badyal (1997). "AFM Study of the Breakup of Catalyst Particles during Ethylene Polymerization." The Journal of Physical Chemistry B **101**(10): 1791-1793.

138. Spiccia, L. and W. Marty (1986). “The fate of "active" chromium hydroxide, Cr(OH)3.3H2O, in aqueous suspension. Study of the chemical changes involved in its aging.” Inorg. Chem **25**: 266-271.

139. Vuurman, M. A., Hardcastle, F. D., and Wachs, I. E. (1993). "Characterization of CrO3/Al2O3 catalysts under ambient conditions: Influence of coverage and calcination temperature." Journal of Molecular Catalysis **84**(2): 193-205.

140. Best, S. A., Squires, R. G., and Walton, R. A. (1977). "The X-ray photoelectron spectra of heterogeneous catalysts." Journal of Catalysis **47**(3): 292-299.

141. Cavani, F., Koutyrev, M., Trifiró, F., Bartolini, A., Ghisletti, D., Iezzi, R., Santucci, A., and Del Piero, G. (1996). "Chemical and Physical Characterization of Alumina-Supported Chromia-Based Catalysts and Their Activity in Dehydrogenation of Isobutane." Journal of Catalysis **158**(1): 236-250.

142. Dines, T. J. and S. Inglis (2003). "Raman spectroscopic study of supported chromium(vi) oxide catalysts." Physical Chemistry Chemical Physics **5**(6): 1320-1328.

143. Groeneveld, C., Wittgen, P. P. M. M., van Kersbergen, P. L. M., Nuijten, C. E., and Schuit, G. C. A. (1979). "Hydrogenation of olefins and polymerization of ethene over chromium oxide/silica catalysts: I. Preparation and structure of the catalyst." Journal of Catalysis **59**(2): 153-167.

144. Hill, W. and G. Öhlmann (1989). "Thermal decomposition of chromium(VI)-oxide supported on silica." Reaction Kinetics and Catalysis Letters **38**(2): 289-294.

145. McDaniel, M. P., Collins, K. S., Benham, E. A., and Cymbaluk, T. H. (2008). "The activation of Phillips Cr/silica catalysts: V. Stability of Cr(VI)." Applied Catalysis A: General **335**(2): 252-261.

146. Thüne, P. C., Linke, R., van Gennip, W. J. H., de Jong, A. M., and Niernantsverdriet, J. W. (2001). "Bonding of Supported Chromium during Thermal Activation of the CrOx/SiO2 (Phillips) Ethylene Polymerization Catalyst." The Journal of Physical Chemistry B **105**(15): 3073-3078.

147. Vuurman, M. A., Wachs, I. E., Stufkens, D. J., and Oskam, A. (1993). "Characterization of chromium oxide supported on Al2O3, ZrO2, TiO2, and SiO2 under dehydrated conditions." Journal of Molecular Catalysis **80**(2): 209-227.

148. Weckhuysen, B. M. and I. E. Wachs (1997). "In Situ Raman Spectroscopy of Supported Chromium Oxide Catalysts: 18O2−16O2 Isotopic Labeling Studies." The Journal of Physical Chemistry B **101**(15): 2793-2796.

149. Wachs, I. E. (1996). "Raman and IR studies of surface metal oxide species on oxide supports: Supported metal oxide catalysts." Catalysis Today **27**(3): 437-455.

150. Zecchina, A., Garrone, E., Ghiotti, G., Morterra, C., and Borello, E. (1975). "On the chemistry of silica supported chromium ions. I. Characterization of the samples." The Journal of Physical Chemistry **79**: 966-972.

151. McDaniel, M. P. (1981). "The state of Cr(VI) on the Cr/Silica polymerization catalyst." Journal of Catalysis **67**(1): 71-76.

152. McDaniel, M. P. (1982). "The state of Cr(VI) on the Phillips polymerization catalyst: II. The reaction between silica and CrO2Cl2." Journal of Catalysis **76**(1): 17-28.

153. Zaki, M. I., Fouad, N. E., Leyrer, J., and Knözinger, H. (1986). "Physicochemical investigation of calcined chromia-coated silica and alumina catalysts: Characterization of chromium-oxygen species." Applied Catalysis **21**(2): 359-377.

154. Fubini, B., Ghiotti, G., Stradella, L., Garrone, E., and Morterra, C. (1980). "The chemistry of silica-supported Cr ions: A characterization of the reduced and oxidized forms of chromia/silica catalyst by calorimetry and ultraviolet-visible spectroscopy." Journal of Catalysis **66**(1): 200-213.

155. Liu, B., Fang, Y., and Terano, M. (2004). "High resolution X-ray photoelectron spectroscopic analysis of transformation of surface chromium species on Phillips CrOx/SiO2 catalysts isothermally calcined at various temperatures." Journal of Molecular Catalysis A: Chemical **219**(1): 165-173.

156. McDaniel, M. P. (1982). "The state of Cr(VI) on the Phillips polymerization catalyst: IV. Saturation coverage." Journal of Catalysis **76**(1): 37-47.

157. Vuurman, M. A., Stufkens, D. J., Oskam, A., Moulijn, J. A., and Kapteijn, F. (1990). "Raman spectra of chromium oxide species in CrO3/Al2O3 catalysts." Journal of Molecular Catalysis **60**(1): 83-98.

158. Weckhuysen, B. M., De Ridder, L. M., and Schoonheydt, R. A. (1993). "A quantitative diffuse reflectance spectroscopy study of supported chromium catalysts." The Journal of Physical Chemistry **97**(18): 4756-4763.

159. Kytökivi, A., Jacobs, J. P., Hakuli, A., Meriläinen, J., and Brongersma, H. H. (1996). "Surface Characteristics and Activity of Chromia/Alumina Catalysts Prepared by Atomic Layer Epitaxy." Journal of Catalysis **162**(2): 190-197.

160. Knözinger, H. and P. Ratnasamy (1978). "Catalytic Aluminas: Surface Models and Characterization of Surface Sites." Catalysis Reviews **17**(1): 31-70.

161. Phung, T. K., Lagazzo, A., Ribero, C. M. A., Sanchez, E. V., and Busca, G. (2014). "A study of commercial transition aluminas and of their catalytic activity in the dehydration of ethanol." Journal of Catalysis **311**: 102-113.

162. Ahmadi, E., Mohamadnia, Z., Rahimi, S., Mohammad, H. A., Mohammad, H. H., and Mahmood, R. (2016). "Phillips catalysts synthesized over various silica supports: Characterization and their catalytic evaluation in ethylene polymerization." Polyolefins Journal **3**(1): 23-36.

163. Fouad, N. E., Knözinger, H., Zaki, M. I., and Mansour, S. A. A. (1991). Chromia on Silica and Alumina Catalysts. Zeitschrift für Physikalische Chemie. **171:** 75.

164. McDaniel, M. (2017). "Manipulating polymerization chemistry of Cr/silica catalysts through calcination." Applied Catalysis A: General **542**: 392-410.

165. Fouad. N. E., Knözinger, H., Zaki, M. I. (1994). Chromia on Silica and Alumina Catalysts: Temperature-Programmed Reduction and Structure of Surface Chromates. Zeitschrift für Physikalische Chemie. **186:** 231.

166. Turek, A. M., Wachs, I. E., and DeCanio, E. (1992). "Acidic properties of alumina-supported metal oxide catalysts: an infrared spectroscopy study." The Journal of Physical Chemistry **96**(12): 5000-5007.

167. Cimino, A., De Angelis, B. A., Luchetti, A., and Minellli, G. (1976). "The characterization of CrOxSiO2 catalysts by photoelectron spectroscopy (XPS), X-ray and optical measurements." Journal of Catalysis **45**(3): 316-325.

168. Mentasty, L. R., Gorriz, O. F., and Cadus, L. E. (1999). "Chromium Oxide Supported on Different Al2O3 Supports: Catalytic Propane Dehydrogenation." Industrial & Engineering Chemistry Research **38**(2): 396-404.

169. Pradier, C. M., Rodrigues, F., Marcus, P., Landau, M. V., Kaliya, M. L., Gutman, A., and Herskowitz, M. (2000). "Supported chromia catalysts for oxidation of organic compounds: The state of chromia phase and catalytic performance." Applied Catalysis B: Environmental **27**(2): 73-85.

170. Lennartson, A. (2014). "The colours of chromium." Nature Chemistry **6**: 942.

171. Zaki, M. I., Hasan, M. A., and Fouad, N. E. (1998). "Stability of surface chromate – A physicochemical investigation in relevance to environmental reservations about calcined chromia catalysts." Applied Catalysis A: General **171**(2): 315-324.

172. Hewston, T. A. and B. L. Chamberland (1984). "Magnetic and structural studies of Cr2O5 and Cr3O8." Journal of Magnetism and Magnetic Materials **43**(1): 89-95.

173. Takayoshi, T., Ikemoto, I., Namikawa, T., and Kuroda, H. (1981). "X-Ray Photoelectron Spectrum of Cr2O5." Bulletin of the Chemical Society of Japan **54**(3): 913-914.

174. Maslar, J. E., Hurst, W. S., Vanderah, T. A., and Levin, I. (2001). "The Raman spectra of Cr3O8 and Cr2O5." Journal of Raman Spectroscopy **32**(3): 201-206.

175. Okamoto, Y., Fujii, M., Imanaka, T., and Teranishi, S. (1976). "X-Ray Photoelectron Spectroscopic Studies of Catalysts—Chromia–Alumina Catalysts—." Bulletin of the Chemical Society of Japan **49**(4): 859-863.

176. Frost, D. C., McDowell, C. A., and Woolsey, I. S. (1974). "X-ray photoelectron spectra of cobalt compounds." Molecular Physics **27**(6): 1473-1489.

177. Ikemoto, I., Ishii, K., Kinoshita, S., Kuroda, H., Alario Franco, M. A., and Thomas, J. M. (1976). "X-ray photoelectron spectroscopic studies of CrO 2 and some related chromium compounds." Journal of Solid State Chemistry **17**(4): 425-430.

178. Poole, C. P., Kehl, W. L., and Maclver, D. S. (1962). "Physical properties of coprecipitated chromia-alumina catalysts." Journal of Catalysis **1**(5): 407-415.

179. Kazanski, V. B. and J. Turkevich (1967). "Kinetics and ESR studies of ethylene polymerization on chromia-silica catalysts." Journal of Catalysis **8**(3): 231-239.

180. Biesinger, M. C., Payne, B. P., Grosvenor, A. P., Lau, L. W. M., Gerson, A. R., and Smart, R. S. C. (2011). "Resolving surface chemical states in XPS analysis of first row transition metals, oxides and hydroxides: Cr, Mn, Fe, Co and Ni." Applied Surface Science **257**(7): 2717-2730.

181. Biesinger, M. C., Brown, C., Mycroft, J. R., Davidson, R. D., and McIntryre, N. S. (2004). "X-ray photoelectron spectroscopy studies of chromium compounds." Surface and Interface Analysis **36**(12): 1550-1563.

182. Liu, B. and M. Terano (2001). "Investigation of the physico-chemical state and aggregation mechanism of surface Cr species on a Phillips CrOx/SiO2 catalyst by XPS and EPMA." Journal of Molecular Catalysis A: Chemical **172**(1): 227-240.

183. Merryfield, R., McDaniel, M., and Parks, G. (1982). "An XPS study of the Phillips Cr/silica polymerization catalyst." Journal of Catalysis **77**(2): 348-359.

184. Halada, G. P. and C. R. Clayton (1991). "Photoreduction of Hexavalent Chromium during X-Ray Photoelectron Spectroscopy Analysis of

Electrochemical and Thermal Films." Journal of The Electrochemical Society **138**(10): 2921-2927.

185. Rahman, A., Mohamed, M. H., Ahmed, M., and Aitani, A. M. (1995). "Characterization of chromia/alumina catalysts by X-ray photoelectron spectroscopy, proton induced X-ray emission and thermogravimetric analysis." Applied Catalysis A: General **121**(2): 203-216.

186. Kagwade, S. V., Clayton, C. R., and Halada, G. P. (2001). "Causes and prevention of photochemical reduction of hexavalent chromium during x-ray photoelectron spectroscopy." Surface and Interface Analysis **31**(6): 442-447.

187. Jaleel, V. A. and T. S. Kannan (1983). "Hydrothermal synthesis of chromium dioxide powders and their characterisation." Bulletin of Materials Science **5**(3): 231-246.

188. Harrison, P. G., Lloyd, P. G., Daniell, W., Bailey, C., and Azelee, W. (1999). "Evolution of Microstructure during the Thermal Activation of Chromium-Promoted Tin(IV) Oxide Catalysts: An FT-IR, FT-Raman, XRD, TEM, and XANES/EXAFS Study." Chemistry of Materials **11**(4): 896-909.

189. Gaines Jun, G. L. and W. Vedder (1964). "Dehydroxylation of Muscovite." Nature **201**: 495.

190. Rimstidt, J. D., Zhang, Y. and Zhu, C. (2016). "Rate equations for sodium catalyzed amorphous silica dissolution." Geochimica et Cosmochimica Acta **195**: 120-125.

191. Opila, E. J. (2004). "Volatility of Common Protective Oxides in High-Temperature Water Vapor: Current Understanding and Unanswered Questions." Materials Science Forum **461-464**: 765-774.

192. Opila, E. J., Jacobson, N. S., Myers, D. L., and Copland, E. H. (2006). "Predicting oxide stability in high-temperature water vapor." JOM **58**(1): 22-28.

193. Young, J. A. (2003). "Chromium(VI) Oxide, CrO3." Journal of Chemical Education **80**(3): 259.

194. Bunting, E. N. (1931). "Phase equilibria in the system Cr2O3-Al2O3." Bureau of Standards Journal of Research **6**(6): 947.

195. Busca, G. (2014). "The surface of transitional aluminas: A critical review." Catalysis Today **226**(Supplement C): 2-13.

196. Contescu, C., Jagiello, J., and Schwarz, J. A. (1993). “Heterogeneity of proton binding sites at the oxide/solution interface.” Langmuir **9**(7): 1754-1765.

197. Innocenzi, P. (2003). "Infrared spectroscopy of sol–gel derived silica-based films: a spectra-microstructure overview." Journal of Non-Crystalline Solids **316**(2): 309-319.

198. Leung, K., Nielsen, I. M. B., and Criscenti, L. J. (2009). "Elucidating the Bimodal Acid−Base Behavior of the Water−Silica Interface from First Principles." Journal of the American Chemical Society **131**(51): 18358-18365.

199. McHale, J. M., Navrotsky, A., and Perrotta, A. J. (1997). "Effects of Increased Surface Area and Chemisorbed H2O on the Relative Stability of Nanocrystalline γ-Al2O3 and α-Al2O3." The Journal of Physical Chemistry B **101**(4): 603-613.

200. Maciver, D. S., Tobin, H. H., Barth, R. T. (1963). "Catalytic aluminas I. Surface chemistry of eta and gamma alumina." Journal of Catalysis **2**(6): 485-497.

201. Carre, S., Gnep, N. S., Revel, R., and Magnoux, P. (2008). "Characterization of the acid–base properties of transition aluminas by model reaction." Applied Catalysis A: General **348**(1): 71-78.

202. Pearson, R. G. "Hard and Soft Acids and Base, HSAB, Part I, Fundamental principles." J. Chem. Educ. **45**(9): 581-587.

203. Weckhuysen, B. M., Schoonheydt, R. A., Jehng, J. M., Wachs, I. E., Cho, S. J., Ryoo, R., Kijlstra, S., and Poels, E. (1995). "Combined DRS-RS-EXAFS-XANES-TPR study of supported chromium catalysts." Journal of the Chemical Society, Faraday Transactions **91**(18): 3245-3253.

204. Gardiner, D. J., Littleton, C. J., Thomas, K. M., and Strafford, K. N. (1987). "Distribution and characterization of high temperature air corrosion products on iron-chromium alloys by Raman microscopy." Oxidation of Metals **27**(1): 57-72.